Design of a Centrifugal Compressor Impeller for Micro Gas Turbine Application

by
Bosman Botha van der Merwe

Thesis presented in fulfilment of the requirements for the degree of Master of Science in Engineering in the Faculty of Mechanical and Mechatronic Engineering at Stellenbosch University

Supervisor: Dr S.J. van der Spuy
Co-supervisor: Prof T.W. von Backström

December 2012

DECLARATION

By submitting this thesis electronically, I declare that the entirety of the work contained therein is my own, original work, that I am the sole author thereof (save to the extent explicitly otherwise stated), that reproduction and publication thereof by Stellenbosch University will not infringe any third party rights and that I have not previously in its entirety or in part submitted it for obtaining any qualification.

Date:…………………..

i

ABSTRACT

Design of a Centrifugal Compressor Impeller for Micro Gas Turbine Application

B.B. van der Merwe

Department of Mechanical and Mechatronic Engineering, Stellenbosch University,
Private Bag X1, Matieland 7602, South Africa
Thesis: *MSc. Eng.* (Mech)

December 2012

The use of micro gas turbines (MGTs) for the propulsion of unmanned aerial vehicles (UAVs) has become an industry standard. MGTs offer better performance vs. weight than similar sized, internal combustion engines. The front component of an MGT serves the purpose of compressing air, which is subsequently mixed with a fuel and ignited to both power the turbine which drives the compressor, and to produce thrust. Centrifugal compressors are typically used because of the high pressure ratios they deliver per stage. The purpose of this project was to design a centrifugal compressor impeller, and to devise a methodology and the tools with which to perform the aforementioned. A compressor impeller adhering to specific performance and dimensional requirements was designed. The new compressor was designed using a mean-line performance calculation code. The use of the code was vindicated through comparison with the results from a benchmark study. This comparison included mean-line, Computational Fluid Dynamic (CFD), and experimental results: the new design mean-line results were compared to the results of CFD simulations performed on the same design. The new design was optimised using an Artificial Neural Network (ANN) and Genetic Algorithm. Prior to and during optimisation, the ANN was trained using a database of sample CFD calculations. A Finite Element Analysis (FEA) was done on the optimised impeller geometry to ensure that failure would not occur during operation. According to CFD results, the final design delivered good performance at the design speed with regards to pressure ratio, efficiency, and stall margin. The mechanical stresses experienced during operation were also within limits. Experimental results showed good agreement with CFD results of the optimised impeller.

Keywords: micro gas turbine, centrifugal compressor, impeller, CFD, experimental, optimisation, FEA.

UITTREKSEL

Ontwerp van 'n Mikrogasturbine Sentrifigaalkompressor Rotor

("Design of a Centrifugal Compressor Impeller
for Micro Gas Turbine Application")

B.B. van der Merwe

*Departement van Meganiese and Megatroniese Ingenieurswese,
Universiteit van Stellenbosch,
Privaatsak X1, Matieland 7602, Suid-Afrika*
Tesis: *MSc. Ing.* (Meg)

Desember 2012

Die gebruik van mikrogasturbines vir die aandrywing van onbemande vliegtuie het 'n standaard geword in die industrie. Mikrogasturbines bied beter werkverrigting teen gewig as binnebrandenjins van soortgelyke grote. Hierdie eienskap verseker dat mikrogasturbines as aandryfmotors vir onbemande vliegtuie uiters voordelig is. Die voorste komponent van 'n mikrogasturbine dien om lug saam te pers, wat dan met brandstof gemeng en daarna aan die brand gesteek word om krag aan die kompressor en stukrag te voorsien. Sentrifugaalkompressors word tipies gebruik as gevolg van die hoë drukverhoudings wat hierdie komponente per stadium kan lewer. Die doel van hierdie projek was om 'n sentrifugaalkompressor te ontwerp, en 'n metode en die hulpmiddels te ontwikkel om laasgenoemde uit te voer. 'n Kompressor rotor wat voldoen het aan sekere werkverrigtings en dimensionele vereistes is ontwerp. Die nuwe kompressor rotor is met behulp van 1-dimensionele werkverrigting-berekeningskode ontwerp. Die berekeningsakkuraatheid van die kode en díé van 'n kommersiële Berekenings Vloeidinamika pakket is bevestig deur die berekende resultate te vergelyk met die van eksperimente. Die nuwe rotor is gevolglik deur middel van 'n Kunsmatige Neurale Netwerk en Genetiese Algoritme geoptimeer. Die Kunsmatige Neurale Netwerk is voor en gedurende optimering deur Berekenings Vloeidinamika simulasies opgelei. Die meganiese sterkte van die geoptimeerde rotor is nagegaan met behulp van 'n Eindige Element Analise. Dit is gedoen om te verseker dat die rotor nie sal faal by die bedryfspunt nie. Berekenings Vloeidinamika resultate het getoon dat die finale rotor ontwerp 'n goeie werkverrigting lewer by die ontwerpspoed, met betrekking tot drukverhouding, bennutingsgraad, en stakingsmarge. Eksperimentele resultate het goeie ooreenstemming met die Berekenings Vloeidinamika resultate van die geoptimeerde rotor getoon.

Sleutelwoorde: mikrogasturbine, sentrifigaalkompressor, rotor, Berekenings Vloeidinamika, eksperimenteel, optimering, Eindige Element Analise.

ACKNOWLEDGEMENTS

I would not have been able to finish this journey if not for certain individuals and institutions. I am sincerely grateful to all of them.

My father, Hendrik, who first introduced me to the world of engineering and who's memory lives on in our hearts.

My mother, Malinda. You are my guiding light.

All my friends and family. There are too many of you to single anyone out. Thanks for bearing with me.

My supervisors for all their insights and motivation. Dr S.J. van der Spuy for his unwavering optimism and Prof. T.W. von Backström for bringing me back to earth.

Ballast and my supervisors for the financial support of this project.

The guys in "Die Lasraam". Thanks for the coffee brakes, pizza specials, and all-around good vibes!

iv

To my dad…

TABLE OF CONTENTS

Table of Contents x

LIST OF FIGURES

LIST OF TABLES

NOMENCLATURE

Constants

R_o	Universal gas constant = 8.314570	[J/mol·K]

Symbols

A	Area	[m^2]
a	Sonic velocity, first element length in geometric progression	[m/s], [m]
B	Bézier control point	[~]
b	Blade height	[m]
$f_{startsplit}$	Splitter fraction of main blade length	[~]
C_p	Specific heat at constant pressure	[J/kg·K]
C_r	Contraction ratio correlation	[~]
C_v	Specific heat at constant volume	[J/kg·K]
C	Velocity (absolute vector)	[m/s]
c_f	Friction coefficient	[m/s]
d	Diameter	[m]
E	Error	[~]
h	Enthalpy, hub control point, distance	[J/kg], [~], [m]
I	Work input coefficient	[J/kg], [~]
i	Any integer value	[~]
J	Bézier blending variable	[~]
k	Penalty term exponent	[~]
L	Length	[m]
M	Mach number, molar mass	[~], [kg/mol]
m	Mass, meridional length	[kg], [m]
N	Quantity	[~]
n	Distance between stream surfaces, Bézier curve order	[m], [~]
P	Penalty term value, objective function value, Bézier function	[~]
p	Pressure, variable or parameter	[Pa], [1]
Q	Quantity in penalty term	[~]
Q_o	Design point mass flow rate	[kg/s]
Q_s	Stall mass flow rate	[kg/s]

---

[1] Unit depends on type of variable.

R	Gas constant	[J/kg·K]
r	Radius, common ratio	[m], [~]
s	Entropy, shroud control point	[J/kg·K], [~]
T	Temperature	[K]
t	Nondimensionalised length	[~]
t	Clearance gap, time	[m], [s]
U	Velocity (impeller vector)	[m/s]
u	Nondimensionalised length	[~]
W	Velocity (relative vector), weight factor	[m/s], [~]
y	Distance	[m]
z	Number of blades	[~]

Greek Symbols

α	Streamline slope angle with axis	[rad]
β	Blade camber angle	[rad]
γ	Specific heat ratio	[~]
η	Isentropic efficiency	[~]
θ	Endwall contour angle, blade camber circumferential position, temperature ratio	[rad], [rad], [~]
κ_m	Mean-line curvature	[~]
λ	Impeller tip distortion factor	[~]
μ	Mutation rate	[~]
ν	Kinematic viscosity	[m^2/s]
Π	Pressure ratio	[~]
ρ	Density	[kg/m^3]
σ	Slip factor	[~]
ϕ_2	Tip flow coefficient	[~]
$\overline{\omega}_{BL}$	Blade loading loss coefficient	[~]
$\overline{\omega}_{CH}$	Choke loss coefficient	[~]
$\overline{\omega}_{CL}$	Clearance gap loss coefficient	[~]
$\overline{\omega}_{cr}$	Supercritical Mach number loss coefficient	[~]
$\overline{\omega}_{DIF}$	Diffusion loss coefficient	[~]
$\overline{\omega}_{HS}$	Hub-to-shroud loading loss coefficient	[~]
$\overline{\omega}_{inc}$	Incidence loss coefficient	[~]
$\overline{\omega}_{mix}$	Wake mixing loss coefficient	[~]
$\overline{\omega}_{SF}$	Skin friction loss coefficient	[~]
$\overline{\omega}_{\lambda}$	Abrupt expansion loss coefficient	[~]

Subscripts

0	Compressor inlet (eye)
$0n$	Total condition
1	Impeller inlet
2	Impeller tip
3	Diffuser outlet
B	Bézier control point, blade parameter
CPU	Computer CPU quantity
CL	Camber line quantity
DF	Disk friction parameter
H	Hydraulic quantity
h, hub	Hub quantity
imp	Impeller quantity, imposed quantity
l	Lower bound
m	Meridional component, mother chromosome
$main$	Main blade quantity
n	Compressor section, Bézier order
p	Father chromosome
par	Parameter
$s, shroud$	Shroud quantity
$sample$	Sample of a specific entity
$splitter$	Splitter blade quantity
$step$	Step quantity
R	Recirculation parameter
r, θ, z	Cylindrical coordinate components
ref	Reference quantity
rms	Root-mean-square quantity
$t-s$	Total-to-static quantity
$t-t$	Total-to-total quantity
th	Quantity at throat
u	Upper bound
x, y, z	Cartesian coordinate components

Superscripts

$\cdot$	Time rate of change
$'$	Quantity in relative frame of reference
$+$	Dimensionless wall distance indicator

| * | Conditions for sonic velocity |
| $^-$ | Averaged quantity |

Acronyms

ANN	Artificial Neural Network
ASM	American Society for Metals
ASME	American Society of Mechanical Engineers
CAD	Computer Aided Design
CFD	Computational Fluid Dynamics
CMM	Coordinate Measuring Machine
CNC	Computer Numerical Control
CPU	Central Processing Unit
CSIR	Council for Scientific and Industrial Research
DOE	Design of Experiments
FEA	Finite Element Analysis
GA	Genetic Algorithm
GCC	Global Competitiveness Centre
GOM	Gesellschaft für Optische Messtechnik
KKK	Kuhnle, Kopp & Kausch
LE	Leading Edge
MEP	Maximum Efficiency Point
MGT	Micro Gas Turbine
MOO	Multi-objective Optimisation
MSC	MacNeal-Schwendler Corporation
NASA	National Aeronautics and Space Administration
NURBS	Non-uniform Rational Basis Spline
RAM	Random-access Memory
TE	Trailing Edge
UAV	Unmanned Aerial Vehicle

1 INTRODUCTION

According to the South African "Government Communication and Information System" (2011), the global market for unmanned aerial vehicles (UAVs) is estimated at US$14-billion per annum. This market is currently dominated by Israel and the United States of America, largely due to the need in these countries for UAVs in military applications. UAVs can be used for national security, crime fighting, disaster management, election monitoring, and search-and-rescue operations. Other areas of application include the agriculture and mining sectors. South Africa has the potential to use local skills to design and manufacture UAVs. However, the country has experienced some challenges in terms of the availability of experienced engineers (Esterhuizen, 2011).

Funding for the training of engineers has been made available by the South African Air Force in the form of the Ballast project. The purpose of the Ballast project is to increase the capacity in South Africa with regards to knowledge and experience in the field of turbomachinery. Work under the Ballast project at Stellenbosch University has, over the last 3 years, specifically focused on micro gas turbines (MGTs, see Figure 1.1) used for the propulsion of UAVs. Propulsion systems used in the past have typically been internal combustion engines (Jabiru, 2011) and electric motors powered by batteries or fuel cells (Warwick, 2010). The growing need for higher performance, however, has been the basis of a global interest in, and on-going research into MGTs.
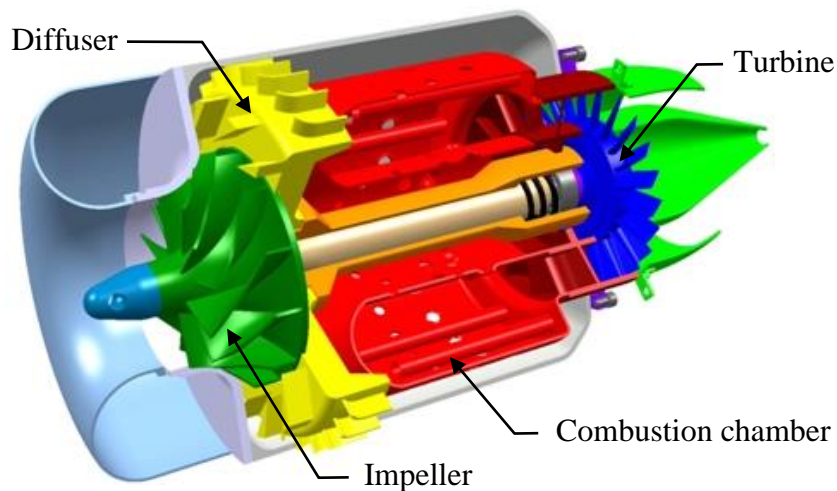
Figure 1.1: Components of a typical MGT. Adapted from Pichlmeier (2010).

The market for gas turbine engines demands machines with high efficiency, low weight, and high reliability (Japikse and Baines, 1994). The number of different types of gas turbines is extensive, and so is their range of applications: from large machines powering commercial and military aircraft, to industrial-sized units used for power generation. These devices serve the purpose of providing energy, in

whichever form necessary. An MGT is a member of a class of turbomachinery categorised by the small scale of the components used in these machines. According to Van den Braembussche (2005), MGTs have generated a growing interest in the last decade. The large energy density (Watt hours per kilogram) obtained by these turbomachines makes them attractive for the propulsion of UAVs.

Currently, international companies like Microturbo, Teledyne, Hamilton Sundstrand, and Williams International are leaders in the manufacturing of small turbojet and turbofan engines of varied thrust for UAVs (Kiney, 2009). The methodology of manufacturing these engines involves taking existing parts, designed for other applications such as turbochargers, and adapting them to desired specifications. This means that the resulting machine is not design orientated and may have inferior performance due to a number of factors. Theoretically, this allows for the improvement of the design to reach a desired performance. The desired performance is typically a combination of operational parameters such as mass flow rate, efficiency, pressure ratio, and input power.

The focus of this study was on the MGT compressor, more specifically, the compressor impeller. One of the big hurdles constraining the development of MGT impellers is the design and manufacturing costs involved. It is considerably less expensive to apply the "off the shelf" methodology mentioned in the previous paragraph. The low resulting performance is often considered acceptable, bearing in mind the relatively low cost of manufacturing these impellers. However, application orientated impeller designs can increase the operational life and fuel efficiency of MGTs, reducing life-cycle costs.

1.1   Project Objective

The primary objective of this project was to design a centrifugal compressor impeller for application in an MGT. The compressor diffuser design was the topic of a different study (Krige, 2012). The impeller design had to adhere to dimensional constraints and deliver a specific level of performance. The dimensional constraints and performance requirements are discussed in detail in Section 4.2. The main requirements were that the compressor delivers a total-to-total (t-t) pressure ratio of 4.72, at an isentropic efficiency of 79.8% (t-t). These performance requirements were obtained from initial GasTurb (Kurzke, 2009) cycle calculations done at the CSIR. The values were to be obtained at a design point with a mass flow rate of 0.325 kg/s from an impeller with an outlet diameter of no more than 75 mm, rotating at a speed of 121 krpm. The design point had to be the point of maximum efficiency.

To achieve the primary objective, a design methodology had to be developed. The methodology included the use of a mean-line code and Computational Fluid

Dynamic (CFD) software to calculate the compressor performance. Consequently, the following secondary objectives were identified for the project:

1) Validate the in-house, mean-line performance calculation code developed by De Wet (2011).
2) Validate the commercial CFD software (Numeca International, 2011a).
3) Design a compressor using the mean-line code.
4) Optimise the mean-line design using CFD.
5) Perform a Finite Element Analysis (FEA) of the optimised design.

According to Aungier (2000), the most accurate and reliable performance analysis and design techniques for turbomachinery components are based on mean-line (1-dimensional) flow models. In these models, flow is analysed along a mean stream surface. The mean stream surface runs through and connects individual components and stages of the turbomachine. The mean-line flow analysis is based on averaged values of the distributed properties of the working fluid flowing through component passages. The relatively short computational time required to calculate performance using a mean-line approach makes it ideal for creating an initial compressor design. There are however aerodynamic factors of a design that cannot be accurately modelled by a mean-line analysis. This shortcoming becomes prominent at off-design mass flow rates. This can be ascribed to the inherent 3-dimensional nature of the flow in turbomachinery during operation, and requires that the compressor design be analysed 3-dimensionally as well.

Three-dimensional design methods for all types of turbomachinery components have come a long way in the last 10 years (Verstraete et al., 2010), with the introduction of numerical optimisation into the field. This has been done in order to improve the design point performance, shorten the design life cycle, and to reduce both costs and the reliance on experience in design practice. The development of CFD software, combined with improvements in computing power, has made numerical optimisation based on CFD simulations more popular than ever. Optimisation however requires that the compressor geometry be defined by a set of parameters (see Section 5). The mean-line design served as an ideal tool to define these parameters and their initial values.

1.2   Operation of Centrifugal Compressors

Centrifugal turbomachinery (see impeller in Figure 1.1) is used in applications where a low stage volume flow rate and a high pressure ratio are required, compared to axial flow turbomachinery where a high stage volume flow rate and low pressure ratio is important. During operation, atmospheric air enters the centrifugal compressor at the eye. As seen in Figure 1.2, the air travels in the axial direction with an absolute velocity vector, C_1. Pre-whirl may be applied to the inlet flow, thereby adding a tangential component to C_1. This is done to adjust the

operational mass flow rate with negligible variation in shaft speed or pressure ratio (Mohseni et al., 2012).

The airflow propagates along the inlet channel until it reaches the inducer section which translates the flow onto the impeller blades. Once the flow is translated, work is imparted to it thereby increasing the total pressure and temperature of the air. The flow propagates along the blade channels until it reaches the impeller tip at r_2. The air now leaves the blades with an absolute velocity vector, C_2, and a relative velocity vector W_2. The relative velocity vectors are obtained by subtracting the impeller velocity vectors, U_n, from the absolute velocity vectors, C_n, or vice versa. The tangential component of the outlet velocity, $C_{\theta 2}$, would ideally be equal to the tip velocity, U_2, minus the tangential component of the outlet relative velocity, $W_{\theta 2}$. However, due to slip, the magnitude of $C_{\theta 2}$ is reduced by the amount ΔC_θ.

As the air leaves the impeller at the tip, it enters the diffuser. At this point, the fluid total pressure has a high dynamic pressure component. The diffuser regains some static pressure, albeit at a loss of total pressure. The magnitude of this loss depends on the type and shape of diffuser used. Static pressure is recovered by an increase in the radial, cross-sectional area and/or conservation of angular momentum.
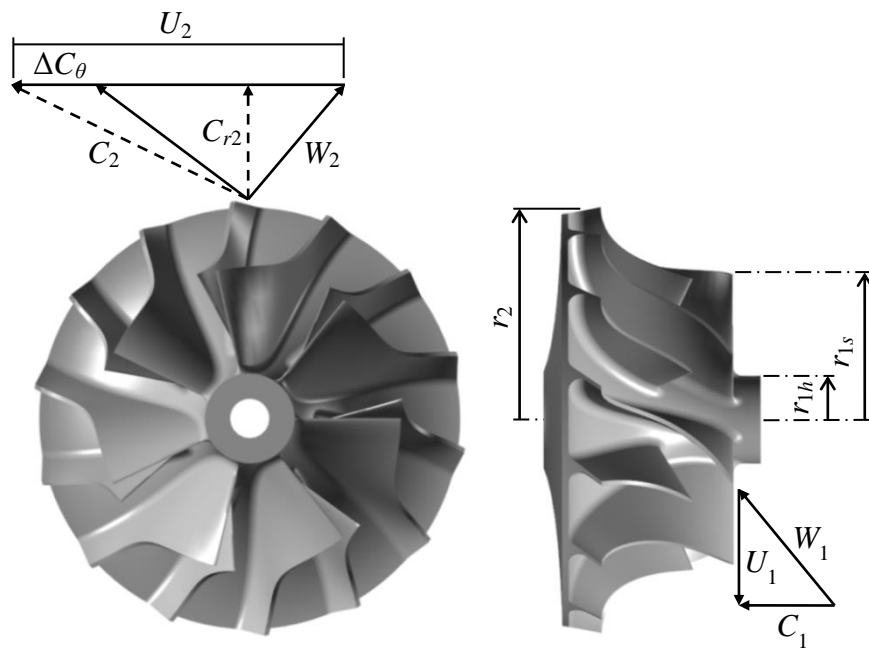
Figure 1.2: Velocity diagrams for centrifugal compressor impeller.

The centrifugal compressor operation is modelled as compressible flow since the fluid experiences changes in both temperature and pressure. It is assumed that there is no heat transfer between the compressor components and the atmosphere (adiabatic flow). The Mollier chart in Figure 1.3 expresses the compressor

performance in terms of the thermodynamic properties of air. The equation for total enthalpy at any point, n, along a streamline in the meridional direction may be written as

$$h_{0n} = h_n + \frac{C_n^2}{2} \qquad (1.1)$$

Therefore, the total enthalpy at the compressor inlet is given by $n = 0$. Since no work is done on the fluid between sections 0 and 1, the total enthalpies at these two points are equal, as seen in Figure 1.3.

$$h_{00} = h_{01} \qquad (1.2)$$

$$h_0 + \frac{C_0^2}{2} = h_1 + \frac{C_1^2}{2} \qquad (1.3)$$
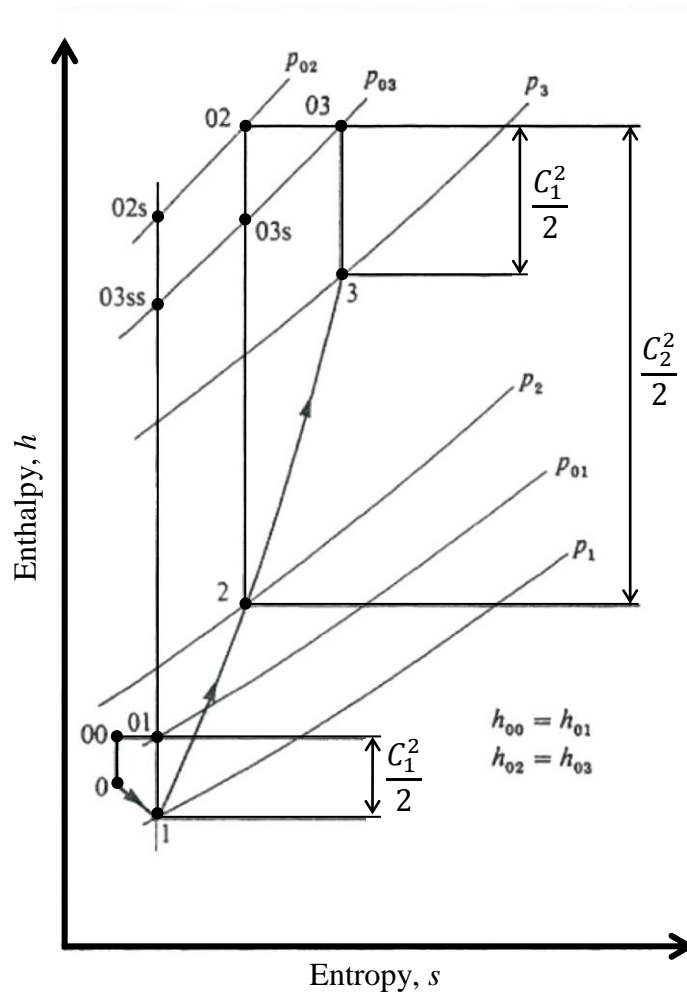
Figure 1.3: Mollier chart for a centrifugal compressor. Adapted from Dixon (1998).

Between sections 1 and 2, work is done on the fluid thereby increasing the total enthalpy. The rise in the total enthalpy of the air is equal to the amount of work done, W, per unit mass, m,

$$h_{02} - h_{01} = \frac{W}{m} = U_2 C_{\theta 2} - U_1 C_{\theta 1} \tag{1.4}$$

Substituting for h_0 gives

$$I = h_1 + \frac{C_1^2}{2} - U_1 C_{x1} = h_2 + \frac{C_2^2}{2} - U_2 C_{x2} \tag{1.5}$$

where I is the impeller rothalpy. The value of I remains constant throughout the impeller and after some manipulation of equation (1.5), it can be shown that the rise in static enthalpy between sections 1 and 2 is given by the following equation:

$$h_2 - h_1 = \frac{U_2^2 - U_1^2}{2} + \frac{W_1^2 - W_2^2}{2} \tag{1.6}$$

with the main contributor to the static enthalpy rise being the $(U_2^2 - U_1^2)/2$ term.

The diffuser is located between sections 2 and 3 of the compressor. No external work is done on the fluid in the diffuser and the total enthalpy remains constant, as given by equation (1.7).

$$h_{02} = h_{03} \tag{1.7}$$

1.2.1   Efficiency and pressure ratio

The efficiency of a centrifugal compressor is calculated by dividing the ideal work input by the actual work input (Japikse and Baines, 1994). The work input of a centrifugal compressor can be obtained either by directly measuring the torque required to turn the impeller or by determining the change in total temperature of the working fluid. The less the fluid is heated, the more efficient the compressor.

The isentropic efficiency of the compressor is based on either total-to-total or total-to-static quantities. The total-to-total and total-to-static efficiencies use total and static values respectively for the temperature and pressure values at the outlet section in equation (1.8). If the kinetic energy at the exit of the impeller is utilised in, for example, a next stage then the total-to-total efficiency is calculated. However, if the exit kinetic energy is lost then the total-to-static efficiency is calculated.

$$\eta_{imp(t-t)} = \frac{\left(\frac{p_{02}}{p_{01}}\right)^{\frac{\gamma-1}{\gamma}} - 1}{\frac{T_{02}}{T_{01}} - 1}$$ (1.8)

In this project, the compressor included only a single stage. The isentropic efficiencies were calculated and used for comparison.

The pressure ratio, Π, of a component is measured between the inlet of the component and the component outlet. Similar to the efficiency, the pressure ratio is given either as a total-to-total or total-to-static quantity. For centrifugal compressors, the pressure ratio is affected by both the diffusion of the relative velocity and the change in radius. This is why, for centrifugal compressors, a higher pressure ratio can be achieved per stage than with axial flow compressors.

$$\Pi_{imp(t-t)} = \frac{p_{02}}{p_{01}}$$ (1.9)

The pressure ratio that is achieved by a centrifugal compressor impeller, along with the surge and choke mass flow rates (see Section 1.2.2), increases with increasing impeller speed. The maximum efficiency at higher impeller speeds is consequently obtained at higher mass flow rates.

1.2.2   Surge and choke

Stable compressor operation is bounded by the occurrence of surge or choke, at the lower and upper operating mass flow rates respectively. Surge is associated with the maximum pressure ratio point while choked flow is often preceded by the point of maximum efficiency (Aungier, 2000). The occurrence of surge and choke can be best explained by considering Figure 1.4. The figure shows an idealised, fixed speed characteristic curve.

The pressure ratio at Point 1 is developed at a zero mass flow rate. A centrifugal compressor never operates at this point; it is off-design and highly unstable. The maximum pressure ratio is obtained at Point 2, and Point 3 is the maximum compressor efficiency point. This point is typically the design point of the compressor, albeit at a lower-than-maximum pressure ratio.
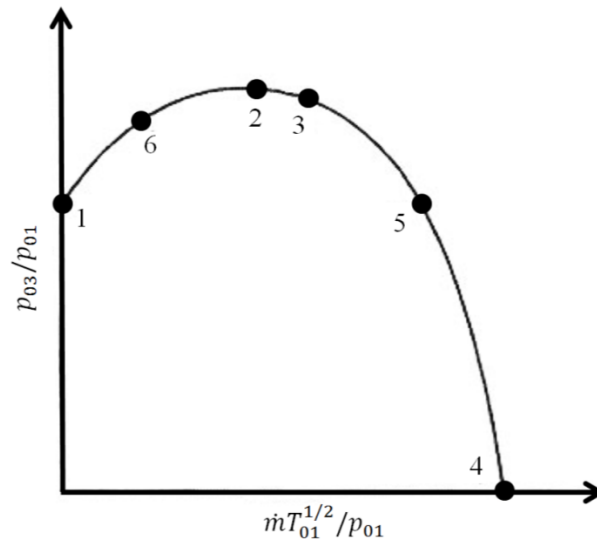
Figure 1.4: Theoretical centrifugal compressor performance curve. Adapted from Dixon (1998).

Surge is experienced when the compressor operates near Point 6 on the positive slope of the performance curve. Surge tends to originate in the diffuser where the effects of surface friction cause the restriction of the compressor mass flow rate. This leads to aerodynamic stall occurring along the impeller blades. As the mass flow rate decreases, the back pressure p_{03} follows suit leading to a further reduction in mass flow rate and finally, the reversal of airflow. Positive, steady flow can again be established by, for example, lowering the impeller speed. However, as the speed is again increased, the mass flow rate would only build up to the restricted value, resulting in the recurrence of surge. As the compressor goes into surge, the effects can be dramatic. An increase in noise level is experienced due to pulsating airflow and mechanical vibration, the latter having the potential to cause compressor failure (Dixon, 1998).

Conversely, if flow restriction were to occur while the compressor was operating at Point 5, the reduction in mass flow rate would lead to a higher back pressure which would return the mass flow rate to a position between Points 3 and 5. The process is therefore self-correcting on the negative slope of the impeller performance curve.

The mass flow rate can increase to Point 5 in Figure 1.4 where it is choked due to sonic conditions being reached at some location in the compressor impeller. The occurrence of choke is coupled with the formation of shockwaves in the impeller blade passages. Choke may occur at the impeller inlet, within the impeller passages, or in the diffuser depending on the compressor geometry and operating conditions. When flow in the rotating impeller passages is choked, it is the relative velocity W that chokes. If choke occurs in stationary passages, the absolute velocity C is choked. Because choke behaviour for rotating and

stationary passages differs, separate analyses are necessary for the compressor inlet, impeller, and diffuser.

At the compressor inlet, choke takes place when the absolute velocity C is equal to the speed of sound, a, at the inlet (Dixon, 1998), or

$$C^2 = a^2 = \gamma RT \tag{1.10}$$

From equation (1.10) and $C_p T_0 = C_p T + \frac{1}{2} \gamma RT$, the following equation is obtained at sonic conditions:

$$\frac{T}{T_0} = \left(1 + \frac{\gamma R}{2 C_p}\right)^{-1} = \frac{2}{\gamma + 1} \tag{1.11}$$

Now, assuming isentropic flow at the compressor inlet,

$$\frac{\rho}{\rho_0} = \frac{p}{p_0} \frac{T_0}{T} = \left[1 + \frac{1}{2}(\gamma - 1)M^2\right]^{1 - \left(\frac{\gamma}{\gamma - 1}\right)} \tag{1.12}$$

with a Mach number of unity giving

$$\frac{\rho}{\rho_0} = \left(\frac{2}{\gamma + 1}\right)^{\frac{1}{\gamma - 1}} \tag{1.13}$$

Equations (1.11) and (1.13) can be substituted into the continuity equation $\dot{m}/A = \rho C = \rho \sqrt{\gamma RT}$, then

$$\dot{m}/A_0 = \rho_0 a_0 \left(\frac{2}{\gamma + 1}\right)^{\frac{\gamma + 1}{2(\gamma - 1)}} \tag{1.14}$$

where A_0 is the cross-sectional area at some location along the compressor inlet. The total quantities ρ_0 and a_0 remain constant which means that the choke mass flow rate at the compressor inlet is unchanged. As opposed to the rotating passages (see following paragraphs), the choke mass flow rate at the inlet is the same at all impeller speeds. In order to increase the choke mass flow rate at the inlet, the cross-sectional area, A_0, needs to be increased.

When choke occurs at the inlet of the rotating impeller passages (for the special case $C_{\theta 1} = 0$), it is the relative velocity, W, that is now equal to the speed of sound at that section (Dixon, 1998).

$$W^2 = a^2 = \gamma RT \tag{1.15}$$

And with

$$T_{01} = T + \frac{1}{2}\frac{\gamma RT}{C_p} - \frac{1}{2}\frac{U^2}{C_p} \tag{1.16}$$

the following equation is obtained:

$$\frac{T}{T_{01}} = \left(\frac{2}{\gamma + 1}\right)\left(1 + \frac{U^2}{2C_pT_{01}}\right) \tag{1.17}$$

Assuming isentropic flow and using the continuity equation,

$$\begin{aligned}
\frac{\dot{m}}{A} &= \rho_{01}a_{01}\left(\frac{T}{T_{01}}\right)^{\frac{\gamma+1}{2(\gamma-1)}} \\
&= \rho_{01}a_{01}\left[\frac{2}{\gamma+1}\left(1 + \frac{U^2}{2C_pT_{01}}\right)\right]^{\frac{\gamma+1}{2(\gamma-1)}} \\
&= \rho_{01}a_{01}\left[\frac{2 + (\gamma-1)U^2/a_{01}^2}{\gamma+1}\right]^{\frac{\gamma+1}{2(\gamma-1)}}
\end{aligned} \tag{1.18}$$

If there is choke in rotating passages of the compressor, equation (1.18) indicates that the mass flow rate is, among others, a function of the impeller operating speed. As the impeller speed increases, the compressor will have a larger mass flow rate at choked conditions. That is, unless choke occurs in some other, stationary part of the compressor due to the larger mass flow rate. In most cases, the area A in equation (1.18) is the impeller throat area. The throat area is defined as the smallest sectional area quasi-normal to the flow through the impeller. Splitter blades are used for high Mach number flows and their purpose is to maintain high blade solidity while reducing the blade metal blockage, thereby increasing the throat area. This delays the occurrence of choke (Aungier, 2000).

The relation for the choked flow at the compressor inlet (equation (1.14)) holds for the diffuser passage as well. It should be noted that the stagnation conditions now refer to those at the diffuser and not the compressor inlet. Because an analysis of a diffuser did not form part of this project, the equations describing the physics of this component were omitted. However, choke in the diffuser could not be ignored as it would affect the operation of the impeller located upstream. The choked mass flow rate in the diffuser is dependent on the impeller speed and is given by the following correlation, for a radial bladed impeller (Dixon, 1998):

$$\frac{\dot{m}}{A_2} = \rho_{01}a_{01}\frac{[1 + (\gamma-1)\eta_i\sigma U_2^2/a_{01}^2]^{\frac{\gamma}{\gamma-1}}}{[1 + (\gamma-1)\sigma U_2^2/a_{01}]^{1/2}}\left(\frac{2}{\gamma+1}\right)^{\frac{\gamma+1}{2(\gamma-1)}} \tag{1.19}$$

where σ is the impeller slip factor.

1.3   Thesis Outline

The project motivation and objectives, along with details on the basic operation of centrifugal compressors have been discussed in this section. Section 2 details the information gathered during the literature survey. The relevant literature identified in the survey is presented in a structured format which follows the layout of the thesis.

The benchmark analyses that were required to reach the 1st and 2nd secondary objectives are the focus of Section 3. The setup of the numerical analyses is explained with an emphasis on the methodology used in this, and the following sections. This is followed by a discussion of the results that were obtained.

All the details about the mean-line design are discussed in Section 4. The section contains details on the modification of the in-house mean-line code, the final mean-line design, and the CFD screening of the new compressor geometry. The work in Section 4 falls in line with the requirements of the 3rd secondary objective.

Section 5 contains all the information on the optimisation of the mean-line design presented in Section 4. The compressor parameterisation is discussed in detail, along with the setup of the optimisation algorithm (4th secondary objective). The final results are also evaluated with regards to the optimised compressor CFD and FEA, as required by the 5th secondary objective. Experimental results are also discussed in this section.

The project conclusion is presented in Section 6 along with aspects to be considered in future studies.

2 LITERATURE SURVEY

2.1   Introduction

The following literature survey focuses on two specific areas, namely MGTs (Section 2.2), and the analysis and design of centrifugal compressors (Section 2.3).

2.2   Micro Gas Turbines

The physics behind the operation of MGTs and larger turbomachines of the same type (axial or radial) are essentially the same. However, applying scaling procedures to large, existing turbomachinery components in order to design MGTs presents some problems. According to Van den Braembussche (2005), the main issues are the following:

- The large difference in **Reynolds numbers** between large and micro gas turbomachinery components.
- Significant **heat transfer** between the hot and cold components in micro turbomachinery (negligible in large machines).
- **Geometrical and mechanical restrictions** incurred by the manufacturing processes and mechanical properties of micro turbomachinery components.

Low **Reynolds number** and surface roughness are two very significant limiting factors for micro turbomachinery efficiency. Casey (1985) measured a drop of 10% in stage efficiency between impellers operated at high (70×10^3 to 120×10^3) and at low Reynolds numbers (20×10^3). The higher the surface roughness compared to the overall hydraulic diameter, the higher the skin friction losses. This relative surface roughness increases as compressors become smaller. The reason for this is that manufacturing processes, like milling or casting, at best provide an absolute surface roughness. The consequence is that for a given Reynolds number, the losses due to skin friction increase with decreasing impeller size. The skin friction can however be decreased by using manufacturing processes that improve the surface finish.

High temperature gradients exist between the compressor and other components of a turbomachine. In micro compressors with high ratios of surface area to volume, these high temperature gradients lead to significant **heat transfer** to the compressor (Casey and Fesich, 2010). This presents the problem that compressor operation cannot be modelled as being adiabatic (Sirakov, 2005). Gong *et al.* (2004), Epstein (2004), and Isomura *et al.* (2001) have investigated the impact of temperature gradients in small turbomachinery where the shroud wall reaches temperatures of 1000 K. This leads to additional losses in compressor efficiency of between 20 and 40 per cent. Therefore, in applications where high combustion

chamber and impeller exhaust gas temperatures are reached, non-adiabatic effects may considerably reduce the overall efficiency of the compressor. Thermal insulation between the compressor inlet and outlet is therefore crucial.

There are a number of **geometrical and mechanical restrictions** that limit the attainable efficiency of micro turbomachinery. These restrictions include the size of the clearance gap and the blade fillets. It has been shown in numerous publications (Jansen (1967), Pampreen (1973), Musgrave (1980), Senoo (1987), and Brasz (1988)) that large relative clearance gaps impair the efficiency of centrifugal impellers. Typically, increasing the relative clearance gap (t/b_2) by 10% leads to a drop in efficiency of 3 to 4 per cent. As the impeller size decreases, it becomes more difficult to maintain a small relative clearance gap. This is due to both limits on manufacturing tolerances and bearing technology (Schiffmann and Favrat, 2010). Hydrostatic oil bearings, typically used in automotive turbochargers, allow for overall clearances of between 0.1 mm and 0.3 mm. These tolerances complicate the inclusion of small clearance gaps in order to avoid interference between the blade tip and the shroud surface. The choice of bearings and assembly tolerances therefore has a direct effect on the efficiency of the compressor.

Another complication associated with the small size of MGT impellers is the relative bluntness of blade leading edges and the size of blade fillets, as compared to larger impellers. Although the wider blades may reduce tip leakage, the blockage and distortion of flow becomes more significant at the impeller throat and outlet. Consequently, pressure recovery by the diffuser and stage efficiency are negatively affected because of distorted flow at the diffuser inlet. The blade bluntness and fillet are not to be confused with the blade thickness distribution in the spanwise direction at the leading edge. For small scale impellers, thick blade roots reduce mechanical stresses during operation while having little effect on compressor efficiency.

2.3   Analysis and Design of Centrifugal Compressors

2.3.1   Mean-line analysis

The analysis or design of a centrifugal compressor typically involves two distinct stages, the first one of these applying mean-line theory (Aghaei and Tousi, 2007). The mean-line analysis is typically followed by a more in-depth CFD study of the compressor geometry. Aghaei and Tousi obtained a preliminary compressor design using a mean-line code based on previous experience. The inlet and outlet blade angles and the "skeletal" dimensions required to achieve a certain pressure ratio, mass flow rate, and impeller speed were obtained. Good agreement between 1-D and CFD results was obtained for a new compressor design with a pressure ratio of around 4.

Benini and Giacometti (2007) used 1-dimensional calculations, which included loss and deviation correlations from Aungier (2000), as a first step to design a small turbojet-engine for research purposes. An impeller with radial blades was designed to make manufacturing of the impeller easier. It has however been shown that backswept impeller blades provide compressors with better peak efficiencies and part-load operation (Japikse and Baines (1994), Zangeneh *et al.* (1998), and E. Benini (2003)). Nevertheless, a small and low-cost jet-engine with a thrust of 200 N was developed.

The objective of Vick *et al.* (2009) was to design a recuperated ceramic turboshaft engine which could develop 3 kW of electric power. The design process included a cycle analysis, choosing the number of shafts and turbine stages to use, and a specification of the maximum allowable tensile stress in the compressor components at operational temperature. A turbine velocity diagram, which would deliver a preliminary design pressure ratio, was then drawn up. The mass flow rate of air during operation and the sizes of the compressor and turbine blade rows were determined. The efficiencies of the turbomachinery components were also estimated. Finally, the cycle analysis, pressure ratio, and velocity diagrams were refined iteratively. The whole process was performed using mean-line models.

Tamaki et al. (2009) followed a mean-line method to obtain an initial design for a multi-splitter centrifugal compressor. The inducer section of the compressor was first designed by selecting the inlet radius of the impeller. The radius was calculated to minimise the relative Mach number at the shroud side leading edge of the main blade. The stall mass flow rate was also estimated using an empirical correlation (Tamaki and Yamaguchi, 2007) to ensure that the operating point of the compressor fell within the stall and choke limits. The outlet section of the impeller was designed to achieve the required pressure ratio. A vaned diffuser was also designed using 1-dimensional calculations and empirical correlations.

Design optimisation of a centrifugal compressor using mean-line performance calculation was carried out by Schiffmann & Favrat (2010). A mean-line code was compiled using MATLAB. The code was used to calculate the isentropic efficiencies and pressure ratios for different impeller geometries at varying mass flow rates and impeller speeds. Loss correlations were implemented to calculate the compressor performances while each station of the compressor was tested for choke conditions. Good agreement between mean-line and experimental results was obtained for an initial design which permitted the use of the mean-line code for optimisation.

2.3.2   Computational Fluid Dynamics

A study by De Wet *et al.* (2010) involved the CFD simulation of an "Eckardt O-Rotor" (Eckardt, 1974) and an open test case known as the "Radiver" test case (Ziegler et al., 2003). The CFD results were compared with previously obtained experimental data. NUMECA™ software, developed for the simulation of

turbomachinery operation, was used for the CFD simulation (Numeca International, 2011b). The rotational speed of the impeller and the mass flow rates used in the CFD were adjusted from the test values to represent standard atmospheric conditions. The inlet conditions for the rotor were adjusted to account for Reynolds number effects of different boundary layer heights and therefore effective flow areas. During the study, only scalar quantities were obtained from the simulation and used for verification of the experimental results. The properties that were compared were temperatures, flow angles, and pressures. Area averaging was applied to obtain scalar values at the relevant boundaries. The Reynolds number effect played an insignificant role in the results of the simulation and the difference between the experimental and CFD data could not be attributed to the Reynolds number effect. Agreement with static pressure measurements was good with a maximum deviation of 1.38% obtained. The largest difference in total pressure values was 3.01%.

Benini & Giacometti (2007) designed a small turbojet-engine centrifugal compressor using the CFD package, ANSYS CFX 10© (ANSYS Inc., 2011). An iterative design process was followed until the CFD results matched those of the mean-line calculations. The resulting compressor design was then manufactured and assembled along with the combustor and turbine to produce the turbojet-engine.

The three-dimensional shape of a centrifugal compressor impeller was designed by Tamaki et al. (2009) with the use of CFD. More specifically, the blade inlet and outlet angles were varied to produce several trial impeller designs. The compressor was designed to include a recirculation device that would enhance the operating range. This recirculation device was found to have a strong effect on the convergence of the calculations, even more so at low mass flow rates. Two final compressor designs were obtained, manufactured, and tested. They delivered pressure ratios of 4.8 and 5.7 respectively.

In a study by Simpson et al. (2012), centrifugal compressor diffusers with small diffusion ratios were designed and tested. Vaneless diffusers were used, with the diffusion ratio being defined as the outlet radius of the diffuser divided by its inlet radius. The CFD in the study was performed using an in-house, structured grid, non-linear Navier-Stokes solver. The solver was primarily developed for application in the field of turbomachinery. The initial geometries for the endwalls, impeller, and diffuser were taken from a baseline design. The objective of decreasing the diffusion ratio from 1.45 to 1.3 without compromising performance was achieved. It was found that the CFD model yielded reliable performance predictions.

Dickmann et al. (2006) studied unsteady flow in a centrifugal compressor using CFD. Results of experimental and CFD simulations compared well allowing the latter to be used to visualise flow through the complex geometry of the

compressor at design and off-design conditions. This kind of visualisation is very hard and almost impossible to obtain using experimental techniques.

2.3.3   Design optimisation

An MGT centrifugal compressor ($d_2 = 20$ mm) was designed and optimised to deliver a specific performance while adhering to mechanical stress constraints by Verstraete *et al.* (2010). The optimisation involved building a database of CFD results using the Design of Experiments (DOE) technique. An Artificial Neural Network (ANN) was used to predict the compressor performance quantities as functions of geometric parameters. Optimisation was done using a Genetic Algorithm (GA). The optimisation was subject to an objective function which included penalty terms for mechanical stress, isentropic efficiency, mass flow rate, and relative Mach number distribution at the blade leading edge.

Schiffmann & Favrat (2010) performed multipoint optimisation on a small-scale centrifugal compressor for use in heat pumps. The optimisation process was performed using an Evolutionary Algorithm, MOO, which was developed by Leyland (2002) and Molyneaux (2002). Excellent correlation between experimental and optimised results was obtained. This allowed the design of a centrifugal compressor able to fit the wide operational range of a domestic heat pump. The wide operating range includes different mass flow rates as well as operating speeds.

FINE™/Design3D was used by Demeulenaere *et al.* (2004) to perform multi-point optimisation of an axial turbomachine compressor and turbine. The methodology employed by the FINE™/Design3D package involves a DOE database of CFD simulations, an ANN, a GA, and an objective function defined by the user. The multipoint optimisation was applied to the re-design of a NASA Rotor 37 transonic compressor rotor. According to Demeulenaere *et al.*, multipoint optimisation guarantees the performance of a turbomachinery component over a wide range of operating conditions.

Simpson *et al.* (2012) optimised the endwall profiles of a centrifugal compressor from the inducer section through to the vaneless diffuser outlet in order to reduce the compressor diffusion ratio. The DOE approach was used to investigate the design space. Transfer functions were built between the compressor loss coefficient and the design parameters by performing sample CFD calculations. The objective function of the optimisation algorithm was set to have as small a loss coefficient in the return channel as possible. The reduction in diffusion ratio yielded a significantly smaller, assembled machine size. This translated into reduced costs and space requirements.

2.3.4   Finite Element Analysis

Verstraete *et al.* (2010) performed FEAs in parallel with CFD simulations to obtain the maximum von Mises stresses in the compressor impeller during operation. The material used in the FEA was Titanium TI-6AL-4V. A total of 160,000 quadratic tetrahedral elements made up the structural mesh. Symmetry was applied to model only a periodic section of the impeller. It was shown that mechanical stresses could be drastically reduced with only a small decrease in compressor efficiency. Increasing the blade thickness at the hub was found to significantly reduce von Mises stresses while negligibly decreasing compressor efficiency. The blade curvature and leading edge height were also found to have a large effect on mechanical stresses. The trailing edge blade height had a direct influence on performance but only a small impact on mechanical stress.

Vick *et al.* (2009) performed FEA simulations to model centrifugal, pressure, thermal, and combined stresses experienced by a centrifugal compressor impeller during operation. Shaft dynamics and heat flow from the hot sections of the turboshaft engine to sensitive components such as the bearings were also investigated. If the CFD or FEA simulations revealed any problems that would be experienced during operation, the engine configuration was redesigned and analysed again.

A study of the unsteady flow through a centrifugal compressor was performed by Dickmann *et al.* (2006). The complex modal pressure data was imposed onto the meshed impeller structure and modelled using FEA. State-of-the-art calculations that analysed the behaviour of free vibrations on the impeller were followed by forced response calculations. The study showed that coupling CFD with FEA is a useful tool when doing fluid/structure interaction assessment at different operational conditions. It allows for the execution of parametric studies and the estimation of impeller life through High Cycle Fatigue analyses.

3 BENCHMARK ANALYSES

3.1   Introduction

The design of an impeller using a mean-line approach formed part of the objective of this project, as discussed in Section 1.1. The accuracy of the in-house mean-line code had to be verified by comparing the results obtained to those of a 3-dimensional, CFD analysis and experimental results. Both numerical analyses were performed on the same benchmark impeller geometry that was experimentally tested. This section contains details on the setup of the CFD and mean-line analyses, and the experimental test bench. The CFD is discussed first since the mean-line code required information from the CAD used for the CFD computational mesh.

The benchmark centrifugal compressor chosen for this project was the KKK k27 model shown in Figure 3.1. This impeller was designed for turbocharger application in the trucking industry. The k27 impeller is a popular performance component in the aftermarket modification of street cars. With the wide operating range and the high pressure ratios it delivers, it is a robust compressor capable of working with a variety of engine configurations. Several versions of the k27 impeller have been manufactured for application in different turbocharger systems. The difference between versions is the size of the impeller tip radius.
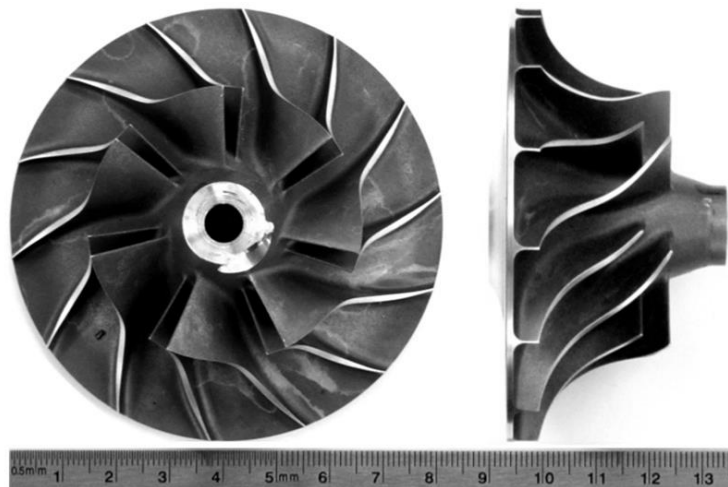
Figure 3.1: KKK k27 centrifugal compressor impeller. Ruler units in cm.

3.2   Impeller CAD

In order to perform a CFD analysis of the centrifugal compressor, a computational mesh had to be created. The mean-line code used in the project also required certain geometric parameters (throat area, throat angle, chord lengths, etc.). An accurate surface CAD model of the impeller was therefore required. NUMECA™

Autogrid5™ (Numeca International, 2011c) was used to mesh the compressor domain, the geometry being defined by a *geomTurbo* file.

3.2.1   *GeomTurbo* file format

This file format is used as input for the mesh generator NUMECA™ Autogrid5™. The file contains information on the geometry of the turbomachinery being modelled. Appendix C shows the structure of a *geomTurbo* file. It contains a header, hub and shroud contour curves, and blade pressure and suction side curves. These curves are all described by points in either cylindrical or Cartesian coordinate systems. Once NUMECA™ Autogrid5™ reads a *geomTurbo* file, it creates the respective surfaces: the hub and shroud surfaces by revolving their defining curves around the z-axis, and the blade surfaces by lofting the pressure and suction side curves, as seen in Figure 3.2.
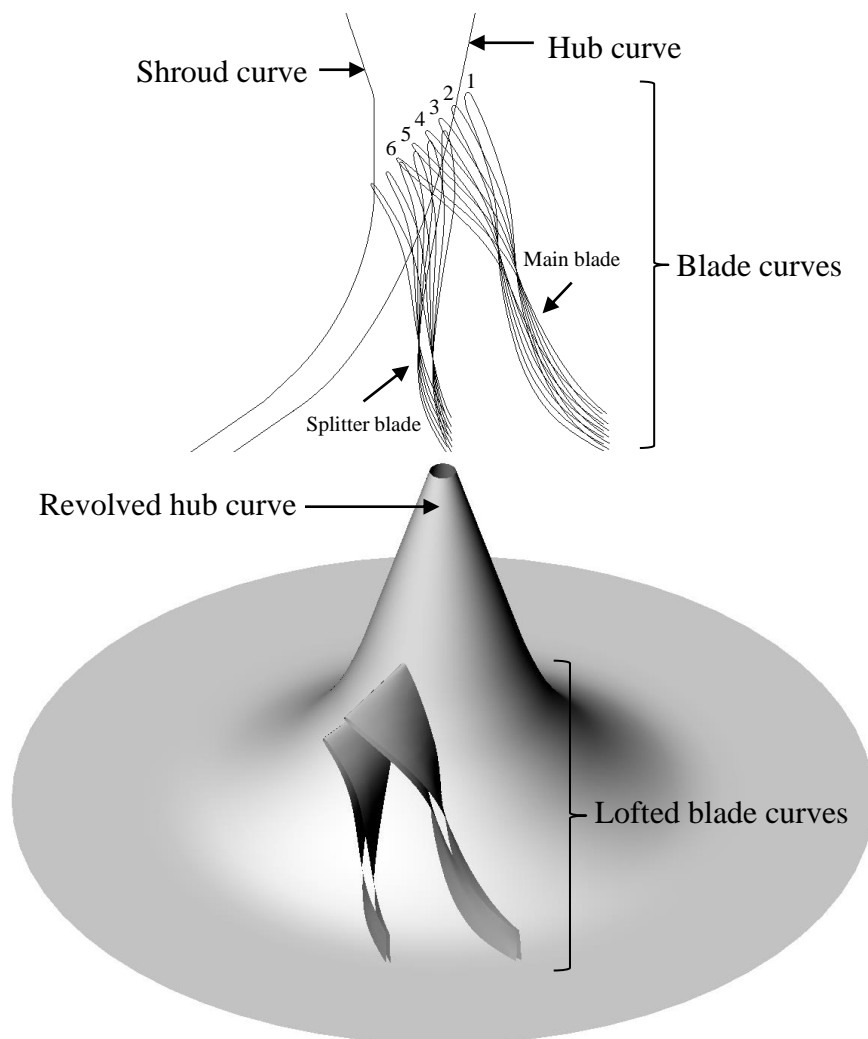
Figure 3.2: Curves and surfaces defining KKK k27 impeller geometry.

A *geomTurbo* file has a header, endwall curves, and a main and splitter blade curve section. The header section of the file is defined by the following lines:

```
GEOMETRY TURBO VERSION 3.7
geometric_tolerance 1e-006
blade_expansion_factor_hub 0.02
blade_expansion_factor_shroud 0.02
blade_merging +0
units 1
number_of_blades 7
```

The first line in the header outlines the format and version of the file. The next line, *geometric_tolerance*, defines the accuracy of the geometry relative to the units used, in this case millimeters. A value of 1×10^{-6} was used throughout.

The hub, shroud, and blade contours are defined separately in the file. Regions exist in the geometry where these contours intersect, ultimately creating boundaries in the computational domain. These intersections are found between the blade-hub and blade-shroud surfaces. The intersections can be defined more clearly if the blade surfaces are expanded through the hub and shroud surfaces so that the penetration of these surfaces is complete. The fractional value used to expand the surface edge (*blade_expansion_factor*) was 0.02. The total expansion of the surface is therefore the distance between corresponding points on the hub and shroud blade curves multiplied by this fractional value.

The unit of the points (meters, millimeters, etc.) written in the file is defined by the *units* entry. The number of blades, and in other words the number of periodic sections modelled by the CFD software, is given by the *number_of_blades* entry.

The data following the file header provides the coordinates of the points defining the various curves. Each set of coordinates is preceded by a description of the curve to which it belongs, e.g. SHROUD, HUB, SUCTION SECTIONAL, etc. This description is followed by the coordinate system and the number of points defining the curve. The shroud and hub endwall coordinates are the first to be defined, starting at the inlet side of the compressor. The next sets of coordinates are for the main blade suction, and then pressure curves. Again, starting at the leading edge and moving down towards the trailing edge. These are followed by the splitter blade suction and pressure coordinates respectively. The *# section* entry in the file denotes the blade section number, arranged from the hub (1) to shroud (6) sections. The intermediate sections (2 to 5) are virtual intersections of the blade surfaces with concentric hub-to-shroud surfaces.

A *geomTurbo* file is relatively easy to modify as all entries are clearly denoted with headings. A new *geomTurbo* can be generated in either one of three ways, using:

- NUMECA™ Autoblade (see Section 5.2)

- Custom code and impeller parameters
- Custom code and geometric measurements and/or scans

None of the impeller parameters, which are required by the first two options, were known at this stage so the third option was selected. In order to obtain a computer model of the compressor geometry, a device which could convert the physical surfaces of the impeller into digital point clouds was used. Work commenced on scans to create a dataset which was further processed using CAD software. These scans are discussed in Section 3.2.2.

3.2.2   Geometric scans

Initially, a Coordinate Measuring Machine (or CMM) at GCC in Stellenbosch was used to individually measure point coordinates on the impeller blades, hub, and shroud. These would then later be used to create surfaces representing the respective geometric features of the compressor. There were, however, some complications (see Appendix A) which led to the decision to use an optical scanner.

The optical scanner was a much less cumbersome tool compared to the CMM. Prior to scanning, the part was sprayed with a white, reflective powder coating. A single scan then created a point cloud of the geometry in view of the component lens. The scanner was re-orientated relative to the model in order to scan all the important geometric features. All individual scans were then superimposed using fixed coordinate stickers on the model. The resulting point cloud was exported in *stl* format to be processed by CAD software. The Atos 3D digitiser used to perform this scan was a GOM™ industries device. Figure 3.3 shows the point cloud model of the k27 impeller that was scanned.
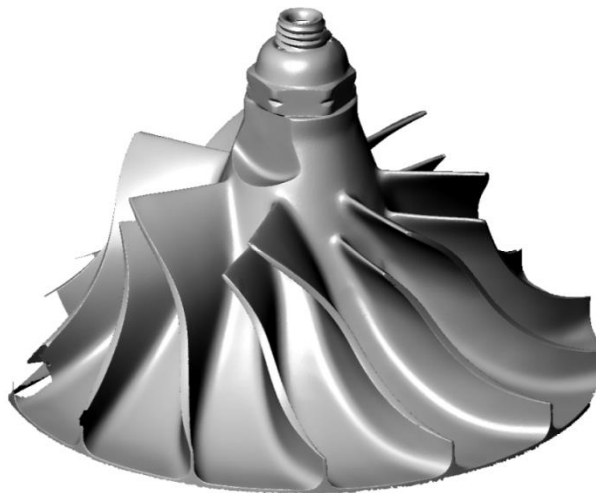
Figure 3.3: Impeller point cloud model from Atos 3D digitiser data (Rhinoceros3D®).

It should be noted that the model in Figure 3.3 is not a finished CAD surface model. The post processing of the point cloud data is detailed in Section 3.2.3 and Appendix A. The Atos 3D scans took about 1 hour to complete compared to the 6 hours for the CMM scans. The resulting point cloud was much denser than that of the CMM.

3.2.3   CAD and *geomTurbo* generation

   1) CAD

Once the point cloud was obtained, post processing of the data to create a surface CAD model commenced. This involved creating smooth surfaces from the still discrete and course point cloud profile seen in Figure 3.3. Surfaces were created for the main and splitter blades as well as for the impeller endwalls. Two CAD packages were utilised. PowerSHAPE® (Delcam, 2011) was used to fit initial surfaces and curves to the point cloud data and Rhinoceros3D® (Robert McNeel & Associates, 2011) was used to post process these objects. The details of the CAD creation are given in Appendix A.

   2) *GeomTurbo* generation code

In the code main function, the header (see Section 3.2.1) was the first part of the *geomTurbo* file to be written. Next, the shroud coordinates were imported and stored. The shroud coordinates were then sorted in order from impeller inlet to outlet. The same procedure was applied to the hub coordinates. After the points of each endwall were sorted, they were written to the *geomTurbo* file. Each set was preceded by its name, its coordinate system, and the number of points defining it.

The approach to sorting the blade section points was somewhat different. The points of each section were allocated to pressure side and suction side sets of the blade. These two sets of points shared a single coordinate at the leading edge of the blade section. This coordinate was computed by the code as the point where the difference between the normal angle (between points) and the virtual leading edge angle was the smallest. The normal angle was calculated between successive points (point 1 and 2 in Figure 3.4), starting from the pressure side trailing edge. As soon as an angle with the smallest difference was identified, the first of the two points (point 1) was set as the leading edge.

The approach of identifying the leading edge is illustrated in Figure 3.4. Once the leading edge point was located, it was set to be the first point in the list defining both pressure and suction sides. From here, the points on either side proceeded to the trailing edge of the impeller. Each set was again preceded by its name, its coordinate system, and the number of points defining the set.

All the sections for the main blade suction side were defined first, followed by the pressure side sections. Once the point coordinates of the main blade were written, the code started processing the splitter blade points. Before writing the splitter blade data, a header had to be placed just after the main blade data. In this header,

the splitter blade expansion factor was defined. The same value as that of the main blade was used. The same procedure for finding the leading edge of these points was applied and the points were written in the same format than those of the main blade.
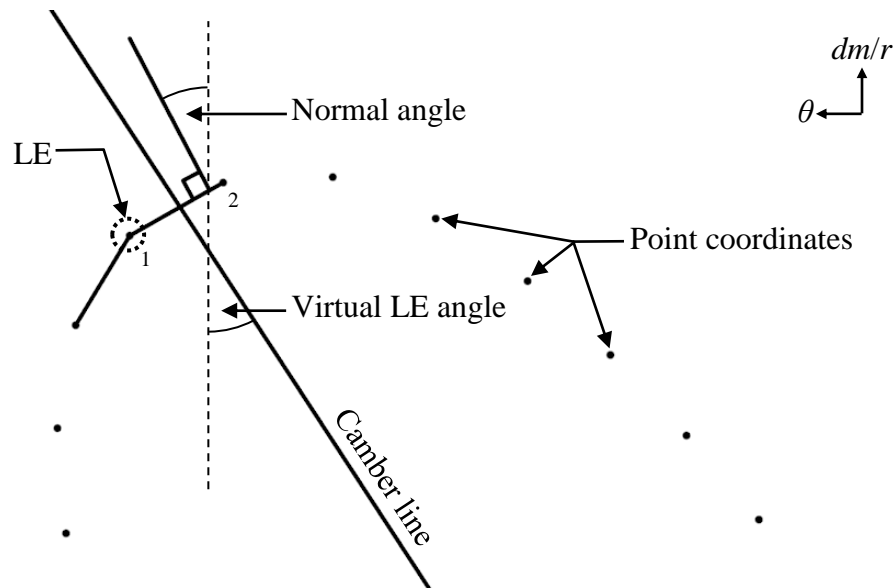
Figure 3.4: Definition of point coordinate leading edge for blade Section 1.

After all the point data was written to the *geomTurbo* file, the file was saved and closed. The next step in the analysis was to open the *geomTurbo* file with NUMECA™ Autogrid5™ and commence with the meshing of the computational domain.

3.3   Computational Domain

The computational domain for the benchmark CFD analysis stretched from the inlet of the turbocharger bell to the outlet of the vaneless diffuser, as seen in Figure 3.5. The dimensions of the compressor are shown in Figure 3.6 and Table 3.1. The geometry of the bolt which fastened the impeller to the shaft was not modelled.

As mentioned in Section 1.2, the fluid (atmospheric air) enters through the compressor inlet and proceeds toward the impeller eye. Here, the work done on the fluid by the rotating impeller increases the total pressure and temperature. The fluid propagates along the impeller blade passages until it reaches the outlet of the impeller. From here, no more work is done on the fluid as it moves over the step gap and through the vaneless diffuser to eventually exit the computational domain at the diffuser/volute interface. The inlet of the computational domain was located 20 mm above the leading edge of the main blade. It was modelled as a surface with a constant z-coordinate, in other words, parallel with the r-θ plane.
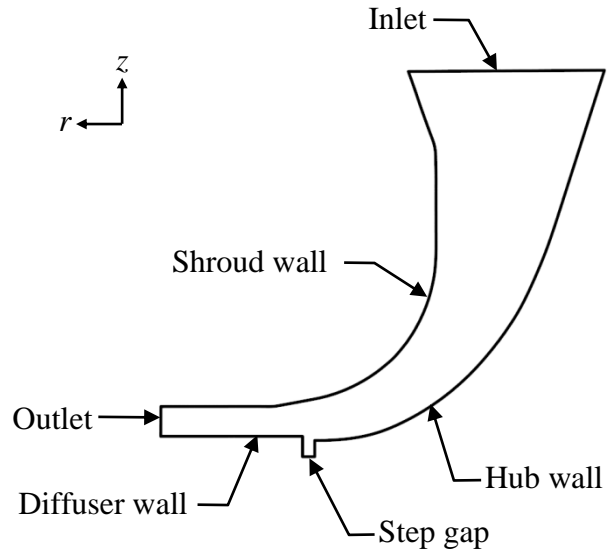
Figure 3.5: Meridional view of k27 computational domain.

The outlet of the computational domain coincided with the vaneless diffuser outlet. The outlet surface of the diffuser was located at a radius of $1.469r_2$. The vaneless diffuser was added to allow faster convergence of the simulations. It was modelled as having parallel walls, which corresponded with the measurements taken of the compressor. This meant that the flow area increased in the radial direction.

There existed a discontinuity between the impeller outlet and the vaneless diffuser in the form of a height difference, or step, between the impeller outlet and the lower diffuser wall (see Figure 3.6). The lower inlet plane of the diffuser would ideally line up with the impeller hub outlet. There was also a large radial gap between the impeller outlet and diffuser inlet. The step was added to the computational domain to model its effect on the impeller performance.

Table 3.1: Impeller dimensions [mm].

Parameter	Value
r_{1hub}	10.113
$r_{1shroud}$	25.522
r_2	40.439
r_3	59.408
b_3	4
b_{imp}	28.814
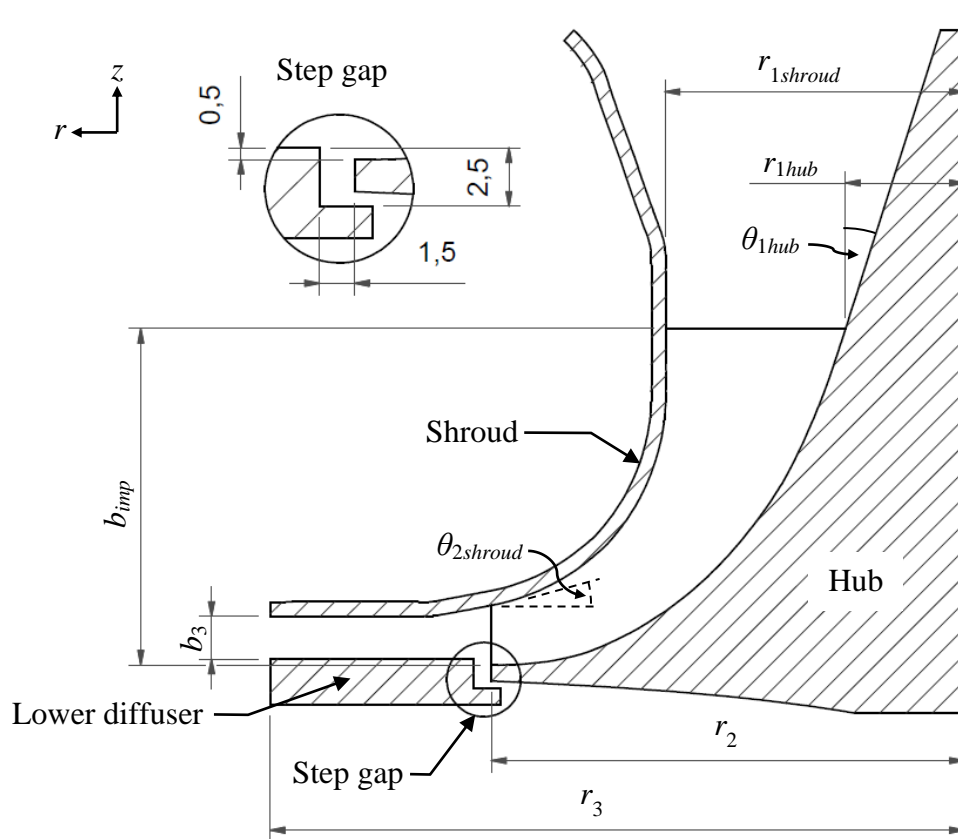
Figure 3.6: Meridional view of k27 geometry. Step gap dimensions in mm.

The computational domain did not include a volute since the focus of the project was on the impeller. Omitting the volute from an analysis is not uncommon (Ibaraki et al., 2003) as modelling a volute introduces axis asymmetry, which complicates meshing and increases computational time. Also, the project CFD analyses were performed at steady state; typical analyses that include volutes model unsteady conditions (Dickmann et al., 2006).

3.4　CFD Mesh Generation

NUMECA™ Autogrid5™ was used to create a structured mesh within the k27 compressor computational domain. Autogrid5™ was developed specifically for meshing turbomachinery geometry. It provides a platform from which to generate high quality structured meshes. It is, however, necessary to adjust some parameters in order to obtain a mesh of sufficient quality. Once the mesh has been generated, its defining parameters can also be used on different compressor geometries to create new meshes. Providing that the difference in geometric features is not significant, this ability of NUMECA™ Autogrid5™ facilitates compressor optimisation, which is discussed in Section 5.

3.4.1 Mesh components

The methodology used by NUMECA™ Autogrid5™ to create 3-dimensional meshes is based on conformal mapping between the 3-dimensional Cartesian coordinate system and 2-dimensional cylindrical surfaces of the blade-to-blade space in the *dm/r-θ* plane. This methodology can be summarised into the following components.

1) GeomTurbo

This component has already been discussed in detail in Section 3.2.

2) Meridional

This component projects surfaces of revolution, i.e. hub and shroud, onto the meridional plane (*r-z*) to create hub-to-shroud stream surfaces. In the blade passages, these stream surfaces are spaced from the blade root to tip, and in the clearance gap between the blade and shroud.

3) Blade-to-Blade

At this stage, 2-dimensional meshes are created on the stream surfaces created in the meridional space. This 2-dimensional generation allows the control of the mesh topology, the mesh point clustering, and the mesh orthogonality on each stream surface. A view of a blade-to-blade mesh is shown at 50% span in Figure 3.9.

4) 3-dimensional

Once the preceding components of meshing have been attended to, a 3-dimensional mesh is created. The use of conformal mapping conserves the quality obtained by the meridional and blade-to-blade meshes. This mesh quality is then transferred to the final, 3-dimensional mesh.

3.4.2 Mesh properties

The compressor was modelled using a total of 7 periodic volumes consisting of 1 main and 1 splitter blade each. These volumes were symmetrically arranged around the *z*-axis. An impeller *Rotational speed* of 120 krpm was specified.

The meshing process was complicated by the addition of *Blade fillets*. The fillets at the blade roots (r_{fillet} = 1.85 mm) were relatively large compared to the blades. At the impeller inlet, the size of the fillet radius was equal to 12% of the blade height. This caused neighbouring fillets to be in close proximity to each other. As a structured mesh was to be created, the same number of mesh cells had to fit into the blade-to-blade plane at both the hub and shroud. The hub blade-to-blade surface area was also much smaller compared to that of the shroud, largely due to the presence of the blade fillets. This led to the cells on and near the hub blade-to-blade plane having low orthogonalities (lower than 20°) as the cells effectively had to be "squeezed" into a smaller area.

Although it was possible to add blade fillets and create a mesh with good quality, it was decided to omit the fillets from the CFD analyses. The decision was strongly influenced by the fact that the optimisation process in Section 5 required that the same mesh settings be applied to create 90 different meshes for as many different geometries. For the sake of consistency, the fillets were omitted from all analyses. The time required to include these fillets could not be justified by their effect on compressor performance.

The *Clearance gaps* were assigned a value of $t = 0.45$ mm at both the leading and trailing edges of the impeller blades.

The *Wall cell width* on the impeller surfaces was calculated to facilitate a y_1^+ value of between 1 and 10 on these surfaces. The choice of y_1^+ range was determined by the turbulence model that was used, as discussed in Section 3.5.2. The cell width at the wall, y_{wall}, was calculated using the truncated series solution of the *Blasius* equation for turbulent flows (Numeca International, 2011c):

$$y_{wall} = 6 \left(\frac{V_{ref}}{\nu}\right)^{-\frac{7}{8}} \left(\frac{L_{ref}}{2}\right)^{\frac{1}{8}} y_1^+ \tag{3.1}$$

where V_{ref} can be taken as the average inlet velocity, ν the kinematic viscosity, and L_{ref} the reference length. The reference length used was that of the camber line describing the main blade. A value of 6 μm was calculated for y_{wall}.

The obtained y_1^+ values on the walls were well within the required range of 1 to 10. The only region where the upper limit of 10 was exceeded was at the blade tips. This phenomenon is explained in the NUMECA™ Autogrid5™ Manual (Numeca International, 2011c) and attributed to the fact that blade clearance gaps are meshed with uniform spanwise node distributions. The y_1^+ values in these regions tend to be higher than the average since the corresponding cell widths are larger. This is because flow over the tip surfaces is highly sheared and vortical and cannot be modelled as normal boundary layer flow.

The next step in the meshing procedure was to specify a node target number. This number was the number of nodes to be contained in the final 3-dimensional mesh. A blade-to-blade mesh at 50% span was generated and the *Mesh Wizard* closed. The next step was to edit the properties of the 2nd and 3rd components (see Section 3.4.1) of the mesh. This step was essential as it increased the quality of the mesh. The mesh quality criteria are defined in the Section 3.4.3.

The *Blade topology* used during the meshing of the computational domain was an H&I topology. This topology is typically used for compressor impellers that have splitter blades. Figure 3.7 shows the different mesh blocks that make up a blade-to-blade plane for the H&I topology. The topologies for both blades were each preceded by an inducer block containing 29 points in the streamwise direction and

extended by a discharge block with 21 streamwise points (see Figure 3.9). An O block skin mesh with 25 points was included around the main and splitter blades.
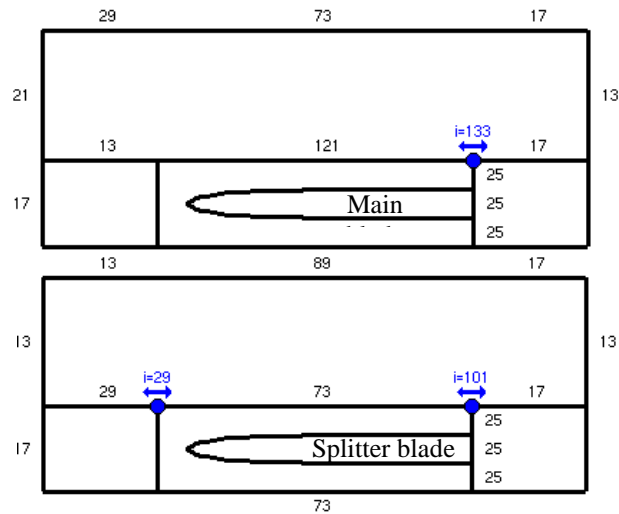
Figure 3.7: H&I topology for main and splitter blades. Note the node distributions and amounts on the mesh blocks.

The number of nodes on the edges of the mesh blocks in Figure 3.7 can be adjusted to increase or decrease the amount of cells in the final 3-dimensional mesh. This is also a way in which the quality of the mesh can be adjusted. The adjustment of the number of nodes must be done carefully as NUMECA™ Autogrid5™ creates multiple mesh levels, called a multigrid system. It effectively clusters combinations of cells into larger, courser cells. During simulation, the courser grid quickly provides a solution with small residuals. This solution is then interpolated onto the finer grid. The process is recursively followed until the finest grid is reached. This procedure is called *Course Grid Initialisation.* The number of multigrid levels depends on the number of nodes used to mesh the configuration shown in Figure 3.7.

The *Optimisation* of the mesh determines the optimum distribution of nodes inside the mesh blocks, the optimum being defined as the distribution having the best mesh quality. The optimisation itself is performed in the blade-to-blade space and controlled by the number of optimisation steps, by default set to 200 steps. After some initial meshing of the computational domain, it was found that 180 optimisation steps provided the best quality mesh.

A *zr-effect* was added to the computational domain to model the step gap shown in Figure 3.6. The meshed gap is shown in Figure 3.8. Note the interface between the step gap mesh and the rest of the meshed domain (the domain mesh is not shown in Figure 3.8). The interface is a full non matching periodic interface. The step gap is modelled as a volume consisting of 7 periodic sections.
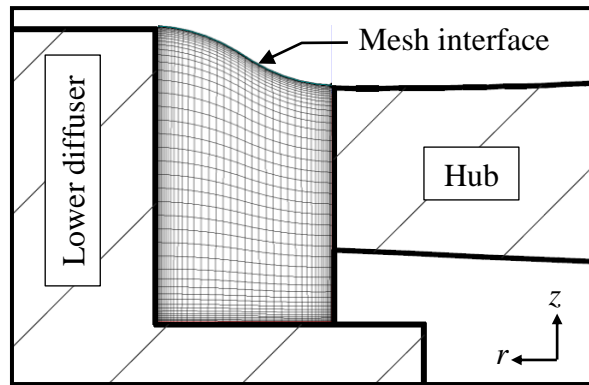
Figure 3.8: Meridional view of step gap mesh.

Once all the mesh properties were adjusted and set, a 3-dimensional mesh was generated. This was done by generating blade-to-blade meshes on the stream surfaces defined in the meridional mesh plane. The *Span interpolation* was set to 2%. This meant that the blade-to-blade mesh would only be optimised at 2% increments of the hub-to-shroud height. All the blade-to-blade meshes lying in-between were generated with the same properties as the preceding, optimised mesh (Figure 3.9).

The blade-to-blade mesh at 50% span seen in Figure 3.9 had a total of 17 mesh blocks, including the *zr-effect* block. The final 3-dimensional mesh had a total of 1,846,597 nodes with 3 multigrid levels.
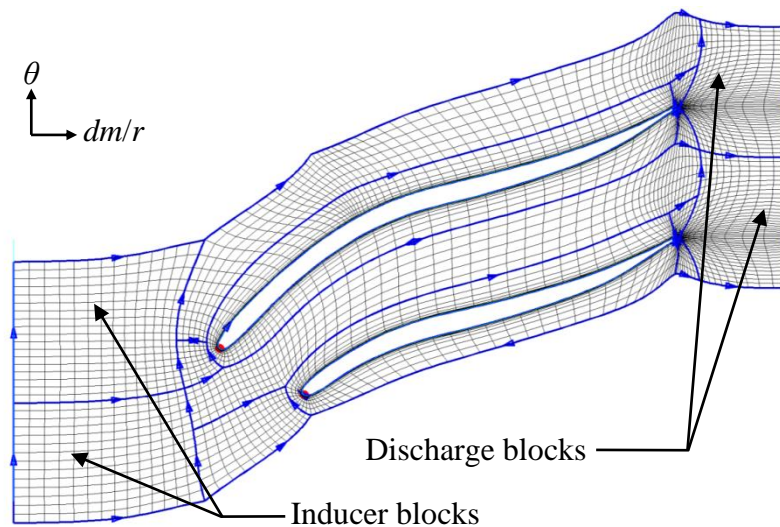
Figure 3.9: Blade-to-blade mesh at 50% span (2nd multigrid level). The blue edges are those of the mesh blocks (NUMECA™ Autogrid5™).

3.4.3   Mesh quality

There are several quantities that contribute to the overall quality of the computational mesh. NUMECA™ Autogrid5™ allows the user to inspect these

quantities and adjust the mesh properties defined in Section 3.4.2 to improve the overall mesh quality. These quantities are the following:

- Orthogonality, the minimum angle between the edges of a cell. This angle is measured in all directions and has a value between 0° and 90°.
- Expansion ratio, the size variation between two adjacent cell surfaces in a specific direction. The range lies between 1 and 100.
- Angular deviation, the angular variation between two adjacent cell surfaces all directions. The range lies between 0° and 180°.
- Aspect ratio, the length of a cell divided by its width. The value ranges from 1 to 50,000.

The criteria used in this project to define a good quality mesh are given in Table 3.2. The required values for the individual mesh properties were identified through correspondence with the CFD software support group (Numeca International, 2011b). For the k27 mesh, this criterion was met in most of the mesh blocks. The "worst" values obtained for the entire mesh are also shown in Table 3.2, as well as the percentage of "bad" cells for each respective quantity.

Table 3.2: K27 mesh quality.

Quantity	Required value	"Worst" value	% "bad" cells
Orthogonality	$> 20°$	20.4°	0%
Expansion ratio	< 2.5	2.53	0.003%
Angular deviation	$< 40°$	25°	0%
Aspect ratio	< 2100	255	0%

Details on the mesh dependency study are given in Appendix G. This study was done to rule out the effects of mesh density on any calculated results.

3.5 CFD Flow Generation

3.5.1 Fluid model

The fluid used in the CFD simulations was atmospheric air with real gas properties. The values of c_p and γ were therefore a function of temperature. The real, or thermally perfect, gas model of NUMECA™ FINE™/Turbo is based on two equations, namely the perfect gas relation

$$p = \rho RT = \rho \frac{R_o}{M} T \tag{3.2}$$

and the enthalpy equation

$$h = \int_{T_0}^{T} C_p dT \; = \; \int_{T_0}^{T} C_v dT \; + RT \tag{3.3}$$

The lower bound of the integral in equation (3.3) is T_0, which is the simulation reference temperature. The reference temperature is taken as the lowest temperature in the computational domain. This temperature value is located at the compressor inlet. The resulting equation

$$RT = \int_{T_0}^{T} (C_p - C_v) dT \tag{3.4}$$

assumes a constant value of R (287 J/(kg·K)). Also, C_p is provided as a function of temperature, with γ then calculated as

$$\gamma = \frac{C_p}{C_p - R} \tag{3.5}$$

The use of the real gas model is recommended by the NUMECA™ FINE™/Turbo Manual (Numeca International, 2011d). The other models available for air are perfect gas and incompressible gas models. The perfect gas model assumes a constant specific heat at all temperatures. The incompressible gas model either assumes constant density, or predefines the density as a function of pressure.

3.5.2   Flow model

A turbulent Navier-Stokes flow solver was used to perform the CFD simulations (Benini and Giacometti (2007), Simpson *et al.* (2012), Verstraete *et al.* (2010), and Tamaki *et al.* (2009)). Steady state compressor operation was the basis of all simulations. No transient or harmonic effects were analysed as they did not form part of the project scope. The same approach was used by Verstraete et al. (2010) and Hildebrandt et al. (2008). Also, as mentioned in Section 3.4.2, the compressor was modelled using periodic, axisymmetric volumes.

To accurately model turbulence, the simulation results of four different models were compared. These were the Spalart-Allmaras, Baldwin-Lomax, k-epsilon, and k-omega models. The deviation in the resulting pressure ratios and efficiencies at the outlet of the computational domain did not exceed 3%. The k-epsilon model did not require as fine a boundary layer mesh as the Spalart-Allmaras and Baldwin-Lomax models. However, it resulted in longer computational times because of its 2-equation approach. The same went for the k-omega model. The final choice of turbulence model therefore lay between the Spalart-Allmaras and Baldwin-Lomax models. The Spalart-Allmaras model simulates turbulent quantities more accurately. It is used by Tamaki (2012) to model an impeller of

similar size and performance. Therefore, the one-equation Spalart-Allmaras model was selected to model turbulence.

3.5.3 Boundary conditions

All the boundaries of the numerical model (except the step gap) were defined in the *geomTurbo* file. The dimensions are given in Figure 3.6. The computational domain consisted of 4 boundary groups:

    1) Inlet boundaries

A subsonic inlet boundary was modelled since the flow velocity normal to this boundary is lower than the speed of sound. A cylindrical coordinate system was used to define flow properties. Total quantities for pressure and temperature were defined at the inlet plane of the computational domain. These properties are shown in Table 3.3. Flow was assumed to have no pre-swirl at the inlet and was therefore constrained in the axial direction (negative z-direction) across the inlet boundary. This was done by selecting a *V extrapolated* velocity direction boundary condition which constrains the V_r, V_θ, and V_z velocity components. $V_r/|V|$ and $V_\theta/|V|$ were set to zero (no inlet pre-swirl) and $V_z/|V|$ equal to -1.

Table 3.3: Inlet boundary imposed quantities.

Property	Value
$V_r/|V|$	0
$V_\theta/|V|$	0
$V_z/|V|$	-1
Absolute Total Pressure	101.325 kPa
Absolute Total Temperature	293 K
Turbulent Viscosity	0.0001 m^2/s

    2) Outlet boundaries

A subsonic*, Mass Flow Imposed* outlet boundary condition was selected to perform the computations. An initial outlet static pressure was defined along with an outlet mass flow rate. The initial outlet static pressure was used by the flow solver to start the simulation computation and was set to 150 kPa. A *Pressure Adaptation* technique is used by NUMECA™ FINE™/Turbo to impose a mass flow by automatically modifying the outlet pressure during the computation process. This ensures that after convergence, the prescribed mass flow rate is obtained.

The k27 compressor operation was simulated at three speeds, namely 80, 100, and 120 krpm. The mass flow rate varied from 0.12 to 0.275 kg/s for the 80 krpm simulations, and from 0.2 to 0.3 kg/s for the 100 krpm simulations. For the 120 krpm simulations, the mass flow rate ranged from 0.25 to 0.31 kg/s. The mass flow range at different speeds varied since the surge/choke range for centrifugal impellers differs at increasing rotational speeds (see Section 1.2.2).

The *Backflow Control* option was selected in NUMECA™ FINE™/Turbo. This option controls the total temperature of the reverse flow at the outlet plane. The total temperature of the reverse flow is adjusted so that it has the same averaged value as that of the exiting flow.

3) Periodic boundaries

When the mesh of the computational domain is created, all the properties of the periodic boundaries are automatically defined. These properties are then transferred to NUMECA™ FINE™/Turbo when the mesh file is imported. This procedure eliminates the need for any user input regarding the definition of periodic boundary properties.

4) Solid boundaries

The solid, or wall, boundaries included were the impeller hub, shroud, blade surfaces, and step. The shroud and step walls remained static during simulation. The blades and hub rotated at the same speed. A smooth surface and no heat transfer (adiabatic flow) was assumed for all the wall boundaries.

3.5.4   Control variables

As mentioned in Section 3.4.2, NUMECA™ Autogrid5™ creates meshes using a multigrid approach. This enabled the use of the NUMECA™ FINE™/Turbo *Course Grid Initialisation* function. There were three multigrid levels, arranged from fine to coarse. The third and second levels were set to run until they met convergence criteria of either residuals of less than 10^{-4}, or 500 iterations. Once the criteria were met, the simulation would move on to the lower respective grid level. A central discretisation scheme was applied for all the grid levels during simulation.

Once the simulation moved on to the finest multigrid level, the convergence criteria were set to a maximum of 2000 iterations or residuals smaller than 10^{-4}. Whichever one of the criteria was met first depended on the operational parameters and boundary conditions. The solver precision was set to *Single*; this option was sufficiently accurate while not being too demanding on computer memory.

3.5.5   Output values

The values that were computed at each node were the following:

- Thermodynamics: Static and total absolute temperature, static and total absolute pressure, density, and entropy.
- Velocities: Absolute velocity magnitude, absolute velocity vectors, absolute Mach number, relative velocity magnitude, relative velocity vectors, relative Mach number.
- Turbulence: Wall distance, turbulent viscosity, y^{+} value in first inner cell.

During simulation, the convergence of the global residual, pressure ratio, efficiency, and inlet/outlet mass flow rate could be monitored. The magnitudes of these values were computed using a weighted integral over the outlet surface of the computational domain. To check the convergence of the computation Numeca International (2011c) recommends the observation of the development of multiple criteria, including:

- an adequate decrease in residuals (minimum 3 orders of magnitude).
- complete stabilization of global performances.
- stabilization of mass flow in/out, with satisfactory correspondence (usually less than 0.5% difference between in/out).

3.6 Mean-line Analysis

An in-house mean-line code which predicts the performance of a centrifugal compressor at a specific operating point was compiled by De Wet (2011). This operating point was defined by two known operational parameters of the compressor, for example air mass flow rate and impeller speed. All other variables and loss coefficients specific to the operating point were then iteratively calculated. The mean-line code was developed by following a procedure outlined in Aungier (2000). Different work input and loss coefficients were imposed between the inlet and the outlet section of the compressor impeller. The correlations used to calculate these coefficients are discussed in Appendix B.

The general procedure for the mean-line calculation of compressor performance is well known (Schiffmann and Favrat, 2010). The procedure used by the in-house code was similar to that of Schiffmann and Favrat. The compressor impeller was modelled at different sections, namely the inlet, throat, and outlet. First, the inlet velocity triangle and air density were iteratively computed at standard atmospheric conditions. The same was done at the throat of the impeller, using the properties calculated at the inlet as initial values. Finally, the air properties at the impeller outlet and the useful and parasitic work required to compress the air were calculated. All the internal loss coefficients were added and the loss in total pressure calculated iteratively. Finally, the compressor impeller pressure ratio and efficiency were calculated.

3.6.1 Modification of in-house code

Because the operation of a centrifugal compressor is not constrained to a single point (i.e. mass flow rate, impeller speed), it was necessary to create a compressor chart showing the predicted performance over a wide range of mass flow rates and impeller speeds. The in-house code was modified to achieve this goal. This was done by calculating the performance of the impeller at a range of impeller speeds and mass flow rates while testing for stall and choke conditions at the impeller inlet and throat respectively. The performance curves at five different impeller

speeds (80 to 120 krpm) were calculated. The equation used to test for stall is given by Aungier (2000):

$$W_{1s}/W_{th} \geq 1.75 \tag{3.6}$$

In the event of choke, the mean-line code was tested at incremental mass flow rates until the choke loss coefficient, $\overline{\omega}_{CH}$ in equation (3.7) (Aungier, 2000), reached a value higher than 1.1. This value was selected following a range of test runs of the code; it was found to give a wide representation of mass flow rates at choked conditions. The approach used to calculate A_{th} is outlined in Appendix B.

$$\begin{aligned}
X &= 11 - 10 C_r \frac{A_{th}}{A^*} \\
\overline{\omega}_{CH} &= 0 \qquad X \leq 0 \\
\overline{\omega}_{CH} &= \frac{1}{2}(0.05X + X^7) \qquad X > 0
\end{aligned} \tag{3.7}$$

Once the operational range of mass flow rates at the different impeller speeds was identified, a compressor chart was created. This chart showed the performance curves at each incremental impeller speed, as well as the surge line indicating where impeller stall was likely to commence. An example of this chart can be seen in Appendix D, Figure D.3.

3.6.2 Mean-line code setup

The same boundary conditions used in the CFD were applied to the mean-line simulations. The inlet velocity was in the axial, z-direction. The total quantities imposed at the inlet were at default atmospheric conditions (p_{total} = 101.325 kPa and T_{total} = 293K). The range of mass flow rates used to calculate the compressor performance and test for stall and choke was between 0.09 and 0.4 kg/s at all impeller speeds. The main parameters describing the compressor geometry were used as an input to the mean-line code and are shown in both Table 3.1 and Table 3.4.

Table 3.4: K27 compressor main parameters.

Parameter	Value
z_{imp}	7
β_{1hub}	58°
$\beta_{1shroud}$	30°
β_2	57°
θ_{1hub}	5°
$\theta_{2shroud}$	10°
LE_{hub}	1.52 mm

LE_{shroud}	0.817 mm
TE	0.488 mm
t	0.45 mm

3.7 Experimental Setup

The test bench in Figure 3.11 was designed and constructed by Struwig (2012) to measure fluid properties in a turbocharger compressor during operation. The benchmark turbocharger was the KKK k27 model mentioned earlier in this section. The fluid static temperature was measured at the compressor inlet and downstream of the volute outlet. For the purpose of comparison between experimental and CFD results, three other properties of the compressor were monitored during operation:

- Mass flow rate [kg/s]
- Impeller speed [rpm]
- Static pressure [kPa]

The compressor **mass flow rate** was measured at the inlet bell mouth using a differential pressure transducer (Hottinger Baldwin Messtechnik, 2011a). This mass flow rate was controlled by a throttle valve located downstream of the compressor outlet. The **impeller speed** was measured using a reflective switch (OPTEK Technology Inc., 2011).

The **static pressure** was measured 6 mm downstream of the impeller outlet, as well as at the diffuser outlet, using two pressure transducers (Hottinger Baldwin Messtechnik, 2011b). Four pressure taps were used at both the impeller and diffuser outlet to circumferentially average the static pressure measurement. Two of the pressure taps can be seen in Figure 3.10. The pressure taps at the impeller outlet could not be located further upstream due to interference with the lower surface of the diffuser (compressor backplate).
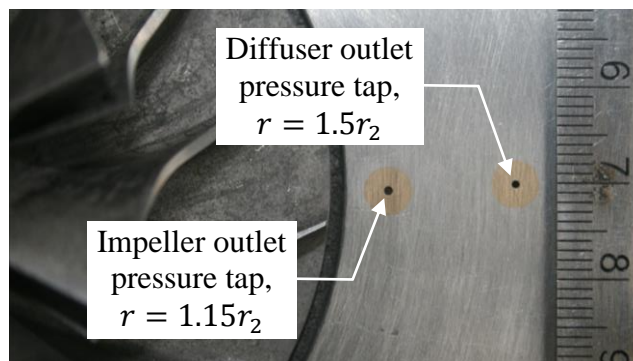
Figure 3.10: Pressure taps at impeller and diffuser outlet. Ruler units in cm.
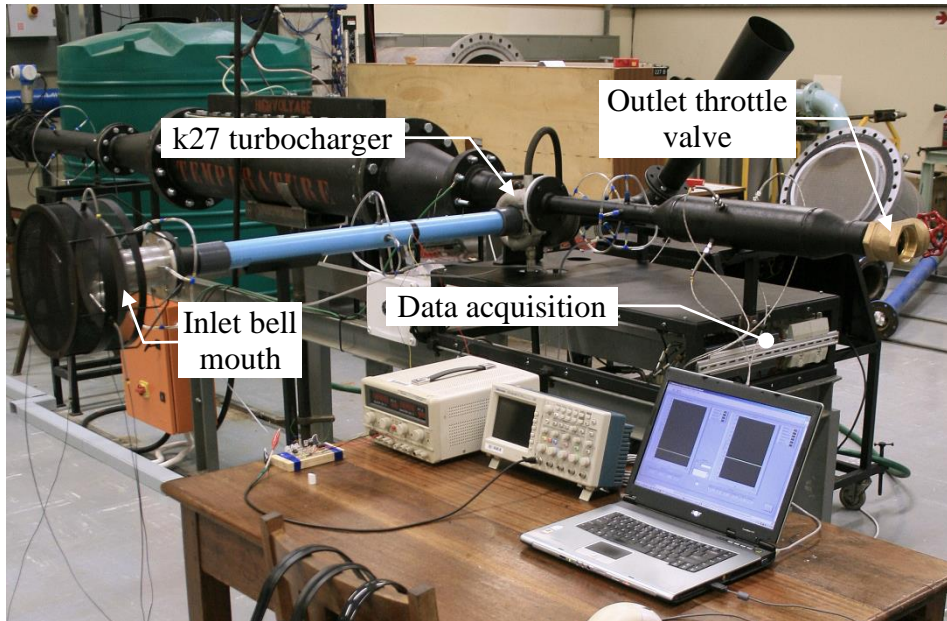
Figure 3.11: Compressor test bench.

3.8 Comparison of Results

Figure 3.12 and Figure 3.13 show the performance curves of the benchmark compressor, as calculated by the mean-line code and CFD, and measured using the test bench described in Section 3.7. The curves represent pressure ratios, isentropic efficiencies, and temperature ratios drawn along data points acquired at specific mass flow rates at constant impeller speeds. The lower and upper limits of mass flow rates were constrained by compressor surge and choke, respectively, at the different impeller speeds.

The occurrence of surge and choke was predicted by the mean-line (see Section 3.6.1) and CFD calculations. The onset of instability in the CFD calculations is not equivalent to compressor instability, surge, or stall. There is, however, a strong correlation with undesirable flow characteristics, such as flow separation (Tamaki, 2012). CFD instability was therefore used as an indication of impeller instability. Flow calculation typically became unstable at lower mass flow rates. This served as an indication of compressor stall or surge.

The first apparent difference between mean-line and CFD results in Figure 3.12 is the higher mass flow rates at which surge and choke are predicted by the mean-line code. This difference is relatively small at lower impeller speeds. It does, however, increase significantly as the speed increases. This is most probably due to the complex, 3-dimensional nature of flow inside the k27 impeller passages at high pressure ratios, as discussed in Section 5.9.

The values of the pressure ratio performance curves near the impeller maximum efficiency points (MEPs) were similar (maximum difference of 0.9%) for the mean-line and CFD calculations, albeit at higher mass flow rates for the former. The same applied to the performance curves of isentropic efficiency, where the maximum difference in efficiencies at the MEP was about 3%. The gradient of the pressure ratio performance curves also differed, with the mean-line calculated performance curves being consistently flat (except at choke) and the CFD calculated curves being skew, becoming skewer (steeper gradient) as the impeller speed increased. This can be attributed to the highly 3-dimensional flow at high impeller speeds, and the splitter blade leading edge being located too close to the impeller throat (see Section 5.8).

The performance curve marked "Aungier (120 krpm)" in Figure 3.12 was calculated with the code of Aungier (2000). The curve was added to compare with the results of the code compiled by De Wet (2011), which applies the same theory and flow models as Aungier's code.
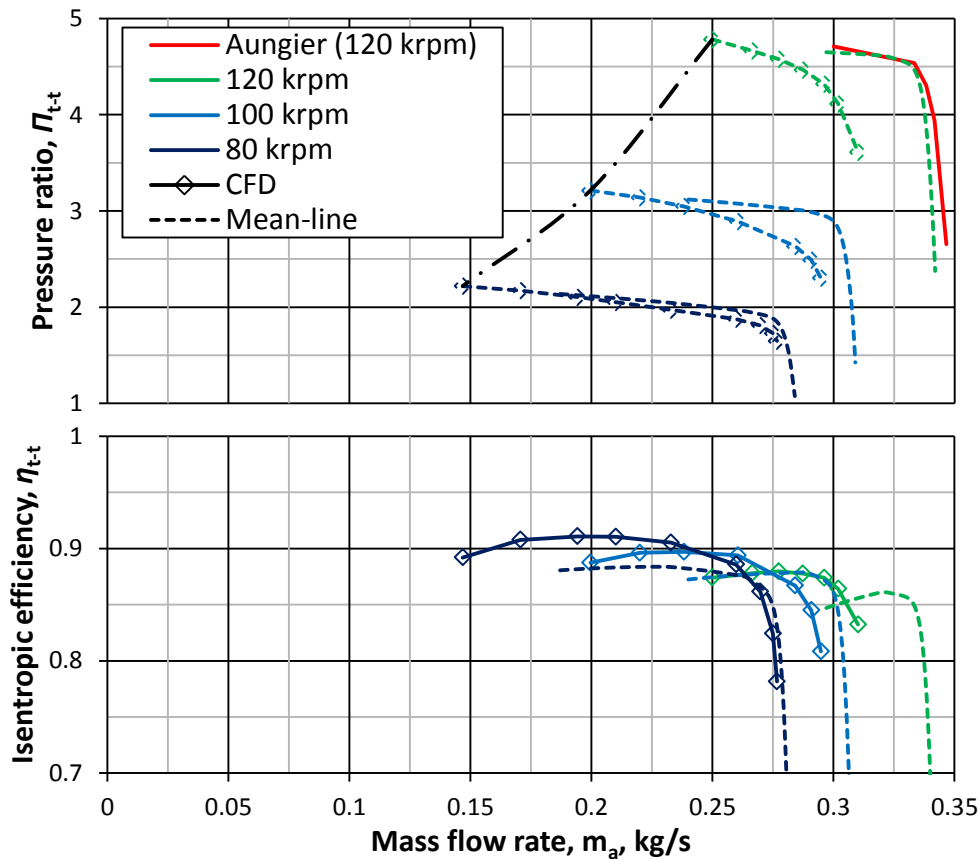
Figure 3.12: Benchmark mean-line and CFD results of pressure ratios and isentropic efficiencies at impeller outlet.

The compressor test bench was operated at conditions different than those of the CFD simulations. The measured mass flow rates were therefore corrected. The

compressor was tested at choked conditions, at the upper limit of the mass flow rate range, and near surge at the lower limit. The compressor was not tested at surge as the effects of surge on the test bench had not been studied. The compressor was tested at speeds of 80 and 100 krpm. The CFD calculated and experimentally obtained performance curves are shown in Figure 3.13.

There are two performance curves at each of the impeller speeds. The curves represent the total-to-static pressure ratio, measured and calculated just downstream of the impeller, and at the diffuser outlet. The difference in static pressure between the constant speed curves was due to static pressure recovery within the vaneless diffuser.

From Figure 3.13, it can be seen that the pressure ratio during and prior to compressor choke is well predicted (if slightly overpredicted) by the CFD, at both impeller speeds. At 80 krpm, the measured data corresponded well across the whole mass flow rate range, with the maximum difference in results being 5.6%. At an impeller speed of 100 krpm, the results deviated further, near the lower limit of mass flow rate. The maximum deviation was 6%. The larger deviation corresponded to a smaller gradient for the experimentally obtained performance curves, as compared to the CFD. This translated into a lower surge margin for the tested compressor, with the design pressure ratio and speed being similar for both cases, and assuming similar surge mass flow rates.

The exact cause of the deviation in results was not identified. There were, however, some differences in geometry between the experimental and CFD compressor models. These were the blade fillets (see Section 3.4.2) and the compressor volute (only present in the experimental model). CFD simulations showed that the addition of blade fillets lead to a reduction of about 2% in pressure ratio across the whole mass flow rate and speed range. This decrease in pressure ratios would bring the CFD results closer to those of the experiments.

The values of total temperature measured at the compressor volute outlet are compared with the CFD calculated values at the diffuser outlet, as temperature ratios (equation (3.8)), in Figure 3.13. It is clear that the magnitudes of the temperature curves in the graph differ (the CFD values are overpredicted), whereas the slopes of the curves are very similar, especially at the higher speed of 100 krpm. This indicates good qualitative agreement between results, the maximum difference in results being about 5%.

$$\theta_{t-t} = \frac{T_{0n}}{T_{01}} \tag{3.8}$$

One of the reasons for the difference between calculated and measured temperatures was the assumption of adiabatic flow in the CFD analysis. The implications of such an assumption are discussed in Section 2.2. When the tests were performed there was definite heat loss to the atmosphere as none of the

components had been thermally insulated. A significant amount of surface area (particularly the area leading up to the temperature measuring point after the volute) was exposed to atmospheric temperature, as can be seen in Figure 3.11.
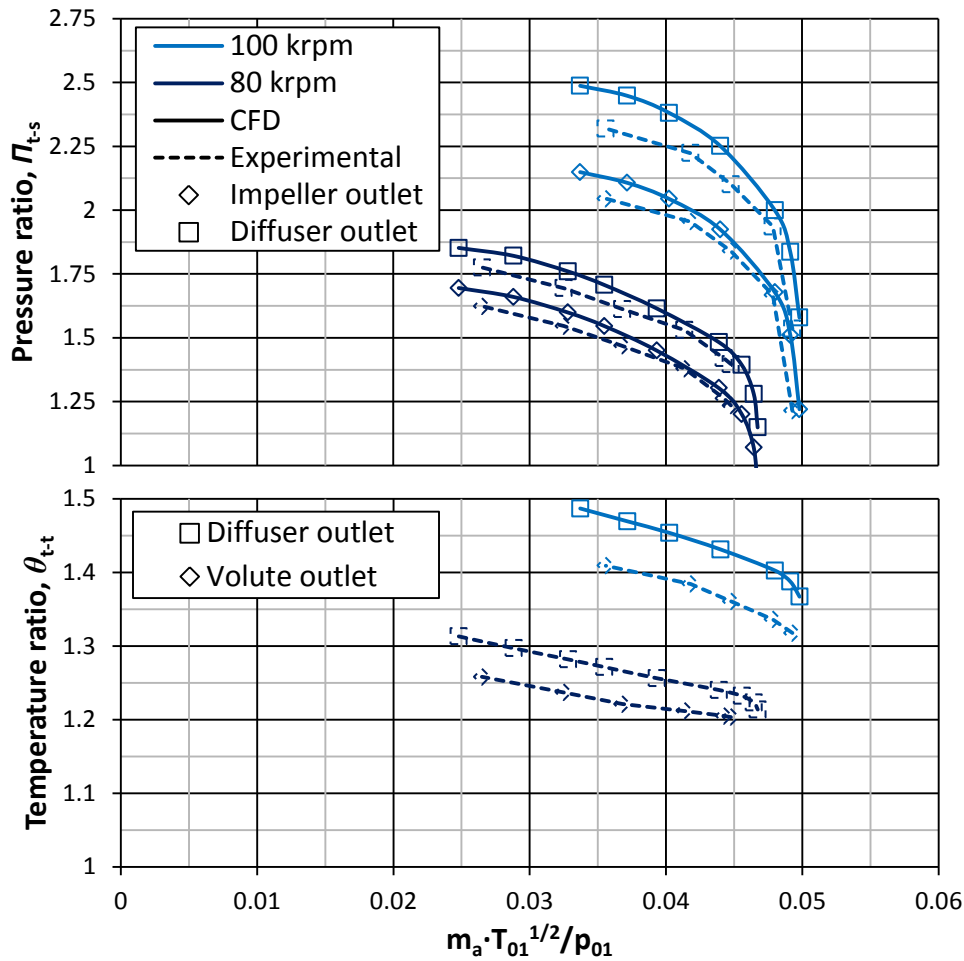
Figure 3.13: Benchmark impeller experimental and CFD results.

In addition to convection, heat was lost through conductance from the hot compressor to the cold turbine: the turbine pressure drop cooled down the air used to power the system. The air upstream of the turbine had a total temperature equal to the atmospheric air temperature. The turbine outlet air temperature was below 0°C at speeds higher than 80 krpm.

The results shown in Figure 3.12 allowed the mean-line code to be used, with some confidence, to create a new impeller design. The performance calculated for this design still had to be verified using CFD. This was important, for example, to calculate mass flow rate ranges more accurately. Figure 3.13 shows that there was good agreement between the experimental and CFD results. CFD could therefore be used, initially, to verify the mean-line impeller design performance (see Section 4.5) and to obtain an aerodynamically optimised, final impeller design (see Section 5).

4 MEAN-LINE IMPELLER DESIGN

4.1 Introduction

The mean-line code discussed in Section 3.6 was used to calculate the performance of a range of impellers, the dimensions of which fell within specified bounds. The geometry of each impeller was created manually and then tested using the mean-line code. However, in order to test the wide range of impeller geometries, it was necessary to create these geometries automatically. The performance of each impeller was then calculated. The "best" performing impeller geometry was selected and a CFD simulation was done using this geometry. The CFD results were subsequently compared with mean-line results in a screening process.

4.2 Impeller Bounds

The most important factor influencing the design of a centrifugal compressor, with a specific performance objective, is the limitations set on its geometry. In this project, the most significant limitation on the impeller geometry was its outlet diameter. The diameter was constrained to a maximum value of 75 mm. The overall compressor geometry was constrained by the dimensions of the MGT. The inlet diameter of the impeller was constrained to a maximum value of 58 mm, while the outlet blade height was fixed at 6 mm.

The design point mass flow rate of the compressor was 0.325 kg/s at 121 krpm. It was required that the compressor deliver a pressure ratio (total-to-total) of 4.72 at an isentropic efficiency (total-to-total) of 79.8%. These values were to be obtained at the diffuser outlet.

4.3 Impeller Geometry

The mean-line design geometry needed to adhere to certain dimensional bounds. This required the creation of a MATLAB computer code which could quickly generate the impeller geometry from a set of parameters falling within these bounds. The same geometry would then have to be exported as a *geomTurbo* file to be meshed in NUMECA™ Autogrid5™. The required geometry included the meridional contours of the hub and shroud, the camber line of the main and splitter blades, the blade thickness distribution normal to the camber line, and the number of blades. A flow chart of the MATLAB code used to generate the geometry has been added as Appendix D.

4.3.1   Endwalls

The hub and shroud contours were the first to be created. As defined by a *geomTurbo* file (see Section 3.2.1), the contours were created in the meridional plane. The endwall contours each consisted of an inlet, bladed, and diffuser section. The inlet and diffuser sections were connected at either ends of the bladed section. The bladed section and the shroud wall of the diffuser were defined by third order Bézier curves, the theory of which is discussed in Appendix E. All of the remaining endwall contours were defined by straight lines.

The inlet channel (see Figure 4.1) length at the hub wall equalled half the radius of the impeller outlet. The inlet height (*z*-coordinate) of the shroud wall of the channel was the same as that of the hub wall. The inlet angle of the channel at the hub and shroud was constrained to equal that of the corresponding endwall bladed angles. In other words, the inlet channel angle of the hub equalled that of the hub bladed section angle at point h_1. The same applied to the shroud angles. No other inlet wall shapes were investigated (Bézier, parabolic, etc.). It has been shown, however, that performance gains can be obtained by carefully designing inlet channels (Engeda et al., 2003).

The 2 Bézier curves defining the impeller endwalls each had 4 control points. Each of these control points had an *r* and *z* coordinate in the meridional plane. Point h_1 (see Figure 4.1) was set as the leading edge of the bladed hub endwall section. This point had a *z*-value equal to the height of the impeller, b_{imp} (measured from the impeller hub outlet), and an *r*-value equal to the impeller inlet radius, r_{1hub}. The corresponding point on the shroud contour, s_1, had the same *z*-value while the *r*-value was set to $r_{1shroud}$. Point h_2 on the hub contour was constrained with $r = r_2$ and $z = 0$. The corresponding shroud contour point, s_2, was constrained with $r = r_2$ and $z = b_2$ (hub-to-shroud height at tip). Point h_{B1} in Figure 4.1 was constrained with respect to point h_1 in that the angle between the two points defined the hub inlet angle in the meridional plane. The same applied to the corresponding shroud point. Finally, point h_{B2} on the hub contour was constrained with $z = 0$ and its *r*-coordinate given by

$$r = \frac{r_2 - r_{1hub}}{2} + r_{1hub} \tag{4.1}$$

For the shroud point, s_{B2}, $z = b_2$ and

$$r = \frac{r_2 - r_{1shroud}}{2} + r_{1shroud} \tag{4.2}$$

The inlet radius of the impeller at the hub section, r_{1hub}, was calculated using the radius ratio, equation (4.3), of an existing impeller (Schwitzer S200). The ratio of the Schwitzer hub inlet radius to the tip radius was:

$$\frac{r_{1hub}}{r_2} = 21.7\% \tag{4.3}$$

For the new design, a value of 8.138 mm was calculated for r_{1hub}.
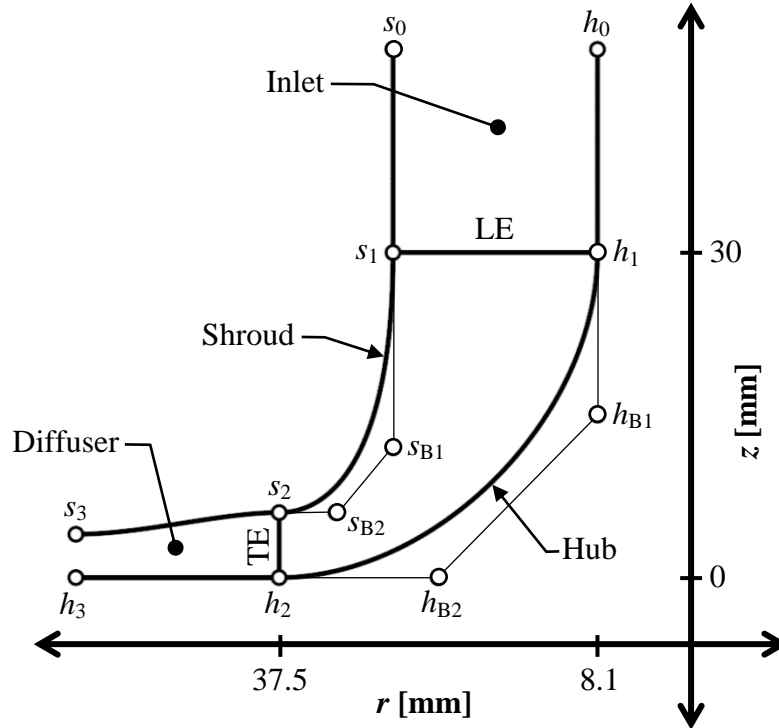
Figure 4.1: Meridional view of endwall contours and Bézier control points.

At the impeller outlet, a vaneless diffuser guided the flow to the outlet of the computational domain. The endwalls at the vaneless diffuser were modelled by a horizontal hub and a Bézier curved shroud. The radius of the diffuser outlet was calculated by:

$$r_3 = 1.5r_2 \tag{4.4}$$

The inlet height of the diffuser was equal to the outlet height of the impeller of 6 mm. The outlet of the diffuser was constrained at a height of 5 mm. The vaneless diffuser was added to the compressor geometry to perform the subsequent CFD screening.

4.3.2   Blades

The most complex geometric feature of a centrifugal compressor is its blades. There are a number of parameters that define an impeller blade. This number varies, depending on the complexity of the blade shape. In this project, each blade was defined first by its meridional hub and shroud contours. The next step was to

define the blade camber line at any point on the hub and shroud contour in the dm/r-θ plane. The blade camber lines were defined by the distribution of the angle, $\beta(u_m)$, between the blade camber line and the meridional plane (see Figure 4.2). The $\beta(u_m)$ distribution at the hub and shroud were defined by the following third order polynomial (Verstraete *et al.*, 2010):

$$\beta(u_m) = \beta_0(1 - u_m)^3 + 3\beta_1 u_m(1 - u_m)^2 + 3\beta_2 u_m{}^2(1 - u_m) + \beta_3 u_m{}^3 \tag{4.5}$$

with u_m being the nondimensionalised meridional length ($u_m \in [0,1]$, 0 at the leading edge, and 1 at the trailing edge). β_0 and β_3 represented angles at the leading and trailing edges of the blade. The camber line circumferential position, θ, was then defined by:

$$rd\theta = dm \tan\beta \tag{4.6}$$

where r equalled the radial coordinate of a point on the camber line and dm equalled the length of a finite camber line section in the meridional plane.
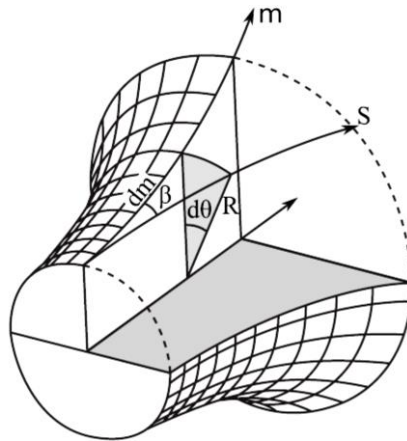
Figure 4.2: Definition of the blade camber line by β angle (Verstraete et al., 2010).

The main blade hub and shroud camber lines were both defined using equations (4.5) and (4.6). The splitter blades were created using the camber line information from the main blades. To define the splitter hub and shroud camber lines, those of the main blade were essentially cut off at a predefined length. The length of the splitter blade hub and shroud camber lines was set to equal a fraction, $f_{startsplit}$, of the respective main blade camber lines.

$$L_{CL_{split}} = L_{CL_{main}} \times f_{startsplit} \tag{4.7}$$

Both the hub and shroud camber lines used the same fractional value. Independent fractional values for the camber lines were also investigated. The camber line circumferential position, θ, of the splitter blades was defined by:

$$\theta_{split} = \theta_{main} - \frac{360}{2z_{main}} \tag{4.8}$$

where θ is given in degrees and z_{main}.equals the number of main blades on the impeller.

Once the blade camber lines were created, the blade thickness distribution was defined (see Figure 4.3) by following the procedure outlined by Verstraete et al. (2010). The blade thickness was distributed normal to the camber line as a function of the nondimensionalised camber length, u. The profile shape of the main and splitter blades at their leading edges was elliptical. The length of the leading edge, u_1, was a fraction of the hub or shroud blade camber length. Following the ellipse, the blade thickness remained constant up to a certain point u_2 on the camber line. After this point, the blade thickness distribution took on a parabolic shape until it reached the trailing edge.
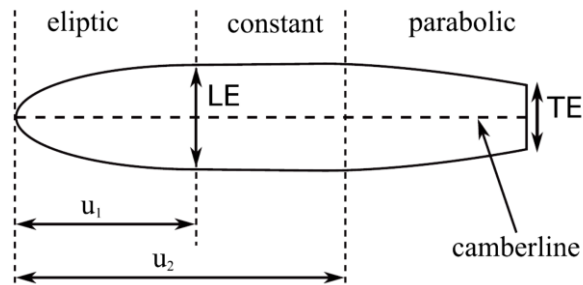
Figure 4.3: Thickness distribution normal to the camber line (not to scale) (Verstraete et al., 2010).

The thickness distribution of the blades for the mean-line design was set to equal that of the Schwitzer impeller mentioned in Section 4.3.1. The values for the different parameters are given in Table 4.1. All of the parameters were the same for both impellers, except for the trailing edge thickness, TE, which was calculated using the following correlation:

$$\frac{TE}{b_2} = 10\% \tag{4.9}$$

where b_2 equalled the trailing edge blade height. A trailing edge thickness of $TE = 0.6$ mm was calculated.

Table 4.1: Thickness distribution parameters (refer to Figure 4.3).

Parameter	Value
u_1	0.1
u_2	0.8
LE_{hub} [mm]	2
LE_{shroud} [mm]	0.6
TE [mm]	0.6

A blade lean angle could also be defined using the MATLAB code. The lean angle was measured at the blade trailing edge between the blade tip and the hub surface, as shown in Figure 4.4. A default angle of 90° was used. For blades created with a lean angle of less than 90°, the MATLAB code provided the option of extending the shroud trailing edge. In other words, increasing the radius variable r_{tip_shroud}. This is contrary to the convention of using the same tip diameter for the hub and shroud. The advantage of extending the shroud trailing edge is that it keeps the blade edge at the tip normal to the flow direction.
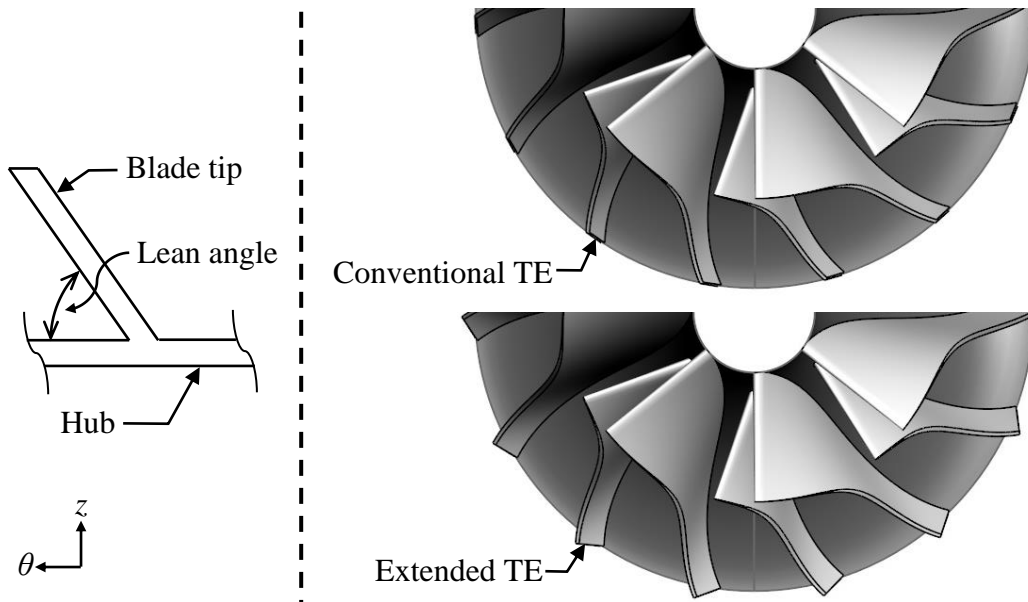
Figure 4.4: Blade tip showing lean angle as well as conventional and extended trailing edges.

The effect on performance of the blade lean and its extension was minimal according to the mean-line code. The only parameters that were affected were the blade meridional and camber lengths. CFD was therefore required to accurately model the effect of blade lean, the geometry of which could be added to a *geomTurbo* file by the MATLAB code.

The last parameter to be assigned a value was the gap, t, between the blades and the shroud (or clearance gap). The main consideration when assigning a tip gap

size is interference between the blade and shroud when the impeller is operating at full speed. A clearance gap value of 0.27 mm was obtained from the following relation (Zemp et al., 2010):

$$\frac{t}{b_2} = 4.5\% \tag{4.10}$$

4.4   Comparison of Designs

Using the MATLAB code discussed in Section 4.3, a wide range of impeller geometries was created. The performance of each impeller was then calculated using the mean-line code discussed in Section 3.6. Finally, the best performing impeller geometry was exported for further processing.

4.4.1   Design parameters

The parameters used to create the compressor geometry were referred to as the design parameters. These parameters included free, frozen, and dependent parameters. The free parameters are listed in Table 4.2, as well as the parameter value limits and the step size with which the values were incremented (a Discrete Interval Testing (or DIT) method was followed when assigning free parameters with values). All the remaining parameter values were either kept constant (frozen) or were dependent on other parameters values, as highlighted in Section 4.3.

The compressor endwalls had 1 free parameter, namely the shroud radius at the inlet. The upper bound of $r_{1shroud}$ was the result of the constraints mentioned in Section 4.2. The lower bound was not affected by these constraints. The value of the lower bound therefore needed only to be low enough to prevent the design value from being blocked at this bound (see Section 5.4).

There were 3 free parameters describing the impeller blades. These were the leading edge camber line angle at the hub and shroud, and the outlet angle at the blade tip. All other blade parameters were either frozen or dependent. They mostly influenced the blade curvature, which had little effect on the performance calculated by the mean-line code.

Table 4.2: Free parameters for mean-line performance calculation.

Parameter, p_n	Lower bound, $p_{n,l}$	Upper bound, $p_{n,u}$	Step size, $p_{n,step}$
$r_{1shroud}$ [mm]	25	27	0.1
β_{1hub} [degrees]	50	65	1
$\beta_{1shroud}$ [degrees]	20	35	1
β_2 [degrees]	60	90	1

A different geometry was created for each combination of free parameter values. The number of sample geometries created was a function of the number of free parameters and the number of steps for each parameter:

$$N_{sample} = \prod_{n=1}^{N_{free\ par}} \left(\frac{p_{n,u} - p_{n,l}}{p_{n,step}} + 1 \right) \tag{4.11}$$

The total number of sample geometries created was 166.7×10^3.

4.4.2   Impeller performance

The performance of each of the different geometries was calculated using the mean-line code. Two different values were calculated to define the impeller performance. First, the isentropic total-to-total efficiency was calculated at the impeller outlet. The other value that was calculated was the total-to-total pressure ratio, also at the impeller outlet. An objective function was used to weight the resulting pressure ratios and efficiencies for the different geometries. This allowed the performances to be compared using a single value:

$$P = \frac{\Pi_{t-t}}{5} + \frac{\eta_{t-t}}{0.798} \tag{4.12}$$

The weighting factors for the pressure ratio and efficiency were 5 and 79.8% respectively. These were the target values for the impeller performance. The factors were used to nondimensionalise the respective performance values. The objective function value for the target case would therefore be equal to 2. Any better/worse design would have an objective function value larger/smaller than 2.

Every time a new impeller was created, its performance was calculated. The impeller performance would then be compared with that of the "best" performing impeller from the samples already created. If the performance was better, the new sample would be saved as the "best" performing impeller. This was done until the performance of each of the 166.7×10^3 impeller geometries was calculated and compared. Once a new design was obtained, the step sizes of the parameter values describing the blade shape were reduced and the parameter value of $r_{1shroud}$ was frozen. The upper and lower bounds of the blade shape parameter values were also shifted to within one of the initial step sizes at either sides of the new parameter value:

$$\begin{aligned} p_{n,l} &= p_n - p_{n,step} \\ p_{n,u} &= p_n + p_{n,step} \end{aligned} \tag{4.13}$$

The number of new geometries analysed equalled 9.26×10^3.

The CPU time for the whole procedure was 2 hours 24 minutes on a 3.33 GHz Intel® Core™ i5 machine with 8 GB of RAM.

4.4.3   Best design

The best performing set of impeller parameters (after reducing the parameter step sizes and ranges) is shown in Table 4.3.

Table 4.3: Best performing impeller parameters according to mean-line code.

Parameter	Value
$r_{1shroud}$	26.1 mm
β_{1hub}	52°
$\beta_{1shroud}$	24.6°
β_2	60°

The compressor chart in Figure 4.6 was created using the same approach as highlighted in Section 3.6.1. This chart shows the impeller design point (green square) and performance over a range of mass flow rates and impeller speeds.

A surface model of the impeller was created using a script that was written for Rhinoceros3D. The script is added as Appendix F. The surface model can be seen in Figure 4.5. First, the hub surface was created by revolving the hub contour around the z-axis. The hub contour was plotted by fitting a curve through the point coordinates written by the MATLAB code. To create the blade surfaces (main and splitter), the blade pressure and suction side contours on the hub and shroud were first plotted. This was done by applying the same procedure as for the hub contour. A surface was then lofted from the hub to the shroud contour. Once the main and splitter blade surfaces were created, 6 more copies of each were arranged symmetrically around the vertical axis.
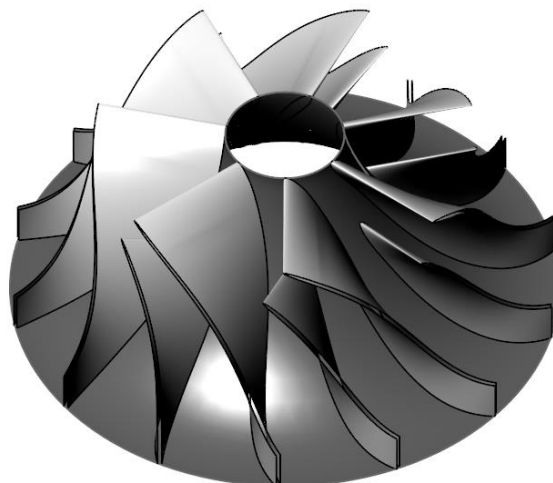
Figure 4.5: Surface model of best performance impeller (Rhinoceros3D®).

The geometry of the mean-line design was exported as a *geomTurbo* file to be read by NUMECA™ Autogrid5™. This was done to perform the CFD screening of the mean-line design.

4.5   CFD Screening

    1) Mesh generation

The mean-line design *geomTurbo* was read by NUMECA™ Autogrid5™ and the computational domain was meshed. Details on the mesh are given in Appendix G.

    2) Flow generation

The same boundary conditions used for the CFD simulation in Section 3.5.3 were applied to the screening of the mean-line design. The only difference was in the imposed mass flow rate, which was increased to 0.325 kg/s. The operating speed was also set to 121 krpm. The output values calculated by the CFD simulation were the same as in Section 3.5.5.

    3) Results

CFD results at the compressor design point in Figure 4.6 show good correlation with the mean-line code results. The total-to-total pressure ratio calculated by the CFD closely corresponded with the same property calculated by the mean-line code (4.17 vs. 4.14). The calculated total-to-total efficiencies differed more (91.6% vs. 89.7%) but the difference was still small.

The most obvious difference in results was the mass flow rates at which stall and choke occurred. The mean-line code predicted that stall would occur at a much higher relative mass flow rate. The single largest contributing factor to this prediction was the test for stall conditions mentioned in Section 3.6.1. In this test the calculated throat area plays a significant role. The algorithm used to calculate this area could be refined; however, any refinement would result in a much longer running time for the mean-line code. As the design point was never located on or near the stall point, the loss in accuracy was an acceptable trade-off considering the reduced computational time. Also, the stall criterion proposed by Aungier (2000) was only tested on larger centrifugal compressors with pressure ratios of less than 4.

According to the mean-line code, choke also occurred at a lower mass flow rate compared to the CFD results. Again the calculated throat area played a significant role. Another contributing factor was the fact that in the mean-line code, choke was a 1-dimensional occurrence. In reality, choked flow is 3-dimensional. CFD therefore played an important role in simulating the operation of the mean-line design under choked conditions.

After testing the mean-line design performance, work focused on the optimisation of the mean-line design. Prior to the optimisation, areas were identified where the

compressor performance had to be improved. One such area was the static pressure at the compressor outlet. The static pressure at the outlet is 280 kPa which equates to a total-to-static pressure ratio of 2.83. According to Dixon (1998), total-to-static pressure ratios of higher than 6 have been obtained with larger compressors. The small size of the compressor presented a problem. Also, increasing the impeller speed to obtain a higher pressure ratio was not an option, largely due to limits on mechanical stress in the material.
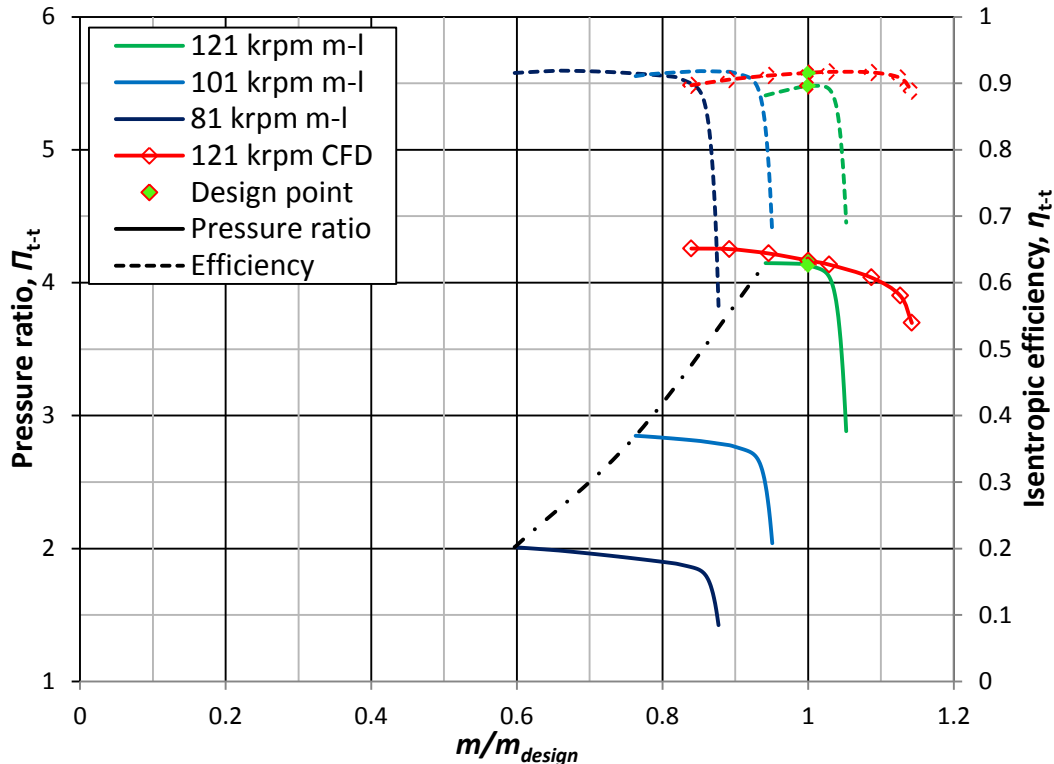
Figure 4.6: Performance curves of mean-line (m-l) design. All quantities calculated at impeller outlet. m_{design} = 0.325 kg/s.

An area where design refinement could lead to improved performance was the blade shape. The mean-line code did not entirely take into account the aerodynamic properties of the blade surfaces. This was one of the reasons for optimising the design using CFD and not the mean-line code. The geometry generated by the mean-line code served as a baseline from which to perform the CFD optimisation. Each set of mean-line overall blade parameters (hub and shroud inlet angles, outlet angle, etc.) could produce an infinite amount of blade shapes. The effects of blade shape include relative Mach number distribution, secondary flows, and friction losses. All these effects could be modelled using CFD.

5 OPTIMISED DESIGN

5.1 Introduction

The use of a mean-line code to predict impeller performance provided the geometry that served as a starting point for the optimisation process. This significantly decreased the number of parameters to consider during optimisation, as well as the ranges in which these parameters were allowed to vary.

5.2 Methodology of Design

The first step in the process to optimise the compressor impeller was to fit a parametric model to the mean-line design geometry. Once completed, the parameters that could be varied (free parameters) during optimisation had to be selected. A database of CFD simulations was then created to initialise an Artificial Neural Network (ANN). The database was generated using the Design of Experiments (DOE) approach. The ANN was used in conjunction with subsequent CFD analyses and a Genetic Algorithm (GA) to perform the optimisation.

5.3 Blade Fitting

NUMECA™ Autoblade™ produces high quality aerodynamic surfaces which are second order curvature continuous (Hildebrandt et al., 2008). These surfaces are defined by sets of parameters which are adjustable by the user. In this project, some of these parameters were identical to those defined in Section 4.3. However, most of the parameters were new and dependent on typology settings in NUMECA™ Autoblade™. It was therefore decided not to import the parameters of the mean-line design, but rather the geometry itself, in the form of a *geomTurbo* file. A parametric model was then fitted onto the mean-line design geometry. This model was defined by a new set of parameters.

The fitting process consisted of three steps which were independently configurable. The steps were the following:

1) Set target geometry
2) Initialise model
3) Optimise fit

5.3.1 Set target geometry

For the target geometry, the mean-line design *geomTurbo* was selected. Once selected, the various curves defined in the *geomTurbo* file were displayed in the NUMECA™ Autoblade™ design space (see Figure H.1). These curves included the hub, the shroud, and the sections of the 3-dimensional blades. The curves were displayed in the different coordinate systems typically used for the design of

turbomachinery components. These included the meridional and $dm/r\text{-}\theta$ planes. The parameters of the compressor were defined in these same coordinate systems.

5.3.2   Initialise model

An initial model was generated from a preliminary analysis of the target geometry. Some adjustments were made to the topology and parameters at this stage. NUMECA™ Autoblade™ has a database of default topology and parameter settings. Each entry is for a certain type of turbomachinery. The centrifugal compressor with splitter blade entry was selected.

When an optimisation based on the fitted model is planned, the key point is to use as few parameters as possible (between 50 and 100) and the simplest laws to define the curves. The number of sections used should also be between 2 and 5. Additional sections will increase the total number of parameters. This will result in the geometry fitting being a much more time consuming process. A range of values was estimated for each parameter by means of the *initialisation* process. The resulting parametric model is referred to as the initial model.

The *initialisation* process did not provide an exact replica of the target geometry. Some manual adjustment of the curve types and their parameters was necessary before the final step in the fitting process could be performed. This adjustment was made in 5 main categories:

1) Endwalls

The endwall contours were linear at the compressor inlet and replicated the geometry of the mean-line design. The bladed sections of the contours were described by Bézier curves. The outlet contours were straight at the hub and converging at the shroud. The converging part of the contour was created using a Bézier curve. The order of the curve types from inlet to outlet was therefore line-Bézier-line at the hub, and line-Bézier-Bézier at the shroud. The total number of parameters defining the endwalls was 28.

2) Stream surfaces

The settings in this category depend on the way sections were defined in the target *geomTurbo* file. Hub to shroud interpolated stream surfaces were used. Only 2 parameters defined the stream surface locations as a percentage of span in the hub-to-shroud direction.

3) Stacking laws

The blade shroud section was positioned (stacked) relative to the hub section using the blade section leading edges as reference. The number of parameters for this category totalled 7. It included details on the blade leading and trailing edges as well as the blade lean angle.

4) Main and splitter blade

The type of curve defining the blade camber lines in the *dm/r-θ* plane was set to a third order Bézier curve with 4 control points. The thickness distribution was defined by a side curve with an elliptical leading edge. 3 nodes described the side curve as an offset of the blade camber line. The splitter blades were created as shortened sections of the main blades. This category contained a total of 22 parameters.

5) Other

The total number of blades was the only parameter in this category. The number of main blades was held constant at 7, with an additional 7 splitter blades.

The total number of parameters for all the mentioned categories was 88 (see Appendix I for parameters and values). This large number of parameters is typical for centrifugal compressors (Hildebrandt et al., 2008).

5.3.3   Optimise fit

Once all the parameters and curve laws were manually adjusted to closely match the target geometry, the fitting process was started. The NUMECA™ Autoblade™ fitting process utilises an optimisation algorithm (GA). The algorithm is combined with an estimate of the error between the target geometry and the current model. To minimize this error criterion, the process is divided up into smaller, consecutive steps which consist of local optimisations involving only subgroups of the parameters defining the geometry.

The fitting process can be performed in either one of three modes, *Coarse*, *Medium*, and *Fine*. The settings of the three modes are the same, except for the number of iterations (25, 50, and 100 respectively). This means that a *Fine* process is twice as slow as a *Medium* process, which in turn is twice as slow as a *Coarse* process.

For all three fitting modes, the first two fitting steps optimise the meridional endwall curves as well as the tangential and meridional locations of the blade leading and trailing edge traces. The parameters defining the blade sections are then optimised.

In this project, the total time required to complete each step depended on the geometry involved in that specific step.

- The first step was skipped as the endwall contours were manually fitted onto the mean-line design geometry.
- The second step optimised the stacking laws. A sweep law was applied and each blade only had two sections. This meant that the step time was also short.
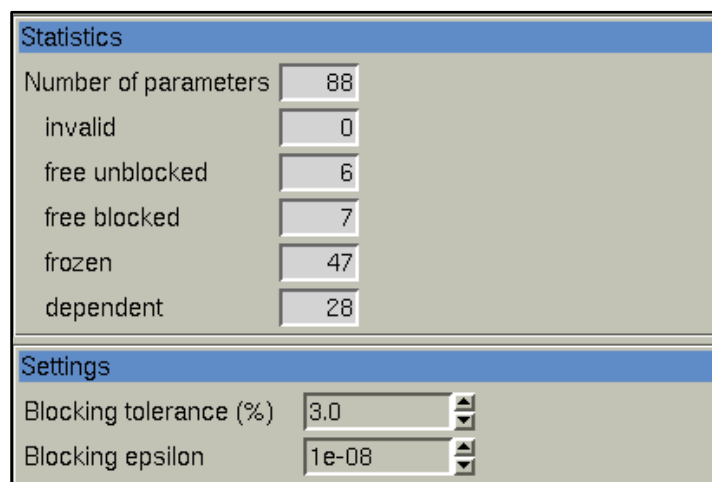
- The next steps involved the blade sections. The processing time for all the sections of a given blade was the same. The completion of this step was slower than the first two steps.

On average, the processing time was proportional to the number of blades. The total processing time was 4 minutes on the machine described in Section 4.4.2. The result of the fit optimisation was a complete and accurate parametric model of the mean-line design compressor.

5.4   DOE Database: Parametric model setup

The database generation was an important part of the design procedure because it used a significant proportion of the total computational resources available for the global optimisation process. Moreover, the physical and numerical conditions chosen to perform this database generation were very important because they remained constant throughout the whole design process.

Once the parametric model of the mean-line design was created, the free parameters that would be allowed to vary during the database generation and design optimisation were specified. Using too many free parameters would have extended the duration of the optimisation process. The dependencies of other parameters, and those parameters that were frozen, also had to be specified. Figure 5.1 shows the number of free, frozen, and dependent parameters.

Statistics	
Number of parameters	88
invalid	0
free unblocked	6
free blocked	7
frozen	47
dependent	28
Settings	
Blocking tolerance (%)	3.0
Blocking epsilon	1e-08

Figure 5.1: Numbers of parameters (NUMECA™ Autoblade™).

The compressor model was defined by 88 design parameters. A total of 13 parameters were allowed to vary within specified bounds. The values of 28 parameters were functions of other parameter values (see Appendix I). The remaining 47 parameters were assigned constant values during the fitting process. The *blocking tolerance* and *blocking epsilon* entries determined when free

parameters could be considered as blocked, in other words, when their values approached the upper or lower bounds.

The determination of the bounds for the free parameters in NUMECA™ Autoblade™ is a compromise between the following two rules:

- The range must be large in order to explore as wide a design space as possible during optimisation.
- The range must be limited, to some extent, in order to avoid unrealistic combinations of blade parameters.

These rules cater for the use of global mesh and flow generation settings. This allows for the automation of these processes and the generation of a DOE database which, except for its initialisation, does not require any user input.

Figure 5.2 shows the free parameters specified for the fitted model as well as their ranges. The current value of the parameter relative to its allowed range is shown by the bars to the right in the figure. The parameters themselves fall under different categories and can be seen, along with other parameters in the same categories, in Appendix I.

Name	Lower bound	Value	Upper bound	Scale
S1_CAMBER_H3	0.7	0.7	1	
S1_SPLIT1_MLE	0.33	0.428	0.53	
S2_SPLIT1_MLE	0.2	0.219	0.4	
Z_LE_HUB	27	30	33	
S1_MERID_LENGTH	0	2.82787601620	1000000000	
S2_MERID_LENGTH	0	1.01394305629	1000000000	
DELTA_1B	0	0.04	0.04	
THETA_SHROUD_OUT	0	0	20	
BETHA_HUB_OUT	0	10	10	
BETHA_HUB_IN	45	52	60	
BETHA_SHROUD_IN	24	24.6	30	
SHROUD_BEZIER_2	0	0.25	0.25	
SHROUD_R4_RATIO	0	0.55	1	

Figure 5.2: Free parameter values and bounds (NUMECA™ Autoblade™).

The degrees of freedom of the endwall free coordinates are shown in Figure 5.3. A considerable amount of time was spent on specifying the parameter ranges and dependencies to prevent the creation of unrealistic compressor geometries during the database generation. The degrees of freedom of each coordinate were constrained by the range of the parameters defining it. The movement of those coordinates that did not have degrees of freedom was constrained by the dependence on other parameters. It is important to note that the coordinates in Figure 5.3 are exactly that, they are not parameters. Their movement was merely constrained by parameters.
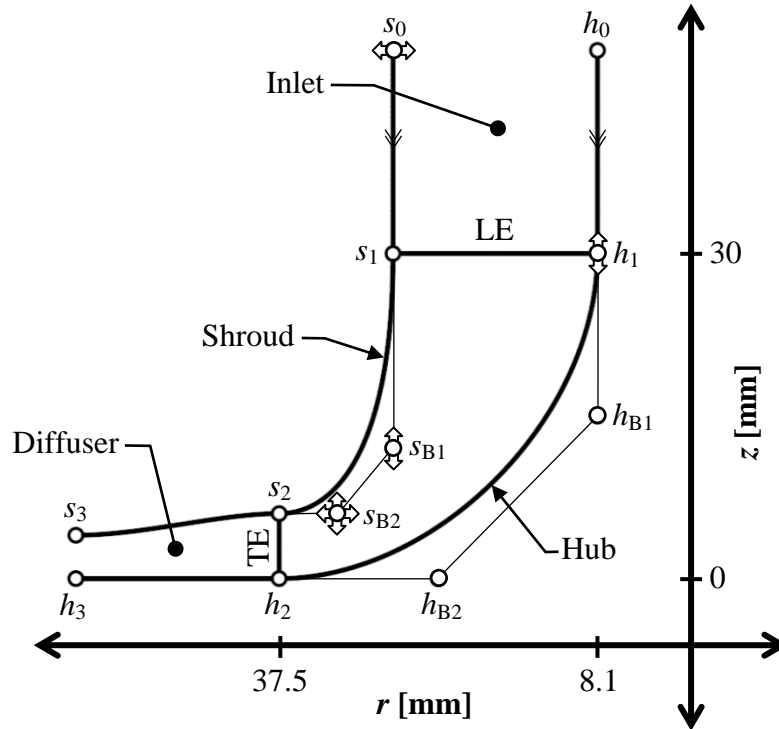
Figure 5.3: Meridional view of endwall contours with control points and degrees of freedom.

The first free coordinate, s_0, had a constant z-coordinate which was defined as the impeller height extended by a length equal to one half of the impeller tip radius. The r-coordinate was controlled by the free parameter, SHROUD_R1, in Figure 5.2 and had the range shown. This meant that the coordinate only had a degree of freedom in the r-direction. However, as the r-value of s_0 changed, this value was carried over onto all subsequent, dependent coordinates. This meant that s_1 and s_{B1} both had the same radial position as s_0.

The next free coordinate, h_1, was free to move in the z-direction and was dependent on the parameter Z_LE_HUB. This parameter defined the height of the impeller leading edge, which was modelled as being horizontal. This parameter also constrained the z-value of s_1 and, combined with the r-constraint in the previous paragraph, therefore fully constrained s_1.

Coordinate h_{B1} was the second control point of the Bézier curve defining the hub endwall. It was also dependent on Z_LE_HUB. The position of h_{B2} was constrained by the parameters HUB_R4 and HUB_Z4 (see Appendix I). Coordinate s_{B1} could also move in the z-direction and was dependent on the SHROUD_Z3 parameter (see Appendix I). This parameter, in turn, was a function of three other parameters, all three of which were allowed to vary during optimisation:

$$s_{B1_z} = SHROUD\_BEZIER\_2 \times s_{1_z} + s_{B2_z} \tag{5.1}$$

The SHROUD_BEZIER_2 parameter is shown in Figure 5.2 to have a value between 0 and 0.25. Equation (5.1) shows that the z-value of s_{B1} was anywhere in-between that of s_{B2} (SHROUD_Z4), and s_{B2} plus a quarter of the LE height. The coordinate s_{B2} was free to move in both the r- and z-direction. The coordinate parameters, SHROUD_R4 and SHROUD_Z4, were both dependent on other parameters:

$$s_{B2_r} = (35 - s_{0_r}) \times SHROUD\_R4\_RATIO + s_{0_r} \tag{5.2}$$

where 35 mm was the upper limit allowed for the radius component of control point s_{B2}.

$$s_{B2_z} = \tan(THETA\_SHROUD\_OUT(\frac{pi}{180}))\,(s_{2_r} - s_{B2_r}) + s_{2_z} \tag{5.3}$$

The main parameter influencing the axial position of s_{B2} was the outlet angle of the shroud contour, or Bézier curve. The parameter describing this angle is given in Figure 5.2 as THETA_SHROUD_OUT and was allowed a value between 0° and 20°, relative to the r-θ plane. The axial position of s_{B2} was based on the outlet angle of the shroud, and a varying radial position (SHROUD_R4). The axial position of s_{B2} (SHROUD_Z4) was then calculated with equation (5.3) which took into account the impeller tip radius and shroud outlet height.

The positions of s_2, h_2, s_3, and h_3 were fixed, their values prescribed by the overall impeller bounds given in Section 4.2. Three of the four control points of the Bézier curve (not shown in Figure 5.3) defining the diffuser shroud contour were also fixed. The final control point coordinates were calculated to ensure tangency between the bladed and diffuser shroud contour sections.

The camber lines were described by fourth order Bézier curves with five control points each. Each blade (main and splitter) was described by a hub and shroud camber line. Figure 5.4 shows how the control points of each Bézier curve were distributed. Each control point had a constant value in the dm/r-direction. The values were stretched along the dm/r-axis by means of geometric progression. This led to an asymmetrical distribution of the points, with more points located near the trailing edge of the camber line. For the free coordinates, only the θ-values were allowed to vary, with the value of the first (LE) coordinate (h_0, $s_0 = 0$) serving as a reference.
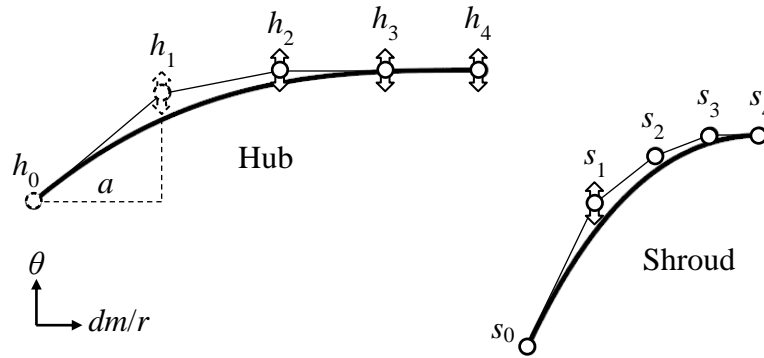
Figure 5.4: Blade camber lines and control points with degrees of freedom in θ-direction.

Now, for the hub camber line, four of the five control points were free to move in the θ-direction. The first coordinate, h_1, was described by the $S1\_CAMBER\_H1$ parameter. Its θ-value was calculated using the inlet blade angle and the meridional length of the hub camber line:

$$h_{1_\theta} = a \times \tan(BETHA_{HUB_{IN}}(\frac{pi}{180})) \tag{5.4}$$

where a was the first element length in the geometric progression, and was calculated by:

$$a = S1\_MERID\_LENGTH/(1 + r + r^2 + r^3) \tag{5.5}$$

with r being a common ratio, in this case 0.9. The value of BETHA_HUB_IN was allowed to vary from 45° to 60° (Figure 5.2), relative to the r-θ plane. Exactly the same procedure was applied to obtain the θ-coordinate of s_1. The only difference was that BETHA_HUB_IN and S1_MERID_LENGTH were replaced by BETHA_SHROUD_IN and S2_MERID_LENGTH respectively.

The only camber line control point directly influenced by a parameter was h_3, through the parameter S1_CAMBER_H3. All the remaining free control points were in some way dependent on this parameter, the first one of which was h_2. The θ-value of h_2 had an upper bound equal to the value of h_3. Relative to this value, it could vary with the value given by parameter DELTA_1B. The resulting θ-coordinate was either the same, or smaller than that of h_3. At the trailing edge, h_4 had a θ-coordinate calculated using the same approach as in equations (5.4) and (5.5). The parameter used at the trailing edge to describe the blade outlet angle was BETHA_HUB_OUT. The final three control points of the shroud camber line were constrained with values from the hub camber line control points. In Appendix I, the dependence correlations of the control point parameters are given. Constraining the shroud camber line using the hub coordinates ensured that no

unrealistic blade geometries were created and that less flow simulations did not converge during the database generation.

The last of the free parameters were S1_SPLI1_MLE and S2_SPLI1_MLE. These parameters defined the hub and shroud coordinates of the splitter blade leading edge, respectively. They were non-dimensional factors used to limit the extent of the main camber in the meridional plane. In other words, the splitter blade was a truncated section of the main blade.

5.5   DOE Database: Database generation

The DOE database samples were generated by perturbing the free parameters. The parameter values were chosen within the defined ranges. In NUMECA™ FINE™/Design3D, two options to generate a database were available: full random (*Continuous*), or discrete level (*Random among Discrete Levels*), which was used in this project. The options available under the *Random among Discrete Levels* setting were the *random number generator index*, the *number of discrete levels*, and the *number of samples* to generate. The *random number generator index* was the first value of a list of predefined random numbers. If more than one database was created using the same *random number generator index*, all resulting geometries and flow solutions would be identical. The *number of discrete levels* was the number of possible values for each NUMECA™ Autoblade™ free parameter. And finally, the total number of samples to be generated for the specific database was given by the *number of samples* field.

The procedure for creating the samples involved the following steps:

1) Geometry generation and export

The number of geometries that were generated determined the number of CFD analyses to be performed. A typical method for calculating the number of required geometries is by multiplying the number of free parameters by three (Hildebrandt et al., 2008).

$$N_{sample} = 3N_{par_{free}}$$
(5.6)

In the case of this project, the number of required geometries equated to about 50. For every one of the geometries, each free parameter could take on one of either two, or three values (*number of discrete levels*). These values were fixed at 0% and 100%, or 0%, 50%, and 100% of the maximum design range. Once all the parameters were assigned a value, the compressor geometry was exported as a *geomTurbo* file. The blade contours were exported as ruled surfaces to allow for flank milling during manufacturing (Hildebrandt et al., 2008).

2) Mesh generation

As mentioned earlier in the section, the database mesh and flow generation settings were global. That is, the same settings were used for all the samples of the DOE database. The settings used to generate the meshes were the same as those used in the mean-line design CFD screening (refer to Section 4.5). Details on the mesh are given in Appendix G.

3) Flow generation

As for the mesh generation, global settings were used to perform the CFD analyses. Again, the same settings used for the CFD screening were applied to the flow generation for the DOE database samples. CFD simulations were, however, only performed at the design mass flow rate of 0.325 kg/s.

4) Post processing

The values calculated from the CFD solution were used to provide the performance values of each database sample. The performance values were used as parameters for the optimisation objective function. These performance values included the mass flow rate, and the total-to-total isentropic efficiency and total-to-total pressure ratio at the diffuser outlet. Also included were the efficiency (total-to-total) and pressure ratio (total-to-total) at the impeller outlet. These two values were obtained by creating a cutting surface at the impeller outlet.

Each of the steps mentioned could be performed separately. For example, if new values had to be calculated they could be defined and the post processing step could be repeated using the data from the steps already completed. Or if flow generation settings needed to be adjusted, the geometry and meshes already created could be used. Of course, whenever the properties of a step were edited, all the following steps needed to be re-simulated to update the values calculated during post processing. The total computational time for every successful database sample was about 2 hours on the machine described in Section 4.4.2.

5.6   Optimisation

The optimised design process is given in Figure 5.5. The process is similar to that of the DOE database. The only difference is that the optimised design process has a closed loop, while the database generation process has an open loop. The closed loop is due to the fact that the model parameters at the top of the process (in Figure 5.5) are generated by the *Optimisation* step, whereas for the database generation process, these parameters are randomly generated. The *Optimisation* step is described in more detail in Appendix K.
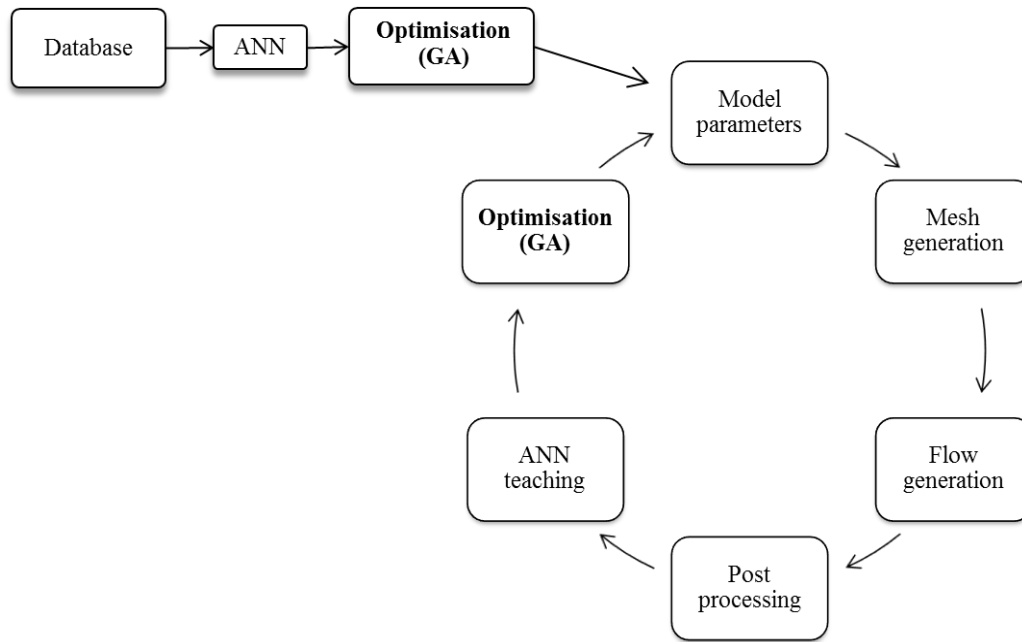
Figure 5.5: Design process.

Optimisation would be too costly a procedure if a CFD computation had to be performed for every possible combination of parameters. Therefore, the CFD results were predicted for specific combinations of parameters. This prediction was performed using an ANN (see Appendix J). The input of the ANN was the values of the free parameters. The ANN then predicted the same aerodynamic performance values that were created by the post-processing step. Once completed, a value would be predicted for the objective function. The accuracy of the ANN was measured by computing the error between the predicted objective function value, and the same value extracted from the training database (CFD calculations). The properties which governed the ANN were the learning parameters which are given in Table 5.1.

Table 5.1: ANN learning parameters.

Parameter	Value
Number of iterations	100000
Learning rate coefficient	0.5
Momentum coefficient	0.8
Decay factor	0.0
Convergence level criteria	0.1

The GA used to perform the optimisation is discussed in more detail in Appendix K. The number of reproduction cycles was set to *Fine* (100 cycles).

An objective function was used to measure the performance of the optimized solution. For each of the post-processed quantities in the objective function, a

penalty was computed. This penalty was higher the more the value differed from the desired (or imposed) value. By adding together these penalty terms, a value was obtained for the objective function. The purpose of the optimisation was to find the combination of design parameters that led to the lowest objective function value. The lowest value represented the compressor geometry which delivered the best performance, relative to the imposed values. The penalties were constructed using equation (5.7):

$$P = W \left(\frac{Q_{imp} - Q}{Q_{ref}} \right)^k \tag{5.7}$$

where Q_{imp} was equal to the imposed value, Q was the post-processed quantity value, and Q_{ref} was a reference value used to nondimensionalise the penalty term. The exponent of the penalty term was given by k. The weight factor, W, allowed for upward or downward scaling of the penalty term influence in the objective function. Two types of penalties were used:

- *Minimum Allowable Value* where the geometries having quantities which had a lower value than the one imposed were penalised.
- *Equality Value* where the geometries having quantities which were not the same as the one imposed, were penalised.

The objective function for the compressor design optimisation was constructed using the parameters given in Table 5.2.

Table 5.2: Objective function parameters. Performance properties calculated at diffuser outlet.

Performance property	Imposed value	Penalty weight
Isentropic efficiency (t-t)	0.798	2
Pressure ratio (t-t)	5	4
Mass flow rate [kg/s]	0.325	2

The number of optimisation cycles (Figure 5.5) to perform was set to 40. A graph of the objective function value convergence can be seen in Figure 5.6. Initially, the accuracy of the ANN prediction was low. After every *Post Processing* step in the following cycles, the ANN was trained and the optimal solution again obtained using the GA. The line showing the best value was updated at every cycle. A clear trend in the reduction of objective function error was observed, as shown by the figure. The objective function value calculated by the ANN and CFD converged after 35 cycles. Further convergence (more than 35 cycles) of the objective function value did not result in significant performance gains. The total computational time for each of the cycles was about 2 hours on the machine described in Section 4.4.2.
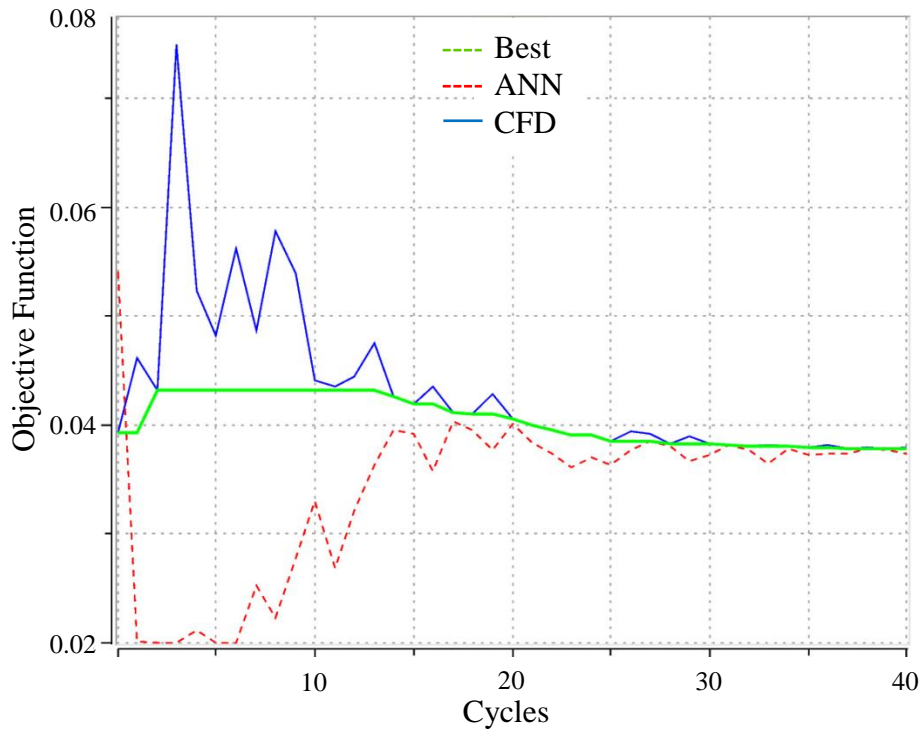
Figure 5.6: Optimisation convergence (NUMECA™ FINE™/Design3D).

A range of impeller geometries was optimised with different objective function performance properties, values, and weights. The pressure ratios and efficiencies at both the impeller and diffuser outlets were used for objective function terms. For all cases, satisfactory convergence of the results was obtained after 40 cycles.

5.7   FEA

The FEA performed on the compressor impeller was done using MSC SimXpert™ (MSC Software, 2011). The FEA did not form part of the optimisation process; it was done after the aerodynamically optimised design was obtained. The FEA served to assess the optimised design with regards to limits set on mechanical stresses during operation.

   1) Impeller CAD

A 3-dimensional solid model of the impeller first had to be created as the model used in the CFD was only a surface model. Therefore, certain features of the impeller had to be designed, in particular, the geometry below the impeller tip ($z < 0$). The initial solid model was created by intersecting the hub, shroud, cut-off, and blade surfaces using Rhinoceros3D. The solid model was subsequently modified to add other features of the impeller. A periodic section of the impeller, which included the main and splitter blade, was created as only one section

needed to be modelled using FEA (Verstraete *et al.*, 2010). The periodic section represented one seventh of the overall impeller geometry.

Once a CAD model of the main, periodic solid body was generated, the lower impeller geometry was designed. The main constraint on the design was the hoop stresses experienced during compressor operation. Earlier FEAs had shown that the maximum hoop stress occurred on the inside surface of the hole on the same *r-θ* plane as the impeller tip ($z \cong 0$). These hoop stresses were the result of the high rotational speed of the impeller and the relatively large tip radius and radial weight. As the geometry above the *r-θ* plane was constrained by aerodynamic effects, the section below it had to be designed so that it had as little radial weight as possible. The smaller radial weight would result in smaller hoop stresses. However, removing too much material, or removing it in the wrong areas, would lead to large deflections during operation resulting in contact between the impeller and shroud.

The last feature to be added to the CAD model was the blade fillets. A fillet size of 1.85 mm was selected as this was the same size found on the k27 benchmark impeller. Any larger fillets would not fit in-between opposing blade surfaces of the impeller due to its small size. The fillet radius was kept constant from the leading to the trailing edge.

2) Structural mesh

The mesh that was created for the periodic section of the compressor impeller needed to accurately model mechanical stresses during operation. The first step in the generation of the mesh was to specify which material the mesh elements would model. Two possible materials were identified in the literature survey for the manufacturing of the impeller. TI-6AL-4V is a titanium alloy with a very high mechanical and fatigue strength. Verstraete *et al.* (2010) designed a centrifugal compressor manufactured from this material. The price and availability of TI-6AL-4V is a concern however, and its use beyond the prototype stage cannot be vindicated. The other material was an aluminium alloy, AL 7075, most commonly known as *Ergal*. The primary alloying component of AL 7075 is zinc. Its mechanical strength is comparable to that of many steels and it depends greatly on the temper of the material. Its high strength-to-density ratio means that AL 7075 is often used in the aerospace industry. AL 7075 also has good fatigue strength. It was therefore decided to choose AL 7075 as the manufacturing material for the FEA of the optimised impeller. The material properties are shown in Table 5.3.

Table 5.3: AL 7075 material properties (ASM International, 1990).

Mechanical Property	Value
Ultimate tensile strength	572 MPa
Tensile yield strength	503 MPa
Fatigue strength	159 MPa
Shear strength	331 MPa

Modulus of Elasticity	71.7 GPa
Poisson's ratio	0.33

Quadratic tetrahedral elements were used to create the solid mesh of the impeller (Verstraete *et al.*, 2010). The number of elements that the mesh contained depended on how complex the geometry of the impeller was at high mechanical stress locations. For this reason, the mesh was refined around the blade fillet and near the shaft hole on the bottom surface. The leading edges of the main and splitter blades were also made up of small mesh elements to accurately model stresses and deformation during operation. The element sizes used to mesh specific geometric features can be seen in Table 5.4. A mesh dependency study was also performed, as seen in Section 5.9.

Table 5.4: Mesh element sizes of impeller features.

Feature	Element size [mm]
Leading edges	0.2
Blade fillets (near LE)	0.2
Blade fillets	0.5
Shaft hole	0.5
Periodic surfaces	0.8
Impeller body	2

The final mesh contained a total of 252,856 nodes and 172,561 elements.

   3)   Constraints and loads

All the constraints for the FEA were defined in the r,θ,z coordinate system. The periodic section of the impeller geometry was modelled using symmetry. The periodic surfaces were constrained in the θ-direction. The other constraint modelled the fixing method of the impeller. Impellers of this nature are typically shrunk fit onto shafts. During operation, the relatively large weight of the lower hub causes the shaft hole walls to deform radially. This in turn relieves the shrink fit causing the contact between the shaft and hub to become less rigid. For this reason, only the top third of the hole surface was modelled as being fully rigid.

Only one load was applied to the impeller, this load being the rotational speed of 121 krpm. It was initially planned to also add the aerodynamic loads to the FEA. However, after further investigation, it was found that these types of loads were typically used to study transient effects on the impeller structure such as fatigue (Dickmann et al., 2006). The scope of the project did not include a fatigue analysis; the effects of fatigue were however not ignored. The maximum allowable cyclic stress during operation was set to the fatigue limit of AL 7075.

The computational time for the FEA was 32 minutes on the machine described in Section 4.4.2.

5.8   Prototype and Testing

All the details on the manufacturing of the impeller prototype and the modification of the KKK k27 turbocharger can be found in Truter (2012). The impeller performance was measured using the test bench discussed in Section 3.7. The manufacturing and testing of the optimised impeller was not an objective for this project. However, time permitted the addition of the preliminary results at the end of Section 5.9 while work was being done, for a different project, to obtain final test results for the k27 compressor.

5.9   Results

1) Optimum parameters

The main parameter values for the mean-line and optimised designs are given in Table 5.5. For the endwalls, the shape of the hub contour remained constant except for the leading edge height being increased from 30 mm to about 33 mm. The shroud contour shape changed somewhat, due to the new outlet angle of 20°: the second and third control point parameters of the Bézier curve defining the shroud contour in Figure 5.3 were functions of the outlet angle (equations (5.1) to (5.3)). The vaneless diffuser shroud contour was also affected by the shroud outlet angle. This was due to the tangency constraint between the shroud walls of the impeller outlet and diffuser inlet.

Table 5.5: Main parameter values for mean-line and optimised designs ("~" if not optimised).

Parameter	Mean-line design	Optimised Design
Endwalls		
Impeller height [mm]	30	32.976
r_{1hub} [mm]	8.138	~
$r_{1shroud}$ [mm]	26.1	~
$\theta_{2shroud}$ [degrees]	0	20
Splitter hub LE [l_{split}/l_{main}]	0.275	0.53
Splitter shroud LE [l_{split}/l_{main}]	0.275	0.4
Blade shape		
β_{1hub} [degrees]	52	55.017
$\beta_{1shroud}$ [degrees]	24.6	24.488
β_2 [degrees]	60	90

The blade shape parameters shown in the table are at the leading and trailing edges of the blades. The other blade shape parameters were coordinates for the Bézier curves defining the camber lines. The hub and shroud contours of the mean-line and optimised designs can be seen in Figure 5.7. The inlet hub and shroud blade angles of the mean-line and optimised designs were almost the same, the largest difference of 2° being between the hub angles. The largest difference between the mean-line and optimised design blade shapes was the difference in

the outlet blade angle. The mean-line code calculated high pressure ratios when the impeller had a radial outlet. These high pressure ratios were however coupled with low efficiencies. This meant that the calculated value of equation (4.12) was lower than compared with those at lower outlet blade angles. The CFD however predicted that a relatively high efficiency could be obtained with a radial outlet, albeit at a much higher pressure ratio. This was primarily due to an optimum set of parameters defining the blade shape upstream of the impeller outlet.
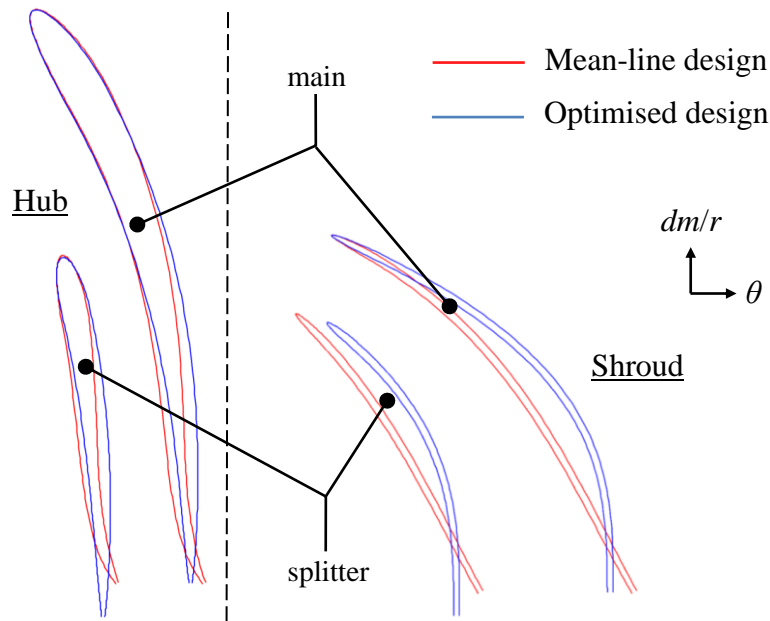
Figure 5.7: Hub and shroud sections of main and splitter blades (NUMECA™ Autoblade™).

The last optimised parameters were the leading edge locations of the splitter blade at the hub and shroud. The location of the splitter blade leading edge was strongly influenced by the relative Mach number at the impeller inlet. The design point mass flow rate had to be less than the choke mass flow rate. Therefore, the splitter blade could not be allowed to reduce the throat area of the impeller by being located in the impeller throat. As choked flow is highly three dimensional, it was expected that the optimised location of the splitter blade leading edge would differ from that of the mean-line design.

2) CFD results

The CFD results of the mean-line and optimised designs with regards to the obtained pressure ratios and efficiencies are shown in Figure 5.8. The most prominent difference between the designs was the pressure ratio obtained at 121 krpm.
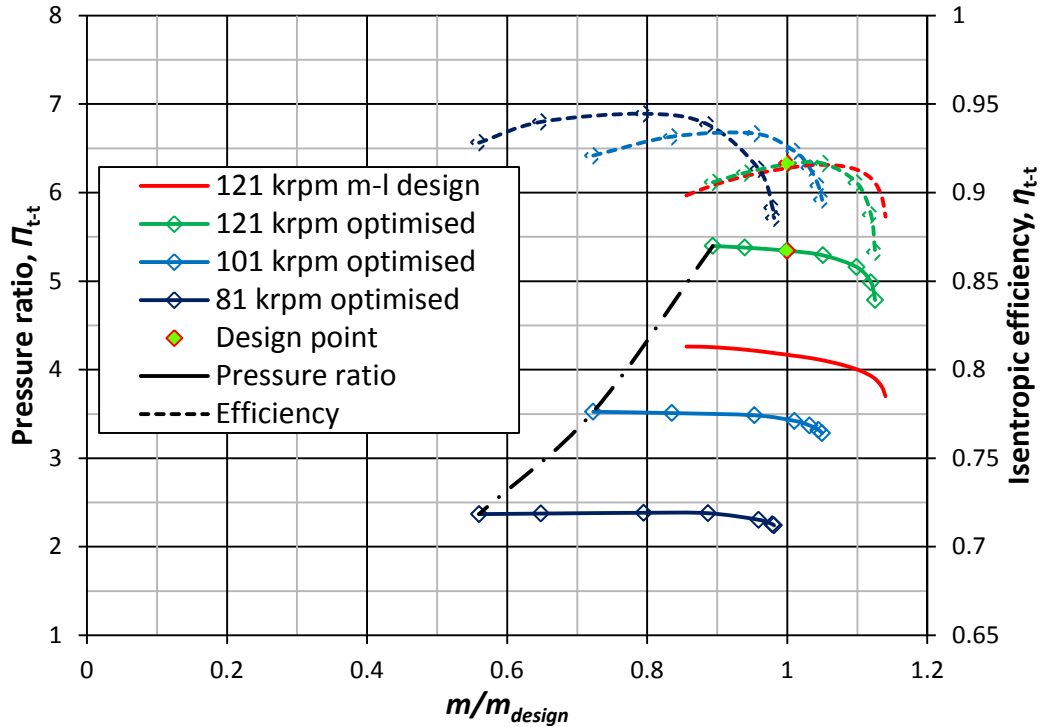
Figure 5.8: Performance curves of mean-line and optimised designs. All quantities calculated at impeller outlet. m_{design} = 0.325 kg/s.

The difference in pressure ratios was ascribed to the fact that the optimised design has a radial outlet, compared to the 60° backswept mean-line design. The efficiencies of the two designs were the same at 121 krpm. This was due to the optimised blade shape and shroud contour. The effectiveness of CFD optimisation becomes clear when it is considered that the main parameters for the two designs were very similar. The increase in performance was obtained by the optimisation of parameters that were interdependent. Their optimum values could not be obtained by existing rules or correlations.

One of the prominent features of both the mean-line and optimised designs was their surge margins. The surge margin, given by equation (5.8), is typically used to represent the stable operating range of a compressor (Tamaki *et al.,* 2009).

$$Surge\ margin = \frac{Q_s - Q_o}{Q_o} \tag{5.8}$$

where Q_s is the stall mass flow rate at the design point pressure ratio, and Q_o is the design point mass flow rate. The surge margin for the optimised design was calculated to be 10.9% at 121 krpm, which is excellent for radial bladed impellers and compared to compressors in literature with the same application (Boyce (2006) and Tamaki *et al.* (2009)).

The design point total-to-total pressure ratio at the outlet of the optimised impeller was 5.34. A pressure ratio of 5.7 was achieved when the objective function quantities were calculated at the impeller outlet (as opposed to diffuser outlet). The surge margin of the latter design was 6.7%, with the calculated efficiency being 91.1%. The difference in performance between the two designs was the result of different shroud outlet angles, $\theta_{2shroud}$ (Table 5.5). The design delivering the higher pressure ratio had a radial shroud outlet. The outlet angle for the design with the higher surge margin was 20°. This design was consequently selected for its superior surge margin and mass flow rate range.

The design point total-to-total efficiency at the outlet of the optimised impeller was 91.6%. Figure 5.8 shows the efficiency curve at 121 krpm reaching a maximum near the design mass flow rate. This property of the efficiency curve was one of the main goals of the optimisation and mean-line design. Even though the compressor efficiency was important, the pressure ratio was given a higher weight in the objective function. This meant that a higher pressure ratio could be obtained at the cost of overall efficiency.

The parameters having the largest effect on efficiency were those of the blade shape and the trailing edge blade height. The effect of trailing edge backsweep on efficiency is well documented. Although the trailing edge height was constrained at 6 mm, initial optimisation runs showed that lower trailing edge blade heights invariably resulted in higher compressor efficiencies. The trailing edge blade height also had little effect on mechanical stress during operation, as opposed to the leading edge height.

The fluid static conditions at the compressor outlet are given in Table 5.6 along with the same quantities for the k27 and S200 compressors mentioned in Sections 3 and 4.4.1. The values shown are those at the compressor MEPs at 121 krpm. The data for the k27 compressor was obtained from CFD results. The S200 performance values were read from a compressor chart (Borg Warner Turbo Sytems, 2011).

Table 5.6: Comparison of compressor performances at 121 krpm.

Parameter	r_2 [mm]	Mass flow rate [kg/s]	Efficiency (t-s)	Pressure ratio (t-s)
k27	40	0.277	0.746	3.3
S200	41	0.378	0.695	3.8
Optimised	37.5	0.336	0.748	3.25

The difference in outlet static pressure between the optimised and S200 impellers can be attributed to the difference in tip radii. Although the S200 does have blade backsweep at the tip, the larger radius results in the compressor achieving a higher pressure ratio. The same applied to the k27 impeller. The static pressure of the optimised design could have been increased by adding a vaned diffuser.

Regarding the total-to-static efficiency at the compressor outlet, the optimised impeller efficiency was, according to the CFD results, the best value of the three in Table 5.6. A further increase in efficiency would have resulted from implementing a blade backsweep and adding vanes to the diffuser. A reduction in the exit blade height would have resulted in even higher efficiencies, were it not fixed by the initial design constraints.

Another factor influencing the compressor efficiency was the relative Mach number distribution at the impeller inlet. The relative Mach numbers for compressors with high volume flow rates, delivering pressure ratios in excess of 3.5, are typically equal to or higher than 1 (Tamaki, 2012). High Mach numbers lead to shock formation which leads to a reduction in compressor efficiency. According to the CFD results, two shocks occurred for the k27 MEP at 90% span (Figure 5.9). "Shock 1" was a normal shock wave located downstream of the main blade leading edge, on the blade suction surface. This type of shock is the one typically found in compressors with a similar volume flow rate and pressure ratio. "Shock 2" occurred at the throat area between the main and splitter blades. It effectively choked flow in this channel. The occurrence of choke defeated the purpose of the splitter blade in the k27 impeller, which was to reduce metal blockage and delay choke. It was also the reason for the steep gradient of the 120 krpm performance curve (see Figure 3.12).

For the optimised impeller, the relative Mach number distribution in the meridional and blade-to-blade planes is shown in Figure 5.10. The blade-to-blade plane showed a normal shock upstream of the main blade leading edge. Flow subsequently decelerated downstream of the shock, only to accelerate again once past the suction side leading edge. The flow kept accelerating until it reached the position of maximum relative Mach number.

Flow in the optimised impeller throat was not choked at the design mass flow rate (there was only one shock and the flow between the main and splitter blade was not choked). This was primarily because, contrary to the k27 impeller, the leading edge of the optimised impeller splitter blade was not located in the impeller throat. Also, the blade thickness of the optimised impeller at the shroud was less than that of the k27 impeller (0.6 mm vs. 0.817 mm), reducing metal blockage in the throat area and allowing for a higher choke mass flow rate. The mass flow rate range of the impeller was thereby improved and the gradient of the performance curve reduced, resulting in more equal pressure ratios at varying mass flow rates and constant speeds.
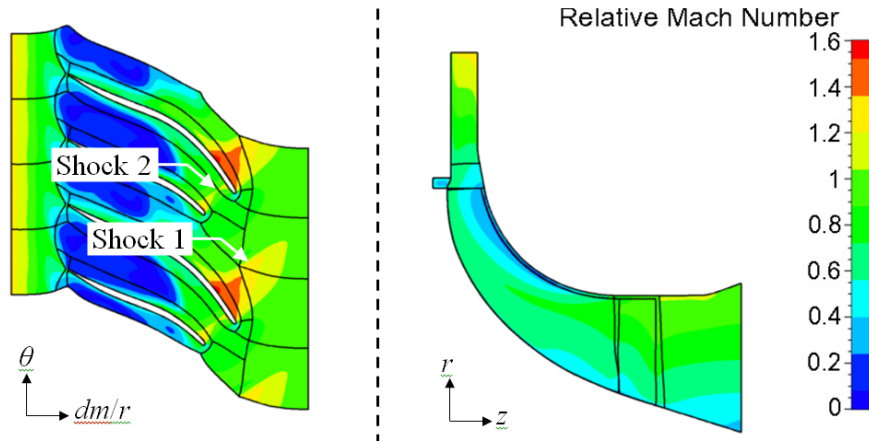
Figure 5.9: K27 contours of relative Mach number at MEP (120 krpm). Blade-to-blade plane at 90% span. Azimuthal averaged values in meridional plane (NUMECA™ CFView).

In the meridional plane, the highest relative Mach number was located near the main blade leading edge at the shroud, as seen in Figure 5.9 and Figure 5.10. In the blade-to-blade planes, the low relative Mach numbers located downstream of about 50% main blade meridional length were due to reverse flow in the clearance gap. The meridional relative Mach number distribution for the optimised impeller in Figure 5.10 shows low relative Mach numbers near the shroud at the same location as for the k27 impeller. The reverse flow was still prevalent for the optimised impeller even though the clearance gap was significantly smaller than that of the k27 impeller (27 mm vs. 45 mm). The relative Mach number for the optimised impeller at the shroud leading edge was also higher (as compared to the k27 impeller) since it had a larger shroud inlet radius (26.1 mm vs. 25.5 mm). The large shroud inlet radius of the optimised impeller was to allow for the relatively large, 0.325 kg/s design mass flow rate (the k27 impeller had an MEP mass flow rate of 0.277 kg/s).
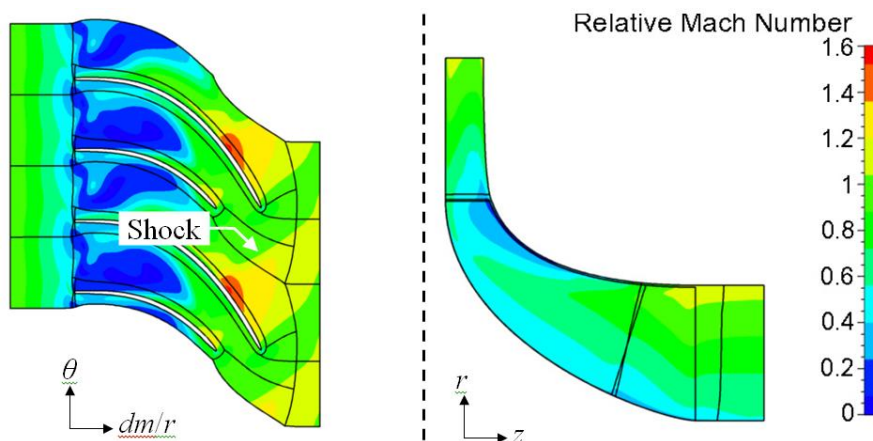
Figure 5.10: Optimised compressor contours of relative Mach number at design point (121 krpm). Blade-to-blade plane at 90% span. Azimuthal averaged values in meridional plane (NUMECA™ CFView).

3) FEA results

The mechanical stress experienced by the impeller was calculated for three different structural meshes (three mesh densities) to rule out mesh dependency when any results were analysed. The results of the mesh dependency study are shown in Table 5.7. These results show a good agreement between the maximum von Mises stress experienced by the impeller for all three meshes.

Table 5.7: Mesh dependency.

Mesh property	Coarse	Medium	Fine
Number of nodes	51,857	150,487	252,856
Number of elements	33,078	100,452	172,561
Max. von Mises stress [MPa]	380.6	381.3	381.4

According to the FEA results, the maximum mechanical stress experienced during compressor operation was the hoop stress at the inside surface of the shaft hole and had a value of 382 MPa. Much work was done in order to reduce the stress at this location. The initial design had a maximum stress in the same location of 480 MPa. The stress was reduced in subsequent designs by introducing undercuts to reduce radial weight. The maximum deflection resulting at the impeller tip was, however, too much and would have caused interference between the impeller and the shroud surface. The undercut was therefore removed in favour of a parabolic, converging taper starting at the bottom surface of the impeller, proceeding toward the impeller tip. This design resulted in a maximum von Mises stress that was well below the tensile yield stress of AL 7075. The load was also non-reversing. The preload provided by the impeller shrink fit on the shaft would further prevent fatigue.

The only other high stress concentrations occurred at the blade leading edges (see Figure 5.11), more specifically, at their roots. It is interesting to note that, between the two blades, the maximum stress of 260 MPa occurred at the leading edge root of the smaller, splitter blade. This was because the splitter blade leading edge did not protrude at a normal angle from the hub surface, as compared to the main blade. This effectively caused the moment load around the blade root to be higher than that of the main blade. Also, the relatively longer main blade was better supported by its own curvature.
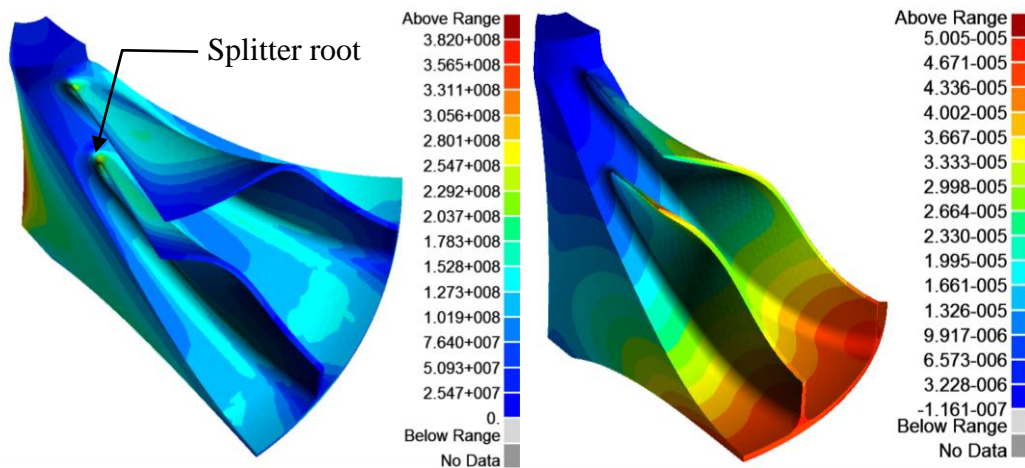
Figure 5.11: Impeller von Mises stress [Pa] (left) and radial deformation [m] (right) (MSC SimXpert™).

An initial design with a maximum von Mises stress of 400 MPa showed that the blade thickness distribution from hub to shroud strongly influenced the von Mises stress. According to Hildebrandt *et al.* (2008), blade thickness has a larger effect on mechanical stress than blade curvature. The initial design was modified by decreasing the shroud, and increasing the hub blade thickness. The hub blade thickness had little impact on compressor efficiency, as shown by Verstraete *et al.* (2010). The inlet blade height ($r_{1shroud} - r_{1hub}$) also played a significant role in the stress incurred at the hub root. A small blade height resulted in lower von Mises stresses. It should be noted that the load experienced at the leading edge roots was non-reversing.

Another mechanical property that was considered was the deformation experienced by the impeller blades. As mentioned in Section 4.4.3, the clearance gap between blade and shroud was 0.27 mm. This meant that the maximum allowable deformation of the blade tips was equal to, or lower than this value. Depending on the location along the meridional shroud coordinate, this deformation was allowed in either the radial (at the leading edge) or axial (at the trailing edge) direction. Figure 5.11 shows that the maximum radial deformation experienced was 0.05 mm, which at any point was small enough not to be of concern. The maximum axial deformation was located on the hub between the blades and had a value of 0.08 mm, also less than the allowable value.

The fact that the yield stress of AL 7075 was never exceeded meant that there was a possibility for the impeller to operate at higher speeds. No speeds higher than 121 krpm were modelled with FEA or CFD. Operation at any higher speed did not form part of the design objective, and therefore will not be optimal. Also, a multi-physics approach was not used during optimisation. In other words, the FEA results did not form part of the optimisation objective function. The optimal shape of the impeller hub, in particular, was not obtained taking into account the allowed mechanical stress.

4) Experimental results

The CNC milled, optimised impeller is shown in Figure 5.12. The impeller was tested using a modified KKK k27 turbocharger, as mentioned in Section 5.8. The compressor was tested at choke conditions, at the upper limit of the mass low rate range, and near surge at the lower limit. The compressor was not tested at surge as the effects of surge on the test bench had not been studied. The testing speeds were 81 and 101 krpm. The atmospheric conditions during testing differed from those of the CFD simulations, hence the corrected mass flow parameter for the horizontal axis of the chart in Figure 5.13.

Figure 5.12: CNC milled impeller. Ruler units in cm.

The CFD and experimental performance curves of total-to-static pressure ratio, just downstream of the compressor impeller, are shown in Figure 5.13. A noticeable trend in the experimental results, at both impeller speeds, is the similar mass flow rates at which choke occurred. It is very likely the absolute flow that was choked, as the choke mass flow rate did not increase with increasing speed, as required by equation (1.18) for relative flow choke. According to CFD results, the application of which was verified in Section 3.8, choke did not occur in the compressor inlet, blade passages, or vaneless diffuser at the mass flow rate indicated by the experimental performance curve. What is certain is that choke did not occur in the impeller, the design of which was the objective of this project.

The k27 shroud/volute that was modified to allow the optimised impeller to be fitted to the turbocharger for testing purposes, was initially designed to direct an absolute velocity flow with smaller tangential and radial components. The characteristics of the flow inside the volute are not known as the volute was not added to the CFD computational domain. Calculations showed that choke did not occur at the volute outlet at the design mass flow rate of 0.325 kg/s. What occurred at the interface between the diffuser and volute was, however, unknown and is therefore a topic for further study.
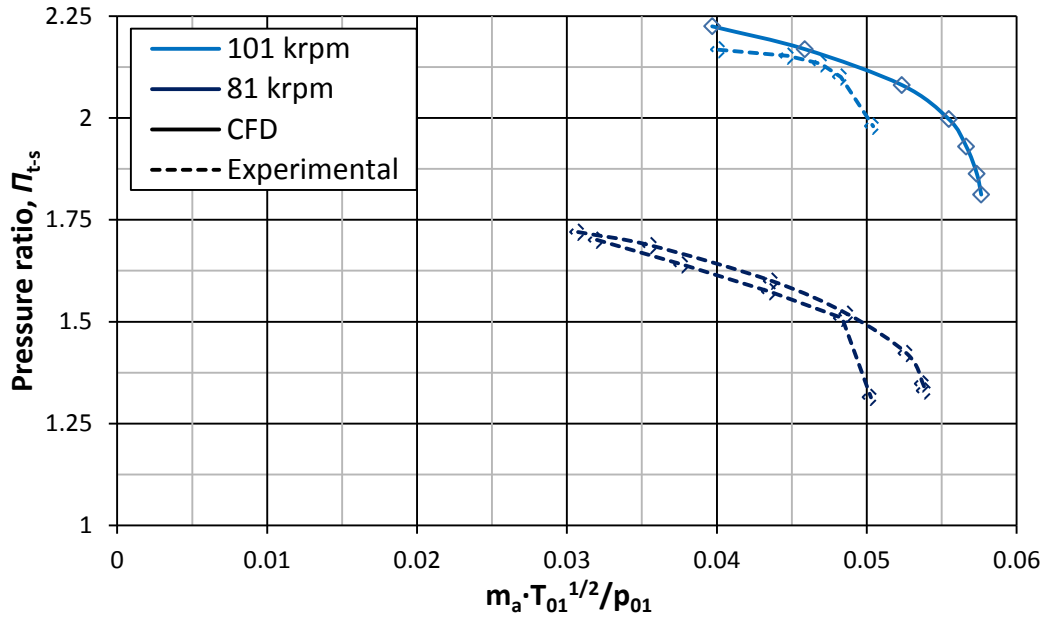
Figure 5.13: Optimised impeller experimental and CFD results, $R = 1.24r_2$.

The CFD and experimental results for the unchoked region were in good agreement. The gradients of the 81 krpm performance curves compared better than those of 101 krpm. The same trend was identified and discussed in the benchmark CFD and experimental results comparison in Section 3.8. The maximum difference in results in the unchoked region of the performance curves, at 101 krpm, was 2.5%. This can be ascribed to the omission of the blade fillets from the CFD simulations.

6 CONCLUSION AND RECOMMENDATIONS

The objective of this project was to design an MGT centrifugal compressor with certain performance properties and characteristics. The objective was reached by completing the work indicated in this section. A methodology was developed by which to design similar centrifugal compressors in future projects. The MATLAB code was created keeping in mind different user requirements with regards to performance properties and dimensional constraints. The dependent parameters of the DOE sample geometries were also set up such that future designs can use the same dependencies.

6.1 Benchmark Study

The results discussed in Section 3.8 allowed the mean-line code to be used to create a new impeller design. The performance calculated for this design was verified using CFD. There was also good agreement between the experimental and CFD results. CFD could therefore be used to verify the mean-line impeller design performance and to obtain an aerodynamically optimised, final impeller design.

6.2 New Design

A new centrifugal compressor impeller was designed using a mean-line code. The in-house code was modified to calculate compressor performance over a range of mass flow rates and impeller speeds. A new code to generate compressor geometry from user defined parameters was created and incorporated into the mean-line performance calculation code. Different parameters were tested and the best performing geometry, at the specified design point, was exported to perform a CFD screening. Good correlation was obtained between the mean-line and CFD design point performance data. The operational mass flow rate range was underestimated by the mean-line code, compared to CFD. This was attributed to the stall criteria used in the mean-line code as well as to the rough calculation of the impeller throat area, A_{th}.

A refinement of the blade shape was proposed in order to increase the performance of the compressor. One performance property that had to be improved was the static pressure at the diffuser outlet.

6.3 Design Optimisation

Optimisation of an ANN based on CFD calculations was selected as the tool by which to attain performance gains at the compressor design point. A GA was used to perform the optimisation. The initial CFD database used to train the ANN

contained a total of 50 samples. Each sample had the same boundary conditions, but a different geometry. The geometry was created from a parametric blade model that was fitted onto the new design geometry of Section 4. A total of 13 parameters were allowed to vary while the CFD database was created.

The final optimisation was performed over a total of 40 cycles (see Figure 5.6) with the objective function containing pressure ratio, efficiency, and mass flow rate terms. A design point total-to-total pressure ratio of 5.34 and total-to-total efficiency of 91.6% was obtained at the impeller outlet. It was found that the blade shape significantly influenced both the aerodynamic and mechanical performance of the impeller. The blade shape depended on a large number of parameters and design optimisation was necessary to find the optimum combination of these parameters.

The objective of the project was to obtain a total-to-total pressure ratio of 4.72 at an efficiency of 79.8% (t-t). These values had to be obtained at the diffuser outlet, at a design point mass flow rate of 0.325 kg/s and a speed of 121 krpm. The final performance results of the optimised compressor, as calculated by CFD, are shown in Table 6.1.

Table 6.1: Performance of optimised (final) design according to CFD. All quantities calculated at diffuser outlet.

Performance quantity	Objective	Optimised design
Pressure ratio (t-t)	4.72	4.79
Efficiency (t-t)	79.8%	79.1%
Mass flow rate [kg/s]	0.325	0.325

A comparative study between experimental and CFD results vindicated the use of CFD to calculate compressor performance during the design optimisation. Experimental results of the final, optimised design showed that the impeller did indeed perform as predicted, at the speeds and mass flow rates tested. The results gave an indication of the interdependence of the different components of a centrifugal compressor, and the need for a design methodology that includes all these components.

6.4   Future Work

The following areas have the potential for further work:

1) Experimental

A larger compressor volute can be designed, or an existing one modified, to ensure that choke never occurs downstream of the impeller. Once this has been done, together with the test bench safety audit (Nigrini, 2012), the impeller test speed can be increased to the design speed of 121 krpm.

2) Mean-line

The current criteria for predicting stall in the mean-line code can be replaced by the criteria in Schiffmann and Favrat (2010). A less coarse calculation of the throat area is not suggested as the increase in computational time to find a new design cannot be justified: the accuracy of the mean-line code at the design point is satisfactory.

The MATLAB code for testing compressor performances was created so that compressors with different defining parameters could be easily analysed. In this project, the method used to obtain a "best" design was DIT. For this approach, the total CPU time required to obtain a new design was strongly influenced by the number of free parameters (see equation (6.1)). Another shortcoming of DIT was the fact that only discrete parameter values could be tested.

$$t_{CPU,T} = t_{CPU,sample} \prod_{n=1}^{N_{free\,par}} \left(\frac{p_{n,u} - p_{n,l}}{p_{n,step}} + 1 \right) \qquad (6.1)$$

Due to the limitations mentioned in the previous paragraph, some work has been done to apply optimisation techniques to obtain a compressor design using the mean-line code. A GA function (see Appendix K), which uses the same mean-line performance calculation code applied to the DIT, has been programmed using MATLAB. The CPU time required to obtain a new design, with 4 free parameters, has been significantly decreased from 2 hours 24 minutes to 2 minutes. The new code also allows for an increase in the number of free parameters, the values of which are now continuous. Finally, multipoint optimisation functionality has been included in the design software. Optimisation can now be applied at different mass flow rates, to obtain a specific surge margin.

3) Compressor geometry

The largest improvement in performance can be obtained if a vaned diffuser were to be designed and used, instead of a vaneless diffuser. The use of a vaned diffuser will increase the static pressure at the compressor outlet, albeit at a slight drop in total-to-total pressure ratio. A vaned diffuser will require that the impeller be designed with backsweep at the outlet in order to reduce incidence and avoid choke at the diffuser inlet. The addition of impeller backsweep is also likely to improve the compressor surge margin and efficiency (Shibata et al., 2012). A reduction in the overall size of the compressor may also result, due to the relatively smaller outlet diameter of a vaned diffuser.

4) Design optimisation

A multidisciplinary approach to optimisation can be used where, along with the CFD, an FEA is performed at each optimisation step (Verstraete et al., 2010). The FEA results can then form part of the objective function. This can reduce the overall mass of the impeller and further increase the aerodynamic performance.

5) Centrifugal compressor design tool

The methodology that was developed to design a compressor can now be refined and extended. The final goal would be to have a fully integrated design tool which performs all the steps in the methodology automatically, only requiring the user to input design specifications and geometric constraints. The tool would obtain the best design according to mean-line code. The design would then be automatically exported and optimised using CFD and FEA.

Finally, the mean-line design code can be used as a standalone package. Empirical functions to predict mechanical stresses can be added to the code for a multidisciplinary design approach. The code can be expanded by including the functionality to design other components of a centrifugal compressor (inlet guide vanes, recirculation devices, and diffusers). The performance prediction will not be as accurate as that of CFD or FEA, however, the time and resources saved by using this in-house design tool might prove significant.

6.5   Work Duration

The duration of the project main work packages is shown by Table 6.2.

Table 6.2: Approximate time per work package.

	Engineering Time[2] [d]	CPU Time[3] [d/core]
Benchmark Study		
Surface CAD model	42	~
GeomTurbo	42	~
Mesh	21	~
CFD calculations	21	15
Mean-line setup	15	~
Mean-line calculation	~	0.5
New Design		
Mean-line modification	42	~
Mean-line design	~	1
CFD screening	5	0.5
Design Optimisation		
Geometry parameterisation	21	~
Robustness study of mesh	5	0.5
DOE database generation	21	10
Optimisation	42	20

---

[2] 8-hour, working day.

[3] 24-hour day.

LIST OF REFERENCES

ANSYS Inc., 2011. ANSYS CFX [WWW Document]. URL http://www.ansys.com/Products/Simulation+Technology/Fluid+Dynamics/ANSYS+CFX

ASM International, 1990. Metals handbook Vol.2 - Properties and Selection: Nonferrous Alloys and Special-Purpose Materials, 10th ed. ASM International, Metals Park, Ohio.

Adewuya, A.A., 1996. New methods in genetic search with real-valued chromosomes. *Master's thesis*. Massachusetts Institute of Technology, Cambridge.

Aghaei, R., Tousi, A.M., 2007. Design and CFD analysis of centrifugal compressor for a microgasturbine. Aircraft Engineering and Aerospace Technology 2, 137– 143.

Aungier, R.H., 2000. Centrifugal compressors. ASME Press, New York.

Benini, E., 2003. Optimal Navier-Stokes design of compressor impellers using evolutionary computation. International Journal of Computational Fluid Dynamics 17, 357–369.

Benini, E., Giacometti, S., 2007. Design, manufacturing and operation of a small turbojet-engine for research purposes. Applied Energy 84, 1102–1116.

Borg Warner Turbo Sytems, 2011. Performance Turbocharger Catalog [WWW Document]. URL http://www.turbodriven.com/files/pdf

Boyce, M., 2006. Gas turbine engineering handbook, 3rd ed. Elsevier, Houston.

Brasz, J., 1988. Investigation into the effect of tip clearance on centrifugal compressor performance, in: ASME, Gas Turbine and Aeroengine Congress and Exposition. Amsterdam, pp. 190–201.

Bézier, P.E., 1968. How Renault uses numerical control for car body design and tooling, in: Society of Automotive Engineers Congress. SAE International, Detroit.

Bézier, P.E., 1970. Emploi des machines à commande numérique, 1st ed. Masson, Paris.

Bézier, P.E., 1971. Example of an existing system in the motor industry: The unisurf system. Proceedings of the Royal Society of London. Series A, Mathematical and Physical Sciences 321, 207–218.

Casey, M.V., 1985. The effects of Reynolds number on the efficiency of centrifugal compressor stages. Journal of Engineering for Gas Turbines and Power 107, 541–548.

Casey, M.V., Fesich, T.M., 2010. The Efficiency of Turbocharger Compressors With Diabatic Flows. Journal of Engineering for Gas Turbines and Power 132, 072302.

De Wet, A.L., 2011. Performance investigation of a turbocharger compressor. *Master's thesis*. Department of Mechanical and Mechatronic Engineering. Stellenbosch University.

De Wet, A.L., Von Backström, T.W., Van Der Spuy, S.J., 2010. The CFD simulation of a centrifugal compressor, in: Seventh South African Conference on Computational and Applied Mechanics. Pretoria.

Delcam, 2011. PowerSHAPE [WWW Document]. URL http://www.powershape.com/

Demeulenaere, A., Ligout, A., Hirsch, C., 2004. Application of multipoint optimization to the design of turbomachinery blades, in: ASME Turbo Expo. ASME, Vienna, pp. 1481–1490.

Dickmann, H.-P., Secall Wimmel, T., Szwedowicz, J., Filsinger, D., Roduner, C.H., 2006. Unsteady flow in a turbocharger centrifugal compressor: Three-dimensional Computational Fluid Dynamics simulation and numerical and experimental analysis of impeller blade vibration. Journal of Turbomachinery 128, 455–465.

Dixon, S.L., 1998. Fluid Mechanics, Thermodynamics of Turbomachinery, 4th ed. Oxford.

Eckardt, D., 1974. Instantaneous measurements in the jet-wake discharge flow of a centrifugal compressor impeller, in: ASME Gas Turbine Conference and Products Show. Zurich, pp. 337–346.

Engeda, A., Kim, Y., Aungier, R., Direnzi, G., 2003. The inlet flow structure of a centrifugal compressor stage and its influence on the compressor performance. Journal of fluids engineering 125, 779–785.

Epstein, A., 2004. Millimeter-scale, micro-electro-mechanical systems gas turbine engines. Journal of Engineering for Gas Turbines and Power 126, 205–225.

Esterhuizen, I., September 2011. SA holds significant UAV production potential. Engineering News. Pretoria.

Forrest, A.R., 1972. Interactive interpolation and approximation by Bézier polynomials. The Computer Journal 15, 71–79.

Gong, Y., Sirakov, B., Epstein, A., Tan, C., 2004. Aerothermodynamics of micro-turbomachinery, in: ASME Turbo Expo. ASME, Vienna, pp. 95–102.

Government Communication and Information System, 2011. Unmanned air vehicle to make maiden flight in 2012.

Haupt, R., Haupt, S., 2004. Practical genetic algorithms, 2nd ed. John Wiley & Sons, Inc, Hoboken, New Jersey.

Hildebrandt, T., Fh, D., Thiel, P., Lehmann, I., 2008. Entwicklung eines leistungsgesteigerten Radialverdichters für Ab- gasturbolader : Von der CFD basierten Optimierung mit FINE ^{TM} / Turbo bis zum serienreifen Prototyp im Hause KBB Einleitung.

Hottinger Baldwin Messtechnik, 2011a. PD1 Differential Pressure Transducer [WWW Document]. URL http://www.hbm.com/se/menu/produkter/givare-sensorer/tryckgivare-foer-tryckmaetning/pd1/

Hottinger Baldwin Messtechnik, 2011b. P8AP Absolute Pressure Transducer [WWW Document]. URL http://www.hbm.com/se/menu/produkter/givare-sensorer/tryckgivare-foer-tryckmaetning/p8ap/

Ibaraki, S., Matsuo, T., Kuma, H., Sumida, K., Suita, T., 2003. Aerodynamics of a transonic centrifugal compressor impeller. Journal of Turbomachinery 125, 346–351.

Isomura, K., Murayama, M., Kawakubo, T., 2001. Feasibility study of a gas turbine at micro scale, in: ASME Turbo Expo. New Orleans.

Jabiru, 2011. Jabiru Aircraft and Engines [WWW Document]. URL http://www.jabiru.net.au/

Jansen, W., 1967. A method for calculating the flow in a centrifugal compressor impeller when entropy gradients are present, in: Royal Society Conference on Internal Aerodynamics (turbomachinery). pp. 133–146.

Japikse, D., Baines, N.C., 1994. Introduction to Turbomachinery. Oxford University Press, New York.

Kiney, J., 2009. The Market for Missile / Drone / UAV Engines, A special focused market segment analysis. Newtown, Connecticut.

Krige, D., 2012. Performance evaluation of a micro gas turbine centrifugal compressor diffuser. *Master's thesis*. Department of Mechanical and Mechatronic Engineering. Stellenbosch University.

Kurzke, J., 2009. GasTurb [WWW Document]. URL http://www.gasturb.de/index.html

Leyland, G., 2002. Multi-objective optimisation applied to industrial energy problems. *Master's thesis*. Ecole Polytechnique Federale de Lausanne.

MSC Software, 2011. MSC SimXpert [WWW Document]. URL http://www.mscsoftware.com/Products/CAE-Tools/simxpert.aspx

Michalewicz, Z., 1994. Genetic Algorithms + Data Structures = Evolution Programs. Springer-verlag Berlin, New York.

Mohseni, A., Goldhahn, E., Van den Braembussche, R. a., Seume, J.R., 2012. Novel IGV Designs for Centrifugal Compressors and Their Interaction With the Impeller. Journal of Turbomachinery 134, 021006.

Molyneaux, A., 2002. A practical evolutionary method for multi-objective optimization of complex energy systems. *Master's thesis*. Ecole Polytechnique Federale de Lausanne.

Musgrave, D.S., 1980. The prediction of design and off-design efficiency for centrifugal compressor impellers, in: ASME 22nd Fluids Engineering Conference. New Orleans.

Nigrini, V., 2012. Safety and performance assessment of a small scale compressor test bench. *Final year project*. Department of Mechanical and Mechatronic Engineering. Stellenbosch University.

Numeca International, 2011a. Numeca International [WWW Document]. URL http://www.numeca.be/

Numeca International, 2011b. NUMECA CFD [WWW Document]. URL http://www.numeca.be/

Numeca International, 2011c. User Manual for Autogrid5™ v8.

Numeca International, 2011d. User Manual for Fine/Turbo v8.

Numeca International, 2011e. User Manual for Design 3D.

OPTEK Technology Inc., 2011. OPB732 Reflective Switch [WWW Document]. URL http://www.optekinc.com/datasheets/OPB732.PDF

Pampreen, R.C., 1973. Small turbomachinery compressor and fan aerodynamics. Journal of Engineering for Power 95, 251–261.

Pichlmeier, D., 2010. Impressum [WWW Document]. URL http://www.dapi-tech.de/EN/projects_en.html

Robert McNeel & Associates, 2011. Rhinoceros, NURBS modelling for Windows [WWW Document]. URL http://www.rhino3d.com/

Rogers, D., 2001. An introduction to NURBS: with historical perspective, First. ed. Morgan Kaufmann Publishers, New York.

Schiffmann, J., Favrat, D., 2010. Design, experimental investigation and multi-objective optimization of a small-scale radial compressor for heat pump applications. Energy 35, 436–450.

Senoo, Y., 1987. Deterioration of compressor performance due to tip clearance of centrifugal impellers. Journal of Turbomachinery 109, 55–61.

Shibata, T., Yagi, M., Nishida, H., Kobayashi, H., Tanaka, M., 2012. Effect of impeller blade loading on compressor stage performance. Journal of Turbomachinery 134.

Simpson, A., Schmitz, M.B., Evangelisti, S., Belardini, E., Ballarini, V., 2012. Design and Testing of Multistage Centrifugal Compressors With Small Diffusion Ratios. Journal of Turbomachinery 134, 1–8.

Sirakov, B.T., 2005. Characterization and design of a non-adiabatic micro-compressor impeller and preliminary design of self-sustained micro engine system. *Master's thesis*. Massachusetts Institute of Technology.

Struwig, D., 2012. Design and construction of a test bench for micro turbomachinery. *Master's thesis*. Department of Mechanical and Mechatronic Engineering. Stellenbosch University.

Tamaki, H., 2012. Effect of recirculation device with counter swirl vane on performance of high pressure ratio centrifugal compressor. Journal of Turbomachinery 134, 051036.

Tamaki, H., Unno, M., Kawakubo, T., Hirata, Y., 2009. Aerodynamic design to increase pressure ratio of centrifugal compressors for turbochargers, in: Proceedings of the ASME Turbo Expo 2009: Power for Land, Sea and Air. ASME, Orlando, Florida, pp. 1171–1184.

Tamaki, H., Yamaguchi, S., 2007. The experimental study of matching between centrifugal compressor impellers and vaneless diffuser for turbochargers, in: ASME, Gas Turbine and Aeroengine Congress. Montreal, pp. 134–138.

Truter, N., 2012. Manufacturing and testing of a centrifugal compressor. *Final year project*. Department of Mechanical and Mechatronic Engineering. Stellenbosch University.

Van den Braembussche, R., 2005. Micro Gas Turbines–A Short Survey of Design Problems. Notes.

Verstraete, T., Alsalihi, Z., Van den Braembussche, R.A., 2010. Multidisciplinary optimization of a radial compressor for microgas turbine applications. Journal of Turbomachinery 132.

Vick, M.J., Heyes, A., Pullen, K., 2009. Design overview of a three-kilowatt recuperated ceramic turboshaft engine, in: Power for Land, Sea and Air. Orlando, pp. 1–14.

Warwick, G., 2010. More Fuel-Cell UAVs Fly. Aviation Week.

Wright, A.H., 1991. Genetic algorithms for real parameter optimization. Foundations of genetic algorithms 1, 205–218.

Zangeneh, M., Goto, A., Harada, H., 1998. On the design criteria for suppression of secondary flows in centrifugal and mixed flow impellers. Journal of turbomachinery 120, 723–735.

Zemp, A., Kammerer, A., Abhari, R.S., 2010. Unsteady computational fluid dynamics investigation on inlet distortion in a centrifugal compressor. Journal of Turbomachinery 132, 031015.

Ziegler, K.U., Gallus, H.E., Niehuis, R., 2003. Experimentelle Untersuchung der Laufrad-Diffuser-Interaktion in einem Radialverdichter variabler Geometrie.

APPENDIX A: IMPELLER CAD

The k27 impeller CAD was created from the point cloud data, discussed in Section 3.2.2. PowerSHAPE®, a software package used in the reverse engineering industry, provided the tools for fitting surfaces and curves to point cloud data.

Problems with collecting point cloud data were experienced from the onset, using a CMM. The small size of the impeller made it difficult to obtain accurate measurements. Because the impeller features were so small, relative to the scanning sensor, the sensor had to be re-orientated several times. This was done to allow access to all areas of the impeller while avoiding contact between other parts of the CMM and the impeller. The sensor longitudinal axis also had to be as normal to the measured surface as possible. The constant re-orientation of the probe caused the resulting point cloud data to have some inaccuracies. Problem areas included the leading edge profiles of the main and splitter blades as well as the shape of the blade profiles (see Figure A.1).
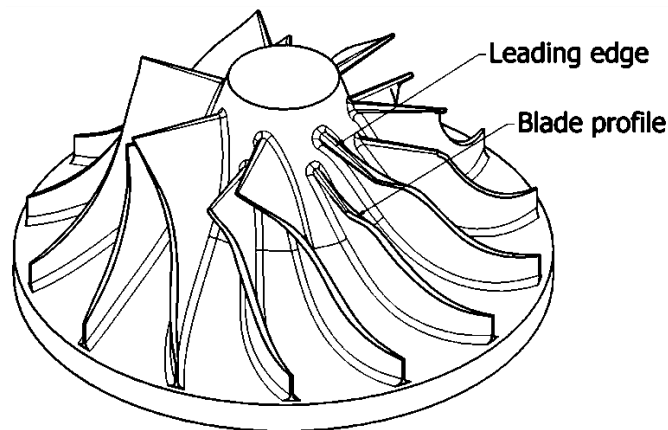
Figure A.1: Impeller CAD model from CMM data (Autodesk Inventor 2010).

Although it may appear to be an appropriate model, closer inspection of the CAD model in Figure A.1 reveals small inaccuracies which could have had a large effect on CFD results. The leading edges of the blades had to be created with circular profiles. Comparison with the actual blade profiles, which were more elliptical in shape, confirmed that more accurate point cloud data was required.

Another problem was the shape of the blade profiles. Directly behind the leading edge of the blades, the CMM data profile takes on a concave shape on the suction side of the main and splitter blades. Likewise, the same profile takes on a convex shape on the pressure side of the blade at the same relative position. This contradicts the actual impeller blade profiles seen in Figure 3.1. This, combined with the erroneous leading edge profiles, meant that a better method of scanning the impeller had to be found. There were however some measurements that could

87

be used, in particular, those of the shroud contour. Their use was justified by the fact that the sensor did not have to be re-orientated during scanning.

Three surfaces were created for each of the impeller blades (main and splitter), each surface containing its own information on the blade shape. These surfaces were the:

- Pressure side surface
- Suction side surface
- Leading edge surface

The surfaces were defined by selecting point coordinates near the edges of the point cloud models. These points formed the boundaries of the surface. Once all the boundaries were specified, a surface was created. This surface was tangent to all the scanned points lying inside the predefined boundaries. The precise boundaries, or edges, of the blade surfaces were not easily definable from the point cloud data. This is a common problem as all scanners, mechanical and optical, have a certain tolerance in accuracy when data is gathered. This tolerance in accuracy becomes a problem when sharp edges need to be scanned. In this project, the problem was circumvented by defining fitted surface edges close to, but not on, these edges. An example of this approach is shown in Figure A.2. Note the inaccurate, rounded representation of the point cloud edge.
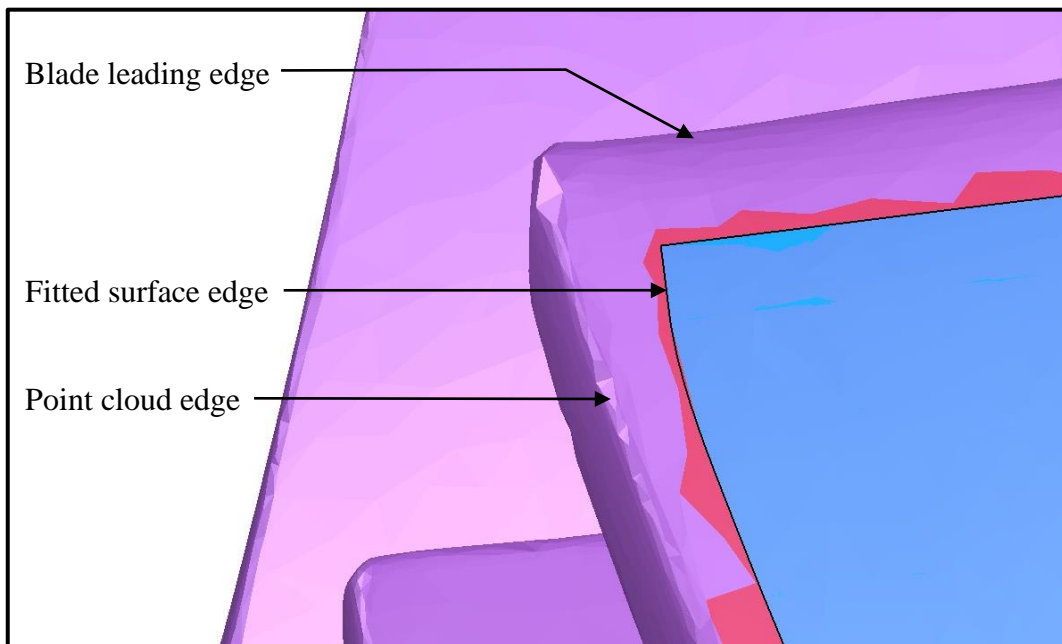
Figure A.2: Example of fitted surface edge location near rounded point cloud edge (PowerSHAPE®).

The need to define the surface boundaries manually was the reason for creating the three separate surfaces listed in the second paragraph. About 20 point

coordinates needed to be selected to define the boundaries of each surface. This process was time consuming since there were many irregularities in the point cloud data.

The surface creation process was complicated further by the presence of blade fillets and clearance gaps. The fillets are located at the blade/hub intersections. Their purpose is to reduce stress concentration during normal compressor operation and to allow the impellers to be milled. The clearance gaps are the gaps between the blades and shroud which allow relative movement when the impeller is rotating. Blade fillets and clearance gaps are treated as mesh parameters by NUMECA™ Autogrid5™ and are added after the *geomTurbo* file has been imported (see Section 3.4). Therefore, the fillets and tip gaps had to be omitted from the surface CAD model. This was done by defining the boundaries of the surfaces near the tip of the blades and origin of the fillets. Once the surfaces were created, they were extended on the fillet side to create virtual, unfilleted blade surfaces. This was also done with the shroud side surface edge to extend it to the shroud.

The six blade surfaces (combining the main and splitter blades) and a hub contour curve were exported in *step* file format from PowerSHAPE® to Rhinoceros3D® to do the final post processing.

The contour curves defining the hub (GOM™ scan data) and shroud (CMM data) were revolved around the z-axis to create the hub and shroud surfaces. The actual impeller hub ends along with the blade trailing edges. The rest of the geometry (opposite the shroud, in the diffuser section) forms a different component of the compressor assembly. This section is called the lower diffuser. In large centrifugal compressors, the meridional hub contour can be modelled as being tangent to the lower diffuser section. This was not the case for the k27 compressor as the difference in height between the hub outlet and lower diffuser inlet was significant. This difference in height was 11.5% of the impeller outlet hub-to-shroud height. The implications of this are explored in Section 3.8. For the time being, a tangent condition at the hub and lower diffuser interface was assumed.

Once each set of blade surfaces were imported from PowerSHAPE® to Rhinoceros3D®, they were trimmed and merged into single surfaces: one for each blade, main and splitter. The surfaces were merged with tangent conditions at their relative interfaces, the interfaces being pressure side-to-leading edge and leading edge-to-suction side. After they were merged, the surface edges were extended so that they intersected the hub and shroud surfaces respectively, on either side. The trailing edges of the blade surfaces were also extended, to be trimmed at a later stage.

As highlighted in Section 3.2.1, a *geomTurbo* file defines the blade surfaces as spanwise section contours of the blade. In order to create these contours, concentric hub-to-shroud surfaces had to be evenly distributed into the space

between the actual hub and shroud. It was decided to distribute four surfaces in order to capture all the necessary blade information. Quasi-normal lines were located at 7 instances along the meridional endwall contours. These lines were then divided into 5 equal length segments. A total of 4, 3rd degree polynomial curves were created, their control points being the endpoints of the equal-length segments. Finally, the curves were revolved around the z-axis creating the concentric hub-to-shroud surfaces. The final surface to be created was located at the trailing edge of the impeller. This surface was cylindrical in the *z*-direction and used to define the trailing edge of the blade surfaces.

In order to create the contours required by the *geomTurbo* file, all the intersections between all of the surfaces were used to create 12 blade contour curves. The next step was to convert the remaining curves into points. This was done by dividing the blade contour curves into 500 segments each, the ends of these segments providing the point coordinates. The number of segments used depended on the number necessary to capture all the information on the leading edges of the blades. The endwall curves were also divided into the same number of segments.

All the point coordinates mentioned in the previous paragraph were exported under their respective headings as text files. A total of 14 text files, consisting of 12 blade sections and 2 endwalls, were exported. MATLAB code was used to arrange the point coordinates into the correct groups and to write a *geomTurbo* file.

APPENDIX B: MEAN-LINE ANALYSIS

The mean-line code was compiled from the work of Aungier (2000). The compressor impeller was modelled at different sections, namely the inlet, throat, and outlet. First, the inlet velocity triangle and air density were iteratively computed at standard atmospheric conditions. The same was done at the throat of the impeller, using the properties calculated at the inlet as initial values. Finally, the air properties at the impeller outlet and the useful and parasitic work required to compress the air was calculated. All the internal loss coefficients were added and the loss in total pressure calculated iteratively. Finally, the compressor impeller pressure ratio and efficiency was calculated.

The impeller blade passages correspond to a rotating duct. The compressor operation is characterised as having a required work input (to compress the working fluid), and being subjected to internal losses. The internal losses are characterised by their effect on the pressure at the impeller outlet as well as the increase in entropy of the system. The loss models used are briefly mentioned below. For a more detailed discussion the reader should refer to De Wet (2011).

The first of the internal losses is the **incidence loss** which accounts for flow adjustment from the actual flow angle to the blade angle. A loss coefficient, $\overline{\omega}_{inc}$, was calculated using the following equation:

$$\overline{\omega}_{inc} = 0.8\left[1 - \frac{C_{m1}}{W_1 \sin\beta_1}\right]^2 + \left[\frac{z_{main}t_{b1}}{2\pi r_1 \sin\beta_1}\right]^2 \tag{B.1}$$

The loss coefficient was calculated at the hub, shroud, and mean stream surfaces, with the overall incidence loss coefficient being defined as a weighted average of these values.

An entrance **diffusion loss**, $\overline{\omega}_{DIF}$, was computed for cases where the diffusion of flow between the leading edge and the throat was found to be more significant than the adjustment of flow at the leading edge due to incidence.

$$\overline{\omega}_{DIF} = 0.8\left[1 - \frac{W_{th}}{W_1}\right]^2 - \overline{\omega}_{inc} \tag{B.2}$$

where $\overline{\omega}_{DIF} \geq 0$ was required.

The **choke loss** was computed to account for losses when the throat Mach number approached unity. Due to the one-dimensional nature of the mean-line theory, choke in the impeller throat occurs suddenly. This means that the impeller pressure ratio and efficiency drop sharply over a small range of mass flow rates, the extent of which is directly proportional to the choke loss coefficient. In turn,

the dependence of the choke loss coefficient on the throat area, A_{th}, means that the throat area needs to be accurately calculated. The choke loss coefficient is given by

$$
\begin{aligned}
\overline{\omega}_{CH} &= 0 & X \leq 0 \\
\overline{\omega}_{CH} &= \frac{1}{2}(0.05X + X^7) & X > 0 \\
X &= 11 - 10C_r \frac{A_{th}}{A^*}
\end{aligned}
$$
(B.3)

with the aerodynamic blockage in the impeller being modelled by a contraction ratio correlation C_r. The area for which a specified mass flow rate will yield a sonic velocity is denoted by A^*. A method by which to calculate A_{th} is given by Aungier. The most complicated step in this method is computing the blade-to-blade throat width, h_t, in a stream surface. Conformal transformation is used to map the *m-theta* plane into a Cartesian plane, *x-y*. In Aungier (2000), the conformal transformation is defined by

$$
\begin{aligned}
X &= \int_{m1}^{m} \frac{dm}{r} \\
Y &= \theta
\end{aligned}
$$
(B.4)

Angles are preserved in a conformal transformation, therefore

$$
\frac{\partial Y}{\partial X} = \frac{r \partial \theta}{\partial m} = constant
$$
(B.5)

and

$$
h_{th} = \int_{m1}^{m} \sqrt{1 + \left(\frac{r \partial \theta}{\partial m}\right)^2} \, dm \approx \sqrt{1 + \left(\frac{\Delta \theta}{X}\right)^2} \, \Delta m
$$
(B.6)

Equation (B.6) is used to calculate distances from all points on the suction side of one blade to a fixed point on the pressure side of the opposing blade. The shortest distance on any particular stream surface is then selected as the throat distance for that surface. The throat area between any two stream surfaces is computed by

$$
A_{th} = \overline{h}_{th} \ \overline{\cos \epsilon \Delta n}
$$
(B.7)

where $\overline{h}_{th}$ is the average throat distance between the two stream surfaces. The distance between the stream surfaces is given by n with $\overline{\cos \epsilon \Delta n}$ accounting for the fact that the stream surfaces may not be normal to the throat area.

The coefficient resulting from **skin friction loss** is given by

$$\overline{\omega}_{SF} = 4c_f \left(\frac{\overline{W}}{W_1}\right)^2 \frac{L_B}{d_H} \tag{B.8}$$

where $\overline{W}$ is the average relative velocity in the impeller. The **blade loading loss** is given by

$$\overline{\omega}_{BL} = \left(\frac{\Delta W}{W_1}\right)^2 / 24 \tag{B.9}$$

while the **hub-to-shroud loading loss** is given by

$$\overline{\omega}_{HS} = \frac{1}{6}\left(\frac{\overline{\kappa}_m \overline{bW}}{W_1}\right)^2$$
$$\overline{\kappa}_m = \frac{\alpha_{C2} - \alpha_{C1}}{L} \tag{B.10}$$
$$\overline{b} = (b_1 + b_2)/2$$

The flow distortion in the meridional direction at the impeller tip results in a loss modelled as an **abrupt expansion loss**. This loss is given by

$$\overline{\omega}_\lambda = \left[(\lambda - 1)\frac{C_{m2}}{W_1}\right]^2 \tag{B.11}$$

with λ denoting the impeller tip distortion factor. The **wake mixing loss** involves only the meridional component of velocity and is given by

$$\overline{\omega}_{mix} = \left[\frac{(C_{m,wake} - C_{m,mix})}{W_1}\right]^2 \tag{B.12}$$

The clearance gap between the impeller blades and the compressor shroud leads to leakage flows resulting in the **clearance gap loss**. This loss is given by

$$\overline{\omega}_{CL} = \frac{2\dot{m}_{CL}\Delta p_{CL}}{\dot{m}_{\rho 1} W_1^2} \tag{B.13}$$

When the flow velocity near the suction surface of a blade is supersonic, shocks typically form. These shocks induce boundary layer separation which leads to a **supercritical Mach number loss**, estimated by

$$\overline{\omega}_{cr} = 0.4 \left[(M_1' - M_{cr}') \frac{W_{max}}{W_1} \right]^2 \tag{B.14}$$

All the internal loss coefficients mentioned were added and the loss in total pressure calculated iteratively when computing the impeller outlet properties.

The total work input required to compress the working fluid in the impeller is made up of four components. The **blade work input**, in an ideal situation, would be the only work input required. It is written as

$$I_B = \sigma(1 - \lambda\phi_2 \cot\beta_2) - \frac{U_1 C_{U1}}{U_2^2} \tag{B.15}$$

where σ denotes the impeller slip factor. There are however parasitic work input coefficients to consider, the first of these being the **disk friction loss**:

$$I_{DF} = (C_{MD} + C_{MC}) \frac{\rho_2 U_2 r_2^2}{2\dot{m}} \tag{B.16}$$

where C_{MD} and C_{MC} denote disk torque coefficients for the impeller disk and cover respectively. The compressor **recirculation work input**, I_R, typically presents itself at low relative mass flow rates and is associated with flow back to the impeller tip. This type of parasitic work is found in highly diffusing impellers, its coefficient computed from

$$\begin{aligned}
W_{max} &= \frac{1}{2}(W_1 + W_2 + \Delta W) \\
D_{eq} &= \frac{W_{max}}{W_2} \\
I_R &= \left(\frac{D_{eq}}{2} - 1\right)\left[\frac{W_{U2}}{C_{m2}} - 2\cot\beta_2\right] \\
I_R &\geq 0
\end{aligned} \tag{B.17}$$

The total work input coefficient required by the impeller to compress the working fluid is given by

$$I = \frac{\Delta h_t}{U_2^2} = I_B + I_{DF} + I_R \tag{B.18}$$

with the first term on the RHS denoting the useful work and last two terms denoting the parasitic work. All the loss coefficients and work input terms that were discussed in the preceding chapters were computed by the in-house mean-line code.

APPENDIX C: K27 GEOMTURBO FILE

```
GEOMETRY TURBO VERSION 3.7
geometric_tolerance 1e-006
blade_expansion_factor_hub 0.02
blade_expansion_factor_shroud 0.02
blade_merging +0
units 1
number_of_blades 7
SHROUD
XYZ
300
2.700000e+01      0.000000e+00      4.843110e+01
...
6.330350e+01      0.000000e+00      3.400000e+00
HUB
XYZ
300
8.000000e+00      0.000000e+00      4.843110e+01
...
6.330350e+01      0.000000e+00      6.000000e-01
SUCTION
SECTIONAL
2
# section 1
XYZ
320
8.000000e+00      0.000000e+00      3.000000e+01
...
2.361240e+01      2.913250e+01      0.000000e+00
# section 2
XYZ
320
2.700000e+01      0.000000e+00      3.000000e+01
...
...
# section 6
XYZ
320
2.700000e+01      0.000000e+00      3.000000e+01
...
2.360710e+01      2.913680e+01      4.000000e+00
PRESSURE
SECTIONAL
2
# section 1
XYZ
320
8.000000e+00      0.000000e+00      3.000000e+01
...
2.399880e+01      2.881510e+01      0.000000e+00
# section 2
XYZ
320
2.700000e+01      0.000000e+00      3.000000e+01
...
# section 6
```

```
XYZ
320
2.700000e+01      0.000000e+00       3.000000e+01
...
2.360710e+01      2.913680e+01       4.000000e+00
splitter_expansion_factor_hub 0.02
splitter_expansion_factor_shroud 0.02
splitter_merging +0
SUCTION_SPLITTER
SECTIONAL
2
# section 1
XYZ
320
1.028410e+01      2.641550e+00       1.880560e+01
...
3.391520e+01      1.600020e+01      -9.995120e-22
# section 2
XYZ
320
2.703290e+01     -3.313500e+00       2.329260e+01
...
...
# section 6
XYZ
320
2.700000e+01      0.000000e+00       3.000000e+01
...
2.360710e+01      2.913680e+01       4.000000e+00
PRESSURE_SPLITTER
SECTIONAL
2
# section 1
XYZ
320
1.028410e+01      2.641550e+00       1.880560e+01
...
3.412550e+01      1.554660e+01       9.995120e-22
# section 2
XYZ
320
2.703290e+01     -3.313500e+00       2.329260e+01
...
...
# section 6
XYZ
320
2.700000e+01      0.000000e+00       3.000000e+01
...
2.360710e+01      2.913680e+01       4.000000e+00
```

APPENDIX D: DESIGN AND TEST PROGRAM

D.1   Flow Chart
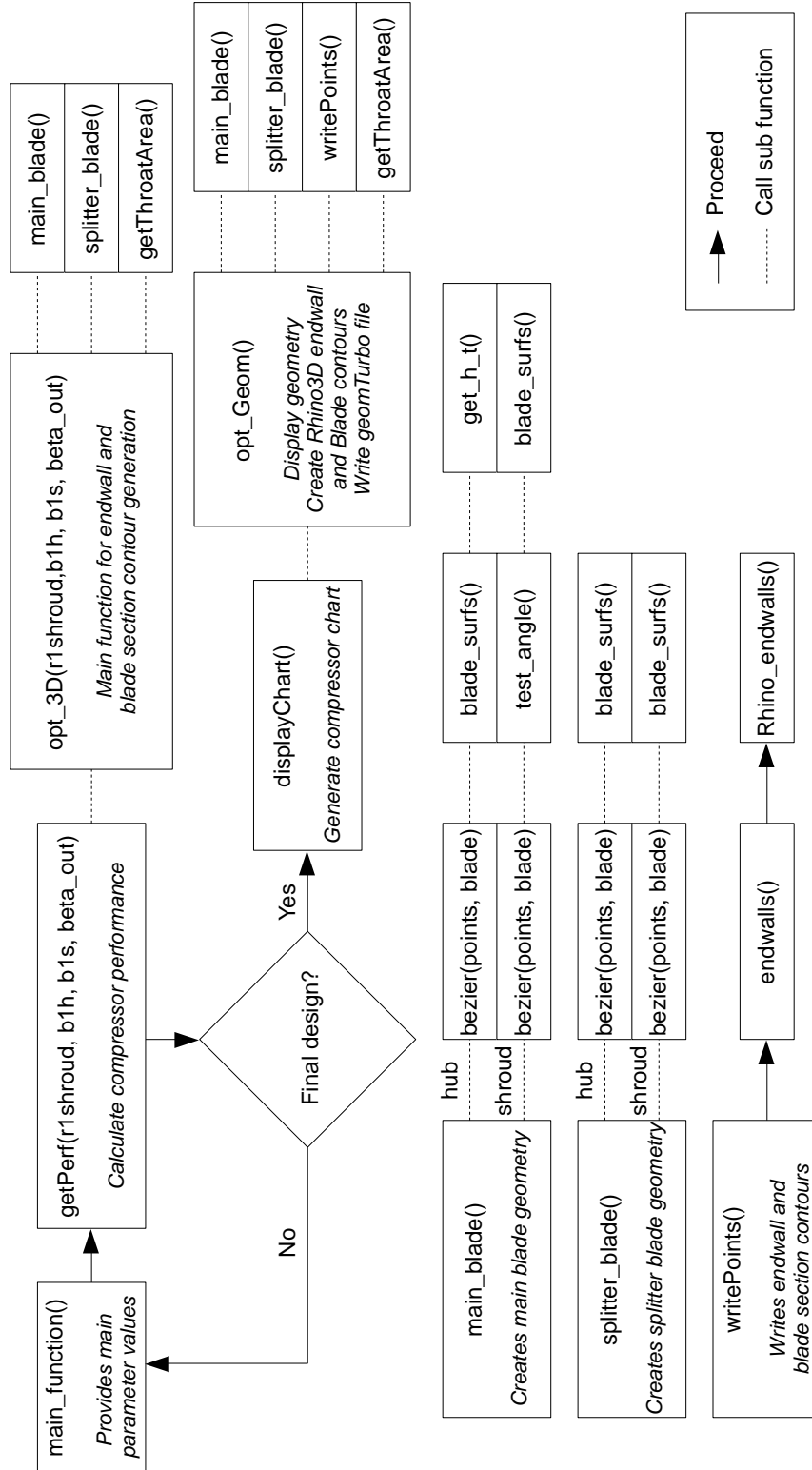
Figure D.1: Flow chart of mean-line approach to compressor design.

D.2   Program Code

```matlab
% Main function

% This program evaluates a range of compressor geometries defined by the
% main parameters. The values of the main parameters are incrementally
% adjusted to test the whole design space. An objective function by which
% to compare seperate geometries is also defined. The best design is
% updated at every step in the geometry definition loop. Once all parameter
% values have been evaluated, the best performing set is saved and the
% compressor chart of the "new design" is created.
function propOut = new_Design()
close all
clear all
clc


% Initialise structs
global imp
global bestImp

imp.mdot = 0.325;                     % test point mass flow rate
imp.imp_speed = 121000;               % test point impeller speed [rpm]

imp.blade_num = 7;               % number of main blades
imp.r_1_hub = 8.138;            % hub inlet diameter
imp.r_2 = 75/2;                 % radius at outlet
imp.blade_height = 6;           % blade tip height
imp.imp_height = 30;            % impeller height (z-direction)
imp.hub_angle = 0*pi/180;       % hub inlet angle relative to z-axis
imp.shroud_angle = 0*pi/180;    % shroud inlet angle relative to z-axis
imp.shroud_angle_out = 0*pi/180;   % shroud inlet angle relative to r-axis
imp.start_split = 0.275;        % splitter blade starting point along "u"
imp.bezier_size = 1000;     % bezier curve number of points (uneven spaced)
imp.size = 200;             % bezier curve number of points (even spaced)
imp.endwall_ext = 0.5;          % fraction extension of endwalls
imp.LE_hub = 2;                 % blade thickness @ hub leading edge
imp.LE_shroud = 0.6;            % blade thickness @ shroud leading edge
imp.TE = 0.6;                   % blade thickness @ trailing edge
imp.fillet_radius = 0;          % blade root fillet radius
imp.s_CL = 0.27;                % tip clearance gap
imp.ell_end = 0.1;              % ellipse end on "u"
imp.par_start = 0.8;            % parabole start on "u"
imp.diff_height = 5;            % height at diffuser outlet
imp.lean_angle = 90*pi/180;     % lean angle at blade tip
imp.leanExt = 0;                % 1 for "Yes" and 0 for "No"


% Initialise performance variables
bestObFunc = 0;
bestPerf(1,1) = 0;
bestPerf(2,1) = 0;
maxPP = 0;


% Loop to define different main parameter values
for r1shroud = 0.025:0.0001:0.027           % Shroud inlet radius
    for beta_1_hub = 70:-0.1:50             % Hub inlet angle
        clc
```

```matlab
        fprintf('Testing at r_1_shroud = %g/0.029\n', r1shroud);
        fprintf('Testing at beta_1_hub = %g\n', beta_1_hub);
        fprintf('Best tested pressure ratio:\t%g\n', bestPerf(1,1));
        fprintf('Best tested efficiency:\t\t%g\n\n', bestPerf(2,1));
        for beta_1_shroud = 35:-0.1:20      % Shroud inlet angle
            for beta_out = 90:-1:60         % Blade tip angle
                % Calculate compressor performance
                perf = getPerf(r1shroud,beta_1_hub,beta_1_shroud,beta_out);
                %test performance
                obFunc = real(perf(1,1))/5 + real(perf(2,1))/0.798;
                if (isnan(perf(1,1))==1||isnan(perf(2,1))==1||...
                        isreal(perf(1,1))==0||isreal(perf(2,1))...
                        ==0||perf(2,1)>=1)
                    break
                elseif (obFunc >= bestObFunc)
                    bestObFunc = obFunc;
                    bestPerf = perf;
                    bestR1Shroud = r1shroud;
                    bestBeta_1_hub = beta_1_hub;
                    bestBeta_1_shroud = beta_1_shroud;
                    bestBeta_out = beta_out;
                    bestImp = imp;
                end
                if (perf(1,1)>maxPP)
                    maxPP = perf(1,1);
                end
            end

        end
    end
end

% Create compressor chart
clc
fprintf('Plotting Compressor Chart...\n\n');
figure(1)
propOut = displayChart(bestR1Shroud,bestBeta_1_hub,bestBeta_1_shroud,...
    bestBeta_out,bestPerf);
figure(2)
opt_Geom(bestR1Shroud,bestBeta_1_hub,bestBeta_1_shroud,bestBeta_out);

% Display compressor main parameters and performance
clc
fprintf('The value of the objective function is:\t\t%g\n', bestObFunc);
fprintf('Design point pressure ratio:\t%g\n', bestPerf(1,1));
fprintf('Design point efficiency:\t\t%g\n\n', bestPerf(2,1));
fprintf('The impeller geometry is as follows:\n');
fprintf('Number of blades:\t%g\n', imp.blade_num);
fprintf('r_1_hub:\t\t\t%g mm\n', imp.r_1_hub);
fprintf('r_1_shroud:\t\t\t%g mm\n', bestR1Shroud*1e3);
fprintf('Beta_1_hub:\t\t\t%g deg\n', bestBeta_1_hub);
fprintf('Beta_1_shroud:\t\t%g deg\n', bestBeta_1_shroud);
fprintf('Outlet height:\t\t%g mm\n', imp.blade_height);
fprintf('Outlet angle:\t\t%g deg\n', bestBeta_out);
fprintf('Throat angle:\t\t%g deg\n', 90-imp.beta_th*180/pi);
fprintf('Throat area:\t\t%g m^2\n\n\n', imp.A_th*7);
```

D.3   Code Output

The outputs of the design and test program are shown in Figure D.2 and Figure D.3. The same outputs can be obtained for any realistic set of input parameters, as defined in the program code in Section C.2.
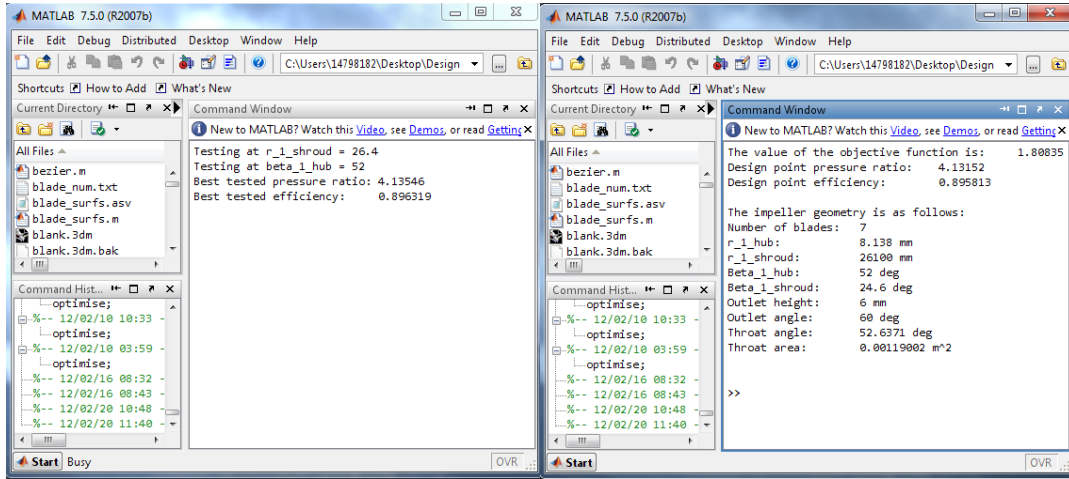
(A)   (B)

Figure D.2: MATLAB command window during (A) and after (B) code run.
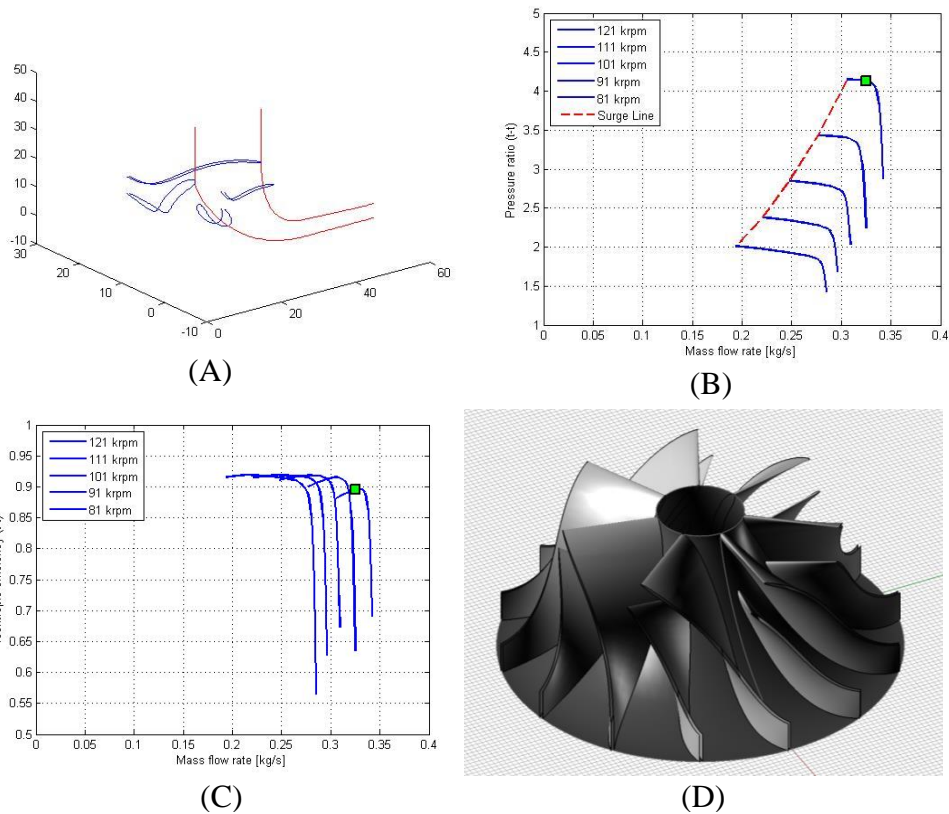
(A)   (B)

(C)   (D)

Figure D.3: MATLAB output figures. (A) is the hub and shroud, and blade sectional contours. (B) and (C) are the pressure ratio and efficiency curves. (D) is the impeller surface model (Rhinoceros3D).

APPENDIX E: BÉZIER CURVES

Surfaces that are subjected to fluid interaction typically have an effect on the fluid mechanics of the fluid with which they interact. The shape of these surfaces, which has the largest effect, is often derived from detailed calculations. These calculations take into consideration all the physics involved in and specific to the problem. NURBS curves have served as an excellent tool with which to create these types of surfaces (Rogers, 2001).

A type of curve that has been commonly used to describe aerodynamic surfaces is the Bézier curve, named after its French developer, Pierre Bézier. In the late 60's, Bézier derived the mathematical basis of the curve from geometrical considerations (Bézier, 1968, 1970, 1971).

Figure E.1 shows the basic components of a third order Bézier curve. The polygon, with control points P_0 through P_3, controls the properties of the curve. The properties for all nth order Bézier curves are the following:

- All basis functions are real.
- The degree of the polynomial which describes the curve segment is one less than the number of points describing the control polygon.
- The Bézier curve generally follows the control polygon shape.
- The first and last points of the Bézier curve and control polygon are coincident.
- The vectors of the first and last polygon lines have the same direction as that of the respective Bézier curve end tangents.
- The largest convex polygon, described by the control points, contains the Bézier curve.
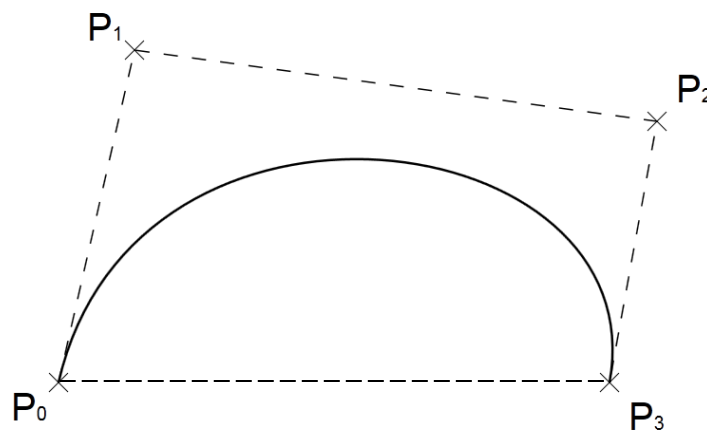
Figure E.1: Bézier curve and control polygon.

A Bézier curve is defined by the following equation:

$$P(t) = \sum_{i=0}^{n} B_i J_{n,i}(t) \qquad 0 \le t \le 1 \qquad\qquad (E.1)$$

The ith nth-order Bézier basis (or Bernstein blending) function is defined by:

$$J_{n,i}(t) = \binom{n}{i} t^i (1-t)^{n-i} \qquad (0)^0 \equiv 1 \qquad\qquad (E.2)$$

with

$$\binom{n}{i} = \frac{n!}{i!\,(n-i)!} \qquad 0! \equiv 1 \qquad\qquad (E.3)$$

Figure E.2 shows the Bézier blending function for different values of n. The maximum value for each basis function is found at $t = i/n$ where the value is given by the following equation from Forrest (1972):

$$J_{n,i}\left(\frac{i}{n}\right) = \frac{\binom{n}{i}\left(i^i (n-i)^{n-i}\right)}{n^n} \qquad\qquad (E.4)$$

It can also be shown that for any given parameter value t, the summation of the basis function is equal to unity:

$$\sum_{i=0}^{n} J_{n,i}(t) = 1 \qquad\qquad (E.5)$$
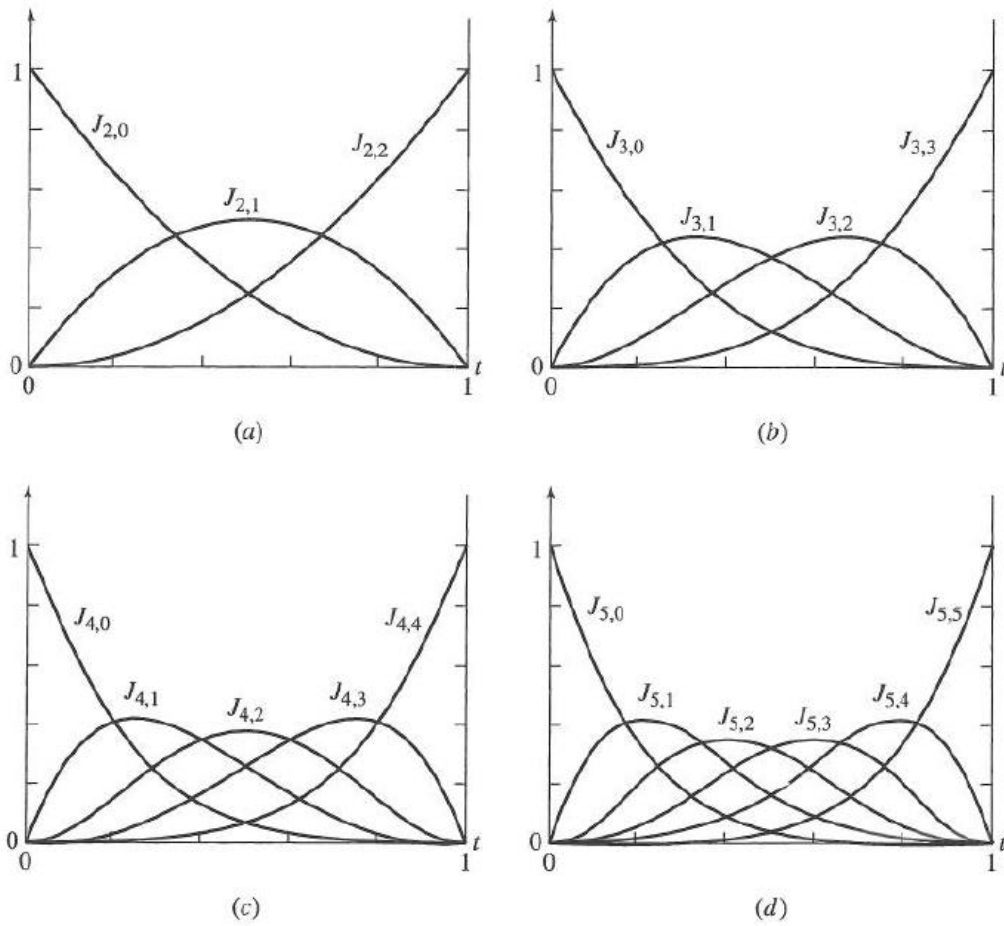
Figure E.2: Bezier blending functions. (a) Three polygon points, n = 2; (b) four polygon points, n = 3; (c) five polygon points, n = 4; (d) six polygon points, n = 5. (Rogers, 2001)

APPENDIX F: IMPELLER SURFACE MODEL RHINO SCRIPT

```
Sub Impeller()
' Declare variables and constants
Const xlDown = -4121
Const rhObjectCurve = 4
Dim arrObjects, strObject
Dim sFileName, aPoints(), x, y, z, main1, main2, tel,
strCurve
Dim oExcel, oSheet, nRow, nRowCount, temporary
Dim arrCenter, nCount
Dim dAngle, arrAxis, arrXform, i
Rhino.ViewDisplayMode ,1
```

Import point data of hub contour.
```
sFileName                                            =
"C:\Users\14798182\Desktop\Design_Geometry\Rhino_hub.txt"
If IsNull(sFileName) Then Exit Sub
' Launch Excel and open the specified file
Set oExcel = CreateObject("Excel.Application")
oExcel.Workbooks.Open(sFileName)
' Get the active worksheet
Set oSheet = oExcel.ActiveSheet
' Count the number of rows that need to be processed
nRowCount                 =                 oSheet.Range("a1",
oSheet.Range("a1").End(xlDown)).Rows.Count
If (nRowCount = 0 ) Then
Rhino.Print "No data range found in file."
Exit Sub
ElseIf (nRowCount < 2 ) Then
Rhino.Print "Not enough points to create curve."
Exit Sub
End If
' Re-dimension the resulting array of points accordingly
ReDim aPoints(nRowCount-1)
' Process all rows
Rhino.Print "Importing data..."
For nRow = 1 To nRowCount
' Read the values from columns A, B, and C
x = oSheet.Cells(nRow, 1).Value
y = oSheet.Cells(nRow, 2).Value
z = oSheet.Cells(nRow, 3).Value
' If the values are all numeric, create an array from the
' values and add it to the array of points
If IsNumeric(x) And IsNumeric(y) And IsNumeric(z) Then
```

```
aPoints(nRow-1) = Array(x,y,z)
Else
oExcel.Quit
Set oSheet = Nothing
Set oExcel = Nothing
Rhino.Print "Non-numeric data found in row " & CStr(nRow) &
"."
Exit Sub
End If
Next
' Close Excel and disassociate object variables
oExcel.Quit
Set oSheet = Nothing
Set oExcel = Nothing
```

Create hub contour by drawing interpolated curve through points. If at least two points were read in, create the curve.
```
If (UBound(aPoints) > 0) Then
  arrObjects = Rhino.AddInterpCurve(aPoints,5,2)
End If
temporary = Rhino.NormalObjects
```

Create hub surface by revolving hub contour.
```
Rhino.AddRevSrf          arrObjects,          Array(Array(0,0,0),
Array(0,0,1))
Rhino.HideObjects temporary
arrObjects = Rhino.NormalObjects
Rhino.LockObjects arrObjects
```

Import point data of main blade hub contour.
```
' Get the name of the file to import
sFileName                                                    =
"C:\Users\14798182\Desktop\Design_Geometry\main_hub.txt"
If IsNull(sFileName) Then Exit Sub
' Launch Excel and open the specified file
Set oExcel = CreateObject("Excel.Application")
oExcel.Workbooks.Open(sFileName)
' Get the active worksheet
Set oSheet = oExcel.ActiveSheet
' Count the number of rows that need to be processed
nRowCount                  =                  oSheet.Range("a1",
oSheet.Range("a1").End(xlDown)).Rows.Count
If (nRowCount = 0 ) Then
Rhino.Print "No data range found in file."
Exit Sub
ElseIf (nRowCount < 2 ) Then
```

```
Rhino.Print "Not enough points to create curve."
Exit Sub
End If
' Re-dimension the resulting array of points accordingly
ReDim aPoints(nRowCount-1)
' Process all rows
Rhino.Print "Importing data..."
For nRow = 1 To nRowCount
' Read the values from columns A, B, and C
x = oSheet.Cells(nRow, 1).Value
y = oSheet.Cells(nRow, 2).Value
z = oSheet.Cells(nRow, 3).Value
' If the values are all numeric, create an array from the
' values and add it to the array of points
If IsNumeric(x) And IsNumeric(y) And IsNumeric(z) Then
aPoints(nRow-1) = Array(x,y,z)
Else
oExcel.Quit
Set oSheet = Nothing
Set oExcel = Nothing
Rhino.Print "Non-numeric data found in row " & CStr(nRow) &
"."
Exit Sub
End If
Next
' Close Excel and disassociate object variables
oExcel.Quit
Set oSheet = Nothing
Set oExcel = Nothing
' If at least two points were read in, create the curve
If (UBound(aPoints) > 0) Then
  main1 = Rhino.AddInterpCurve(aPoints,5,2)
End If
```
...code is repeated for shroud contour of main blade, and hub and shroud contours of splitter blade.

Loft blade contours to create blade surfaces.
```
arrObjects = Rhino.NormalObjects
Rhino.AddLoftSrf arrObjects,,, 3, 1, 1000
```

Circular pattern blades according to "blade_num.txt".
```
sFileName                                              =
"C:\Users\14798182\Desktop\Design_Geometry\blade_num.txt"
If IsNull(sFileName) Then Exit Sub
' Launch Excel and open the specified file
Set oExcel = CreateObject("Excel.Application")
```

```
oExcel.Workbooks.Open(sFileName)
' Get the active worksheet
Set oSheet = oExcel.ActiveSheet
' Count the number of rows that need to be processed
x = oSheet.Cells(1, 1).Value
bladeNum = x
' Close Excel and disassociate object variables
oExcel.Quit
Set oSheet = Nothing
Set oExcel = Nothing
' If at least two points were read in, create the curve
Rhino.ViewDisplayMode ,1
   arrObjects = Rhino.NormalObjects
   If IsNull(arrObjects) Then Exit Sub
    arrCenter = Array(0,0,0)
   If IsNull(arrCenter) Then Exit Sub
    nCount = bladeNum
   If IsNull(nCount) Then Exit Sub
    dAngle = 360.0 / nCount
    Rhino.EnableRedraw False
    For i = 1 To nCount - 1
     arrAxis = Array(0,0,1) ' world z-axis
     arrXform  =  Rhino.XformRotation(dAngle  *  i,  arrAxis,
arrCenter)
      Rhino.TransformObjects arrObjects, arrXform, True
    Next
    Rhino.EnableRedraw True
   End Sub
```

APPENDIX G: COMPUTATIONAL MESH DETAILS

The computational meshes for the mean-line design, DOE database and GA samples, and optimised design were created using the same settings. These settings, along with the qualities of the meshes created (mean-line and optimised designs) and the mesh dependency study results are presented in this Appendix. The mesh components are discussed in more detail in Section 3.4.

G.1 Mesh Settings

An impeller **rotational speed** of 121 krpm was specified.

Blade fillets were omitted from the CFD analysis, as mentioned in Section 3.4.2.

The **clearance gaps** were assigned a value of $t = 0.27$ mm at both the leading and trailing edges of the impeller blades.

The same **wall cell width** used in the benchmark CFD was assigned to the new mesh ($y_{wall} = 6$ μm).

The **blade topology** used during the meshing of the computational domain was an H&I topology. Figure G.1 shows the different mesh blocks that make up a blade-to-blade plane for the H&I topology. The topologies for both blades were each preceded by an inducer block containing 9 points in the streamwise direction and extended by a discharge block, also with 9 streamwise points. An O block skin mesh with 17 points was included around the main and splitter blades.
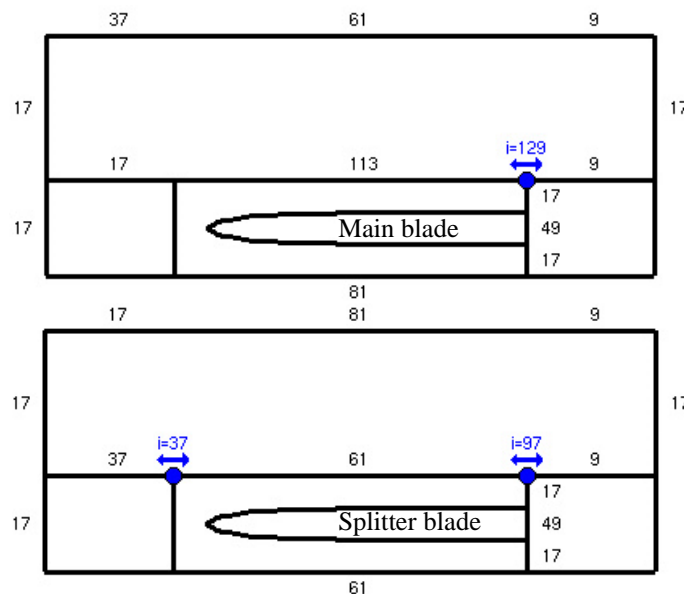
Figure G.1: H&I topology for main and splitter blades. Note the node distributions and amounts on the mesh blocks.

The number of blade-to-blade mesh **optimisation** steps was set to 350.

The **span interpolation** was set to 2%.

The blade-to-blade meshes for the mean-line and optimised designs at 50% span are shown in Figure G.2.
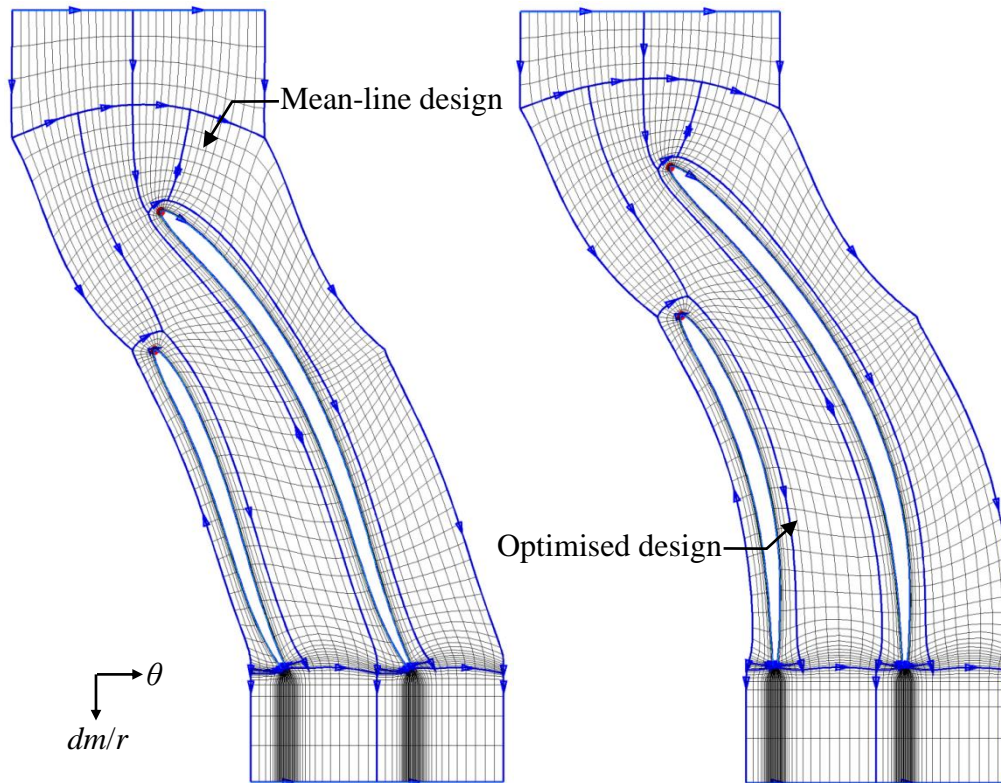
Figure G.2: Blade-to-blade meshes at 50% span (2ⁿᵈ multigrid level).

G.2   Mesh Quality

The final 3-dimensional meshes for the mean-line and optimised designs both had a total of 1,308,448 nodes with 3 multigrid levels. The mesh qualities for the mean-line and optimised designs are shown in Table G.1 and Table G.2 respectively.

Table G.1: Mean-line design mesh quality.

Quantity	Required value	"Worst" value	% "bad" cells
Orthogonality	$> 20°$	$26.7°$	0%
Expansion ratio	< 2.5	3.38	0.032%
Angular deviation	$< 40°$	$28.6°$	0%
Aspect ratio	< 2100	614	0%

Table G.2: Optimised design mesh quality.

Quantity	Required value	"Worst" value	% "bad" cells
Orthogonality	$> 20°$	$28.8°$	0%
Expansion ratio	< 2.5	2.57	0.015%
Angular deviation	$< 40°$	$39.4°$	0%
Aspect ratio	< 2100	1012	0%

G.3   Mesh Dependency

For each of the impellers (k27, mean-line, and optimised), the total-to-static efficiencies and pressure ratios were calculated for three different computational meshes (three multigrid levels) to rule out mesh dependency. It should be noted that the difference in density between the coarse, medium, and fine meshes was significant. This was because the mesh densities depended on the number of available multigrid levels (see Section 3.4.2). It was not possible to compare CFD results for meshes with specific numbers of nodes (e.g. multiples of original) as new meshes had to be created to allow for this. As a result, the qualities (expansion ratio, orthogonality, etc.) of the new meshes would differ and an objective comparison of the calculated performance as a function of the number of nodes could not be made. Multigrid level meshes were therefore used as the mesh qualities for these meshes were relatively similar. The results of the mesh dependency study are shown in Table G.3.

Table G.3: Mesh dependency.

Mesh	Number of nodes	Efficiency (t-s)	Pressure ratio (t-s)
k27			
coarse	36,172	76.5%	3.302
medium	249,563	76.1%	3.302
fine	1,846,597	73.7%	3.292
Mean-line			
coarse	26,590	83.7%	2.982
medium	179,248	76.1%	2.813
fine	1,308,448	74.6%	2.84
Optimised			
coarse	26,590	81.6%	3.288
medium	179,248	77.3%	3.317
fine	1,308,448	74.7%	3.28

The results in Table G.3 show good convergence for the calculated pressure ratios with increasing mesh densities. The maximum difference between calculated pressure ratios for coarse and fine meshes is 5%. The maximum difference between calculated efficiencies for coarse and fine meshes is 11%. The large difference between the calculated efficiencies can be ascribed to the large difference in mesh densities.

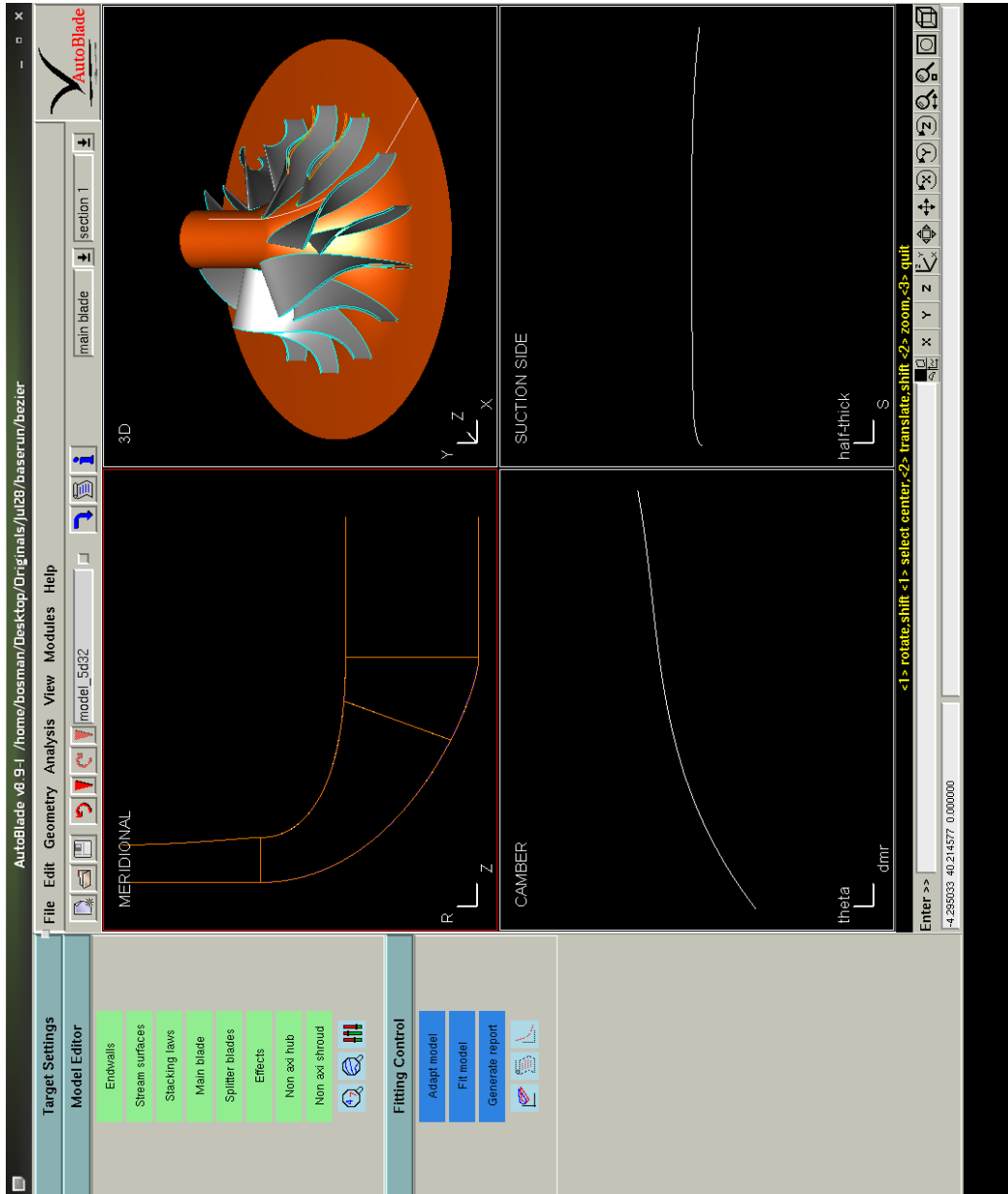# APPENDIX H: NUMECA™ AUTOBLADE™ DESIGN SPACE

Figure H.1: NUMECA™ Autoblade™ design space.

APPENDIX I: DOE IMPELLER PARAMETERS

Table I.1: Endwall parameters.

NAME	Control point	MINIMUN	VALUE	MAXIMUM	REFERENCE
HUB_Z1	h_{0z}		Z_LE_HUB+0.5*HUB_R5 (48.75)		
HUB_R1	h_{0r}	8.138	8.138	8.138	0.000001
HUB_Z2	h_{1z}		Z_LE_HUB (30)		
HUB_R2	h_{1r}		HUB_R1 (8.138)		
HUB_Z3	h_{B1z}		Z_LE_HUB-5 (25)		
HUB_R3	h_{B1r}		HUB_R1 (8.138)		
HUB_Z4	h_{B2z}	0	0	0	0.000001
HUB_R4	h_{B2r}	18	18	18	0.000001
HUB_Z5	h_{2z}	0	0	0	0.000001
HUB_R5	h_{2r}	37.5	37.5	37.5	0.000001
HUB_Z6	h_{3z}		HUB_Z5 (0)		
HUB_R6	h_{3r}		HUB_R5*1.5 (56.25)		
SHROUD_Z1	s_{0z}		HUB_Z1 (48.75)		
SHROUD_R1	s_{0r}	26.1	26.1	26.1	0.000001
SHROUD_Z2	s_{1z}		Z_LE_HUB (30)		
SHROUD_R2	s_{1r}		SHROUD_R1 (27)		
SHROUD_Z3	s_{B1z}		SHROUD_Z4+SHROUD_BEZIER_2*SHROUD_Z2 (9)		
SHROUD_R3	s_{B1r}		SHROUD_R1 (27)		
SHROUD_Z4	s_{B2z}		tan(THETA_SHROUD_OUT*pi/180)*(SHROUD_R5-SHROUD_R4)+SHROUD_Z5 (6)		
SHROUD_R4	s_{B2r}		SHROUD_R1+(35-SHROUD_R1)*SHROUD_R4_RATIO (34)		
SHROUD_Z5	s_{2z}	6	6	6	0.000001
SHROUD_R5	s_{2r}		HUB_R5 (37.5)		
SHROUD_Z6	~		SHROUD_Z5-(SHROUD_R6-SHROUD_R5)*tan(THETA_SHROUD_OUT*pi/180) (6)		
SHROUD_R6	~	42.99495484	42.99495484	42.99495484	0.001
SHROUD_Z7	~		SHROUD_Z8 (5)		
SHROUD_R7	~		SHROUD_R6+(SHROUD_R8-SHROUD_R6)/2 (49.6224774194546)		
SHROUD_Z8	s_{3z}	5	5	5	0.001
SHROUD_R8	s_{3r}		HUB_R6 (56.25)		

Table I.2: Stream surface parameters.

NAME	MINIMUN	VALUE	MAXIMUM	REFERENCE
S1_SPAN	0.005194167	0.005194167	0.005194167	0.01
S2_SPAN	0.998287295	0.998287295	0.998287295	0.01

Table I.3: Camber line parameters (section 1 and 2).

NAME	MINIMUN	VALUE	MAXIMUM	REFERENCE
S1_CAMBER_H1		S1_MERID_LENGTH/(3.439*tan(BETHA_HUB_IN*pi/180)) (0.733487502010582)		
S1_CAMBER_H2		S1_CAMBER_H3-DELTA_1B (0.883647887595772)		
S1_CAMBER_H3	0.7	0.885054911	1	0.001
S1_CAMBER_H4		S1_MERID_LENGTH/4.717*tan(BETHA_HUB_OUT*pi/180)+ S1_CAMBER_H3 (0.885)		
S1_LE_START	0.09126633	0.09126633	0.09126633	0.01
S1_HALF_THICKNESS_X1	0.1	0.1	0.1	0.001
S1_HALF_THICKNESS_Y1	1	1	1	0.001
S1_HALF_THICKNESS_X2	0.8	0.8	0.8	0.001
S1_HALF_THICKNESS_Y2	1	1	1	0.001
S1_HALF_THICKNESS_X3	1	1	1	0.001
S1_HALF_THICKNESS_Y3	0.3	0.3	0.3	0.001
S1_SPLIT1_MLE	0.33	0.42	0.53	0.05
S1_SPLIT1_MTE	0	0	0	0.05
S1_SPLIT1_DELTA_THETA	-0.001767876	-0.001767876	-0.001767876	0.05
S1_SPLIT1_LE_START	0.1	0.1	0.1	0.01
S1_SPLIT1_HALF_THICKNESS_X1	0.148	0.148	0.148	0.001
S1_SPLIT1_HALF_THICKNESS_Y1	1	1	1	0.001
S1_SPLIT1_HALF_THICKNESS_X2	0.704	0.704	0.704	0.001
S1_SPLIT1_HALF_THICKNESS_Y2	1	1	1	0.001
S1_SPLIT1_HALF_THICKNESS_X3	1	1	1	0.001
S1_SPLIT1_HALF_THICKNESS_Y3	0.3	0.3	0.3	0.001
S2_CAMBER_H1		S2_MERID_LENGTH/(3.439*tan(BETHA_SHROUD_IN*pi/180)) (0.489527625984561)		
S2_CAMBER_H2		S2_CAMBER_H3 (0.885054911177647)		
S2_CAMBER_H3		((S1_CAMBER_H4-S1_CAMBER_H3)/(S1_MERID_LENGTH/4.717)*(-S2_MERID_LENGTH/4.717)-S2_CAMBER_H4) (0.885054911177647)		
S2_CAMBER_H4		S1_CAMBER_H4 (0.885054911177647)		
S2_LE_START	0.09482558	0.09482558	0.09482558	0.01
S2_HALF_THICKNESS_X1	0.1	0.1	0.1	0.001
S2_HALF_THICKNESS_Y1	0.3	0.3	0.3	0.001
S2_HALF_THICKNESS_X2	0.8	0.8	0.8	0.001
S2_HALF_THICKNESS_Y2	0.3	0.3	0.3	0.001
S2_HALF_THICKNESS_X3	1	1	1	0.001
S2_HALF_THICKNESS_Y3	0.3	0.3	0.3	0.001
S2_SPLIT1_MLE	0.2	0.245	0.4	0.05
S2_SPLIT1_MTE	0	0	0	0.05
S2_SPLIT1_DELTA_THETA	0.001340144	0.001340144	0.001340144	0.05
S2_SPLIT1_LE_START	0.1	0.1	0.1	0.01
S2_SPLIT1_HALF_THICKNESS_X1	0.148	0.148	0.148	0.001
S2_SPLIT1_HALF_THICKNESS_Y1	0.3	0.3	0.3	0.001
S2_SPLIT1_HALF_THICKNESS_X2	0.704	0.704	0.704	0.001
S2_SPLIT1_HALF_THICKNESS_Y2	0.3	0.3	0.3	0.001
S2_SPLIT1_HALF_THICKNESS_X3	1	1	1	0.001
S2_SPLIT1_HALF_THICKNESS_Y3	0.3	0.3	0.3	0.001

Table I.4: Meridional parameters.

NAME	MINIMUN	VALUE	MAXIMUM	REFERENCE
Z_LE_HUB	27	30	33	1
Z_LE_SHROUD		Z_LE_HUB (30)		
R_TE_HUB	37.5	37.5	37.5	1.00E-06
R_TE_SHROUD	37.5	37.5	37.5	1.00E-06
S1_MERID_LENGTH	0	3.006154961	1000000000	0.001
S2_MERID_LENGTH	0	0.97196081	1000000000	0.001

Table I.5: Tangential parameters.

NAME	MINIMUN	VALUE	MAXIMUM	REFERENCE
LEAN_BETA	0	0	0	1

Table I.6: Other parameters.

NAME	MINIMUN	VALUE	MAXIMUM	REFERENCE
NB	7	7	7	1
BLADE_ROTATION	0	0	0	1

Table I.7: Custom parameters.

NAME	MINIMUN	VALUE	MAXIMUM	REFERENCE
DELTA_1B	0	0.001407024	0.04	1
THETA_SHROUD_OUT	0	0	20	1
BETHA_HUB_OUT	0	0	10	1
BETHA_HUB_IN	45	50	60	1
BETHA_SHROUD_IN	22	30	32	1
SHROUD_BEZIER_2	0	0.1	0.25	1
SHROUD_R4_RATIO	0	0.875	1	1

APPENDIX J: ARTIFICIAL NEURAL NETWORK

An Artificial Neural Network is based on the concept of function approximation. The purpose of an ANN is to provide a fast method of predicting variables that would normally require long computational times to calculate. This prediction needs to be as accurate as possible when compared to the conventional calculation method (i.e. CFD and FEA).

An ANN requires an initial database of samples (input and output variables) that are generated with the method of conventional calculation. These samples are used to construct an approximate model with the same input and output variables as the conventional calculation. The approximate model can be used as a cost function for optimisation, reducing the computational time of the optimisation process.

Figure J.1 schematically depicts an ANN, which consists of several elementary processing units called nodes. These nodes are arranged in layers, joined with connections of varying intensities, called connection weights. The connections form a parallel architecture. An ANN typically consists of several layers: an input layer, one or more hidden layers, and one output layer. Every element of the input vector is connected to every node of the input layer via a weight. Each node summates the weighted input variables and produces a scalar output which is processed by the transfer function, F1. The output of the transfer function is again weighted and used as an input for the final, output layer.
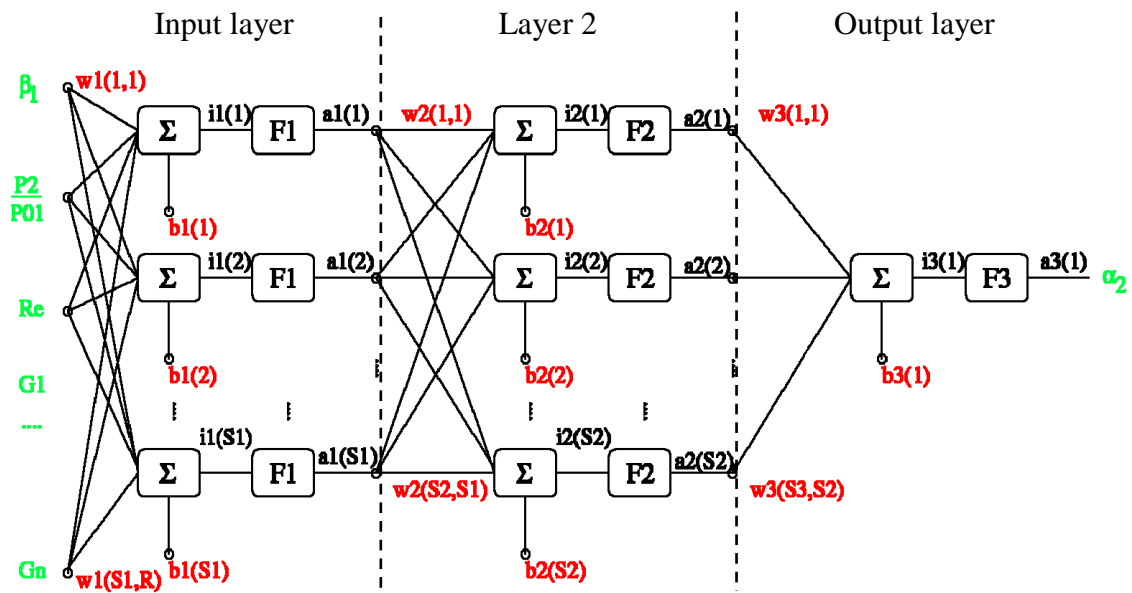
Figure J.1: Artificial Neural Network (Numeca International, 2011e).

In Figure J.1, the variable weights are given by $w_n(a,b)$, and the biases by $b_n(a)$, where

$$n \;=\; \text{layer number}$$
$$a \;=\; \text{node number}$$
$$b \;=\; \text{variable number}$$

115

During the training process, the weights and biases are adjusted in order to obtain convergence between the output variables of the ANN and a conventional method. If the ANN is presented with inputs that were not part of the training process, the accuracy of the output depends on the number and scope of the samples used for training. Trained ANN's tend to give reasonable results with new input sets.

To measure the accuracy of an ANN, the error between the output of the ANN and sample output from the training database is calculated. The error used for the convergence criterion is given by:

$$E_{rms}(l) = \frac{\sum_t [d(l) - a(l)]^2}{N_t}$$

(J.1)

where

$E_{rms}(l)$ = error for output node 1 over all training samples
l = output node index
d = desired output
a = ANN predicted output
N_t = number of training samples

The global training error will be

$$E_{rms} = \frac{\sum_o (E_{rms(l)})^2}{N_o}$$

(J.2)

where

E_{rms} = is the global neural network error based on the training databse
N_o = number of neural network outputs

APPENDIX K: OPTIMISATION: GENETIC ALGORITHM

According to Haupt & Haupt (2004), optimisation is the process of making something better. Optimisation involves initiating a problem or function with different variables or parameters and then calculating and improving the result with the new information gained. The result of the function can represent, for example, the performance of a centrifugal compressor; with different performance properties being weighted more or less (assigned a cost). The final performance is represented as a cost function, with the value penalised (increased) if the required performance is not obtained. The "best" result is obtained when the cost function value is at an absolute (global) minimum (see Figure K.1) on the cost function surface. The presence of local minima complicates the process as some optimisation algorithms tend to converge around these points.
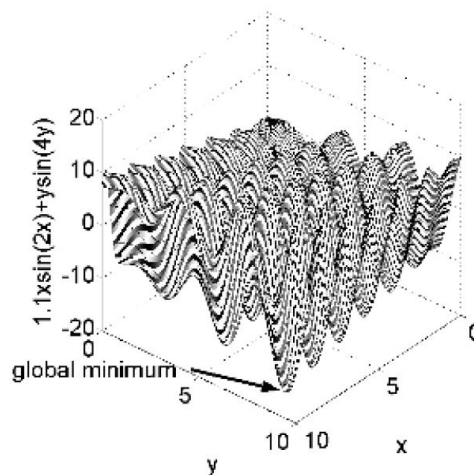

Figure K.1: Function surface showing global minimum located among local minima (Haupt & Haupt, 2004).

A computer is the perfect tool for optimisation as long as the variables (or parameters) affecting the result can be input in electronic format. The data is fed into the computer and the result is obtained. Whether or not this is the best result is a difficult question to answer.

K.1   Optimisation Categories

Optimisation can be divided into 6 main categories. These categories are not mutually exclusive and can be seen in Figure K.2.
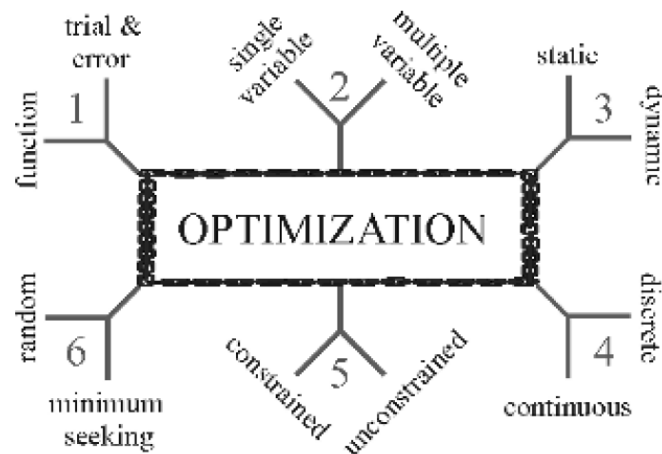
Figure K.2: Six categories of optimisation algorithms (Haupt & Haupt, 2004).

The **trial-and-error** approach involves adjusting the parameter values without having an idea what the affect will be on the result. This is an easy but time consuming approach. Depending on the parameters used, there can be an infinite amount of variations to test. In contrast, a mathematical formula can describe the **function** result. This formula can then be optimised using mathematical manipulation.

Optimisation problems can either be 1-dimensional (having only a **single variable** to solve) or multi-dimensional (**multiple variables**). The problem increases in complexity with an increase in the number of variables. Different types of optimisation are also more suited to problems depending on the number of variables.

An optimisation problem can be **static** (not dependent on time) or **dynamic** (time-dependent). Static problems, for example, are steady-state CFD solutions. These solutions have constant values for their boundary conditions. Dynamic problems include the modelling of compressor surge and vortex shedding which are unsteady flow phenomena.

The variables initiating a function can either be **discrete** or **continuous**. Discrete variables only have a finite amount of possible values. The amount of possible values for a continuous variable is infinite. The exactness of a continuous variable value depends on the internal precision and round off of the computer used for optimisation. These variables may also have limits or constraints. A **constrained** variable has a value that falls within a set range. An **unconstrained** variable may take on any value. As most optimisation routines work best with unconstrained variables, a constrained variable, x, can be described by an unconstrained variable, u (equation (K.1)).

$$-1 \leq x \leq 1 \quad x = \sin(u) \qquad u \in R \qquad\qquad (K.1)$$

The approach used **by minimum seeking** optimisation algorithms to minimise the cost of a function involves starting with an initial set of variables. Moving from the initial set to the next is based on some determinant set of steps. These algorithms tend to converge at local minima. **Random** methods employ a probabilistic approach to calculations to obtain sets of variables. These algorithms have a greater success in finding global minimums but tend to be slower.

K.2 Genetic Algorithm

In this project, the algorithm used to perform optimisation was a Biological optimisation scheme called a Genetic Algorithm (GA). According to Haupt and Haupt, the advantages of a GA are that it:

- Optimises with continuous or discrete variables.
- Does not require derivative information.
- Simultaneously searches from a wide sampling of the cost surface.
- Can analyse large sets of variables.
- Is suited to parallel computing.
- Can locate the global minimum on extremely complex cost surfaces.
- Works with numerically generated, experimental, or analytical data.

The optimisation process, as seen in Figure K.3, is initialised by defining a chromosome as an array of variables that are to be optimised.

$$chromosome = [p_1, p_2, p_3, \dots, p_{N_{var}}] \tag{K.2}$$

The variable values are represented by floating-point numbers. The cost of each chromosome is evaluated by the cost function,

$$cost = f(chromosome) = f(p_1, p_2, p_3, \dots, p_{N_{var}}) \tag{K.3}$$

Equations (K.2) and (K.3), along with the variable constraints, constitute the optimisation problem and the first step in the flowchart shown in Figure K.3. The aim is to find the global minimum of (K.3).

An initial population is defined by a full matrix with the number of rows being the number of chromosomes, or population size. The number of columns is equal to the number of variables per chromosome. The population matrix is given by (K.4). The population of chromosomes is not a democracy as individual chromosomes are not all equal when their cost is evaluated.

$$population = N_{chrom} \times N_{var} \tag{K.4}$$

The next step in the optimisation process is to select the chromosomes which are fit enough (have a small enough cost) to survive and possibly produce "offspring"

in the next generation. The chromosomes are ranked from lowest to highest according to their cost. The worst performing chromosomes die off and are replaced by offspring. This process is repeated at each iteration of the algorithm. Not all surviving chromosomes are deemed fit enough to mate and are replaced by offspring of other, fitter chromosomes.
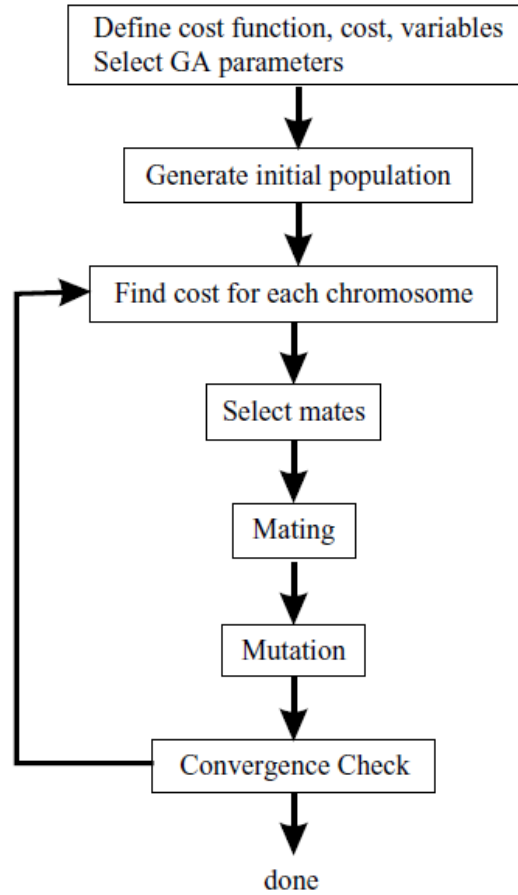
Figure K.3: Flow chart of continuous Genetic Algorithm (Haupt & Haupt, 2004).

The fittest chromosomes from the initial population are selected for the mating pool. Mothers and fathers are selected in a random fashion, each pair producing offspring. The parents also survive to form part of the next generation. If the traits (variable values and chromosome cost) of the parents are similar, the likelihood that the offspring will carry the same traits is high. Many approaches have been utilised for mating chromosomes and creating offspring (Adewuya (1996) and Michalewicz (1994)). The simplest method is to choose points in the chromosome as crossover points. At either side of these points, the offspring possesses the variable values of the parents. There can be more than one crossover point.

$$parent_1 = \left[p_{m1}, p_{m2}, p_{m3}, p_{m4}, p_{m5}, p_{m6}, \ldots, p_{mN_{var}}\right]$$
$$parent_2 = \left[p_{d1}, p_{d2}, p_{d3}, p_{d4}, p_{d5}, p_{d6}, \ldots, p_{dN_{var}}\right]$$

(K.5)

The crossover points are randomly selected and the values input on either sides to create the offspring:

$$offspring_1 = \left[p_{m1}, p_{m2}, |p_{d3}, p_{d4}, |p_{m5}, p_{m6}, \dots, p_{mN_{var}}\right]$$
$$offspring_2 = \left[p_{d1}, p_{d2}, |p_{m3}, p_{m4}, |p_{d5}, p_{d6}, \dots, p_{dN_{var}}\right]$$

(K.6)

There is also the method of randomly selecting which point in an offspring chromosome will be assigned a value from which parent. This method is called uniform crossover.

This approach to creating offspring is suited to discrete variables. However, for continuous variables there are many more values which now are not tested because they did not appear in the initial population. This necessitates a process called mutation which introduces new genetic material. The problem can be somewhat remedied by blending methods which create an offspring variable from a combination of two parent values:

$$p_{new} = \beta p_{mn} + (1 - \beta)p_{dn}$$

(K.7)

where

$\beta =$ random number on the interval $[0,1]$
$p_{mn} = n$th variable in the mother chromosome
$p_{dn} = n$th variable in the father chromosome

Choosing which variables to blend is an issue. Also, the values of new variables cannot venture beyond the extremes in the population brought on by parent values. To accomplish this requires an extrapolating method, the simplest of which is a linear crossover (Wright, 1991). Three offspring are generated using the variables of two parents:

$$p_{new1} = 0.5p_{mn} + 0.5p_{dn}$$
$$p_{new2} = 1.5p_{mn} - 0.5p_{dn}$$
$$p_{new3} = -0.5p_{mn} + 1.5p_{dn}$$

(K.8)

A variable that falls outside the set bounds is discarded, with the best two offspring subsequently propagating.

If care is not taken, the GA can converge on one region of the cost surface too quickly. This increases the probability of missing the global minimum and resulting in a less than optimum chromosome. In order to avoid this problem, the routine can be forced to explore new areas of the cost surface. This is done by randomly introducing changes to chromosome variables, and is termed mutation.

The extent of mutation is controlled by the mutation rate, μ, which is the percentage of the population variables that may be mutated. The variables that are

to be mutated are randomly selected, at which point the variable values are randomly generated. The number of mutations to be performed for each population is given by:

$$N_{mutation} = \mu(N_{chrom} - 1)N_{var} \tag{K.9}$$

The whole process, from cost calculation to ranking to mating to mutation, is repeated for any number of steps until convergence is reached. The solution converges when no significantly lower cost is calculated for a new chromosome than that of the elite chromosome.

APPENDIX L: OPTIMISED IMPELLER (SCALE 1:1)